

THE UNIVERISTY OF HULL

FORMATION AND PROPERTIES OF ALUMINA COATINGS

being a thesis submitted for the Degree of

Doctor of Philosophy

in the University of Hull

by

Jochen Michael Schneider

M.Sc. Hull
Dipl.Ing.(FH) Furtwangen

September 1997



© Copyright by Jochen M. Schneider, 1997

All Rights Reserved

Für meine Eltern

Preface

The experimental work that forms the base of the thesis has been carried out at BIRL/Northwestern University in the time period from October 1994 to April 1997. Much of the time has been spent in re-designing a 70 liter magnetron sputtering system, for effective ionization of the aluminum flux. Films were also grown in an industrial size (300 liter) opposed cathode magnetron sputtering system. Evaluation software for the nanoindentation system was written during the course of this study.

The work has been devoted to the following aspects of PVD alumina deposition:

(I) A novel, **very high rate process** for the deposition of alumina was developed. Based on a combination of partial pressure control of the reactive gas and medium frequency D.C. power, this technology can be utilized for other oxide coating systems too, as demonstrated on zirconia.

(II) **Phase formation studies** in the alumina system, resulted in development of a deposition process for kappa alumina onto metallic substrates, at substrate temperatures $< 500^{\circ}\text{C}$. This work was the basis for a patent application.

The research presented in Chapters III to VII resulted in six mainauthored papers, all accepted for publication in refereed international journals, or conference proceedings.

Abstract

Formation and Properties of Alumina Coatings

Jochen M. Schneider

Investigations concerning the microstructure and mechanical properties, composition and chemical bonding of alumina coatings have been performed. Alumina coatings have been deposited by both ionized reactive magnetron sputtering (IMS) and conventional reactive magnetron sputtering (CMS) in an argon/oxygen discharge onto stainless steel coated silicon substrates. X-ray diffraction (XRD) was used for the phase analysis, and nanoindentation was used to evaluate the mechanical properties.

Substrate temperature during deposition was $<500^{\circ}\text{C}$, which is the technologically interesting temperature range to coat temperature sensitive substrates such as tool steels. Formation of the κ -phase was observed at 472°C . At substrate temperatures $< 472^{\circ}\text{C}$ evidence for the formation of the amorphous alumina phase was found. Films containing a mixture of κ and θ -alumina phases was grown at 430°C . The crystalline film hardness was 22 ± 1 GPa, which is equivalent to values reported for alumina films deposited by Chemical Vapor Deposition (CVD). Films grown at the same temperature by conventional magnetron sputtering were X-ray amorphous, and the hardness was found to be strong function of the substrate temperature.

Furthermore, a novel, very high rate reactive magnetron sputtering deposition process for alumina hard coatings at substrate temperature $\leq 250^{\circ}\text{C}$ has been developed. Utilizing pulsed D.C. power to sputter $\text{Al}+\text{AlO}_x$

off the target surface and partial pressure control of the reactive gas to maintain a certain partial pressure value (accuracy of better than 0.005 mTorr), fully dense, transparent alumina coatings could be produced at 76% of the metal deposition rate. The coatings have an elastic modulus of 140 GPa, a hardness of 12 GPa, a chemical composition close to stoichiometric, and a refractive index of 1.65.

Acknowledgments

I would like to thank my thesis advisor Prof. Allan Matthews for his guidance, support and patience over the last 5 years. Dr. Bill Sproul is gratefully acknowledged for his encouragement, guidance and support whilst head of the BIRL PVD group. My friend and tutor Dr. Andrey Voevodin is acknowledged for inspiring and stimulating discussions on thin films research and life.

I would like to thank all members of the BIRL PVD group for helping me with my work. Especially Tony Lefkow for help with practical problems, and for many interesting discussions on history.

Excellent collaboration is acknowledge with all my friends in the RCSE in Hull, in particular with Claus Rebholz.

I am grateful to my room mates Dr. Brian Swift and Dr. Kevin Peters for looking after me, over the last two years, and keeping the fridge stacked with Strohs.

Most importantly I would like to thank my family: My parents, sister and grandparents, for support and encouragement throughout my studies.

This work was supported by the US Air Force Office of Scientific Research (AFOSR), grant number F49620-95-0177.

Table of Contents

I. Introduction and Review	1
I.1 Why is there an Interest in Alumina Coatings?.....	1
I.2 How can Alumina Coatings be Produced?.....	4
I.2.1 Chemical Vapor Deposition (CVD).....	4
I.2.2 Physical Vapor Deposition (PVD).....	6
I.3 Structure of PVD Coatings	7
I.4 Magnetron Sputtering.....	12
I.4.1 Sputtering and Magnetron Sputtering.....	12
I.4.2 Reactive Magnetron Sputtering.....	16
I.4.2.1 Effect of the Reactive Gas at the Target.....	16
I.4.2.2 Effect of the Reactive Gas on the Deposition Rate.....	19
I.4.2.3 Reactive Magnetron Sputtering of Non- Conductive Materials	19
I.4.3 Pulsed D.C. Magnetron Sputtering.....	22
I.4.4 Process Control of Reactive Magnetron Sputtering	24
I.4.4.1 Why is Process Control needed in Reactive Magnetron Sputtering?.....	24
I.4.4.2 How can the Reactive Sputtering Process be Controlled?	25
I.4.4.3 The Complete Separation of Reactive Gas from the Target	26
I.4.4.4 Pulsing the Reactive Gas Flow	27
I.4.4.5 Optical Emission Control	27
I.4.4.5 Target Voltage and Target Current Control	28

I.4.4.6 Reactive Gas Partial Pressure Control	28
I.5 Ionized PVD techniques	30
I.6 Alumina Deposited by PVD.....	33
II. Methods of Research.....	37
II.1 Conventional Magnetron Sputtering	38
II.2 Ionized magnetron sputtering system	40
II.3 Nanoindentation.....	48
II.3.1 Hardness Measurement	48
II.3.2 Tip Correction.....	51
II.3.3 Elastic Modulus.....	53
II.3.4 Implementation.....	53
II.4 X-Ray Diffraction (XRD)	54
II.5 Field Emission Scanning Electron Microscopy (FESEM).....	54
II.6 Scanning Auger Microprobe (SAM).....	54
II.7 X-Ray Photoelectron Spectroscopy (XPS).....	55
II.7 Spectrophotometer.....	55
III. High Rate Deposition of Alumina	56
III.1 Deposition Rate.....	56
III.2 Optical Properties.....	60
III.3 Chemical Composition	62
III.4 Mechanical Properties	65
III.5 Microstructure.....	68
IV. Initial Phase Formation Studies - Conventional Magnetron Sputtering.....	70
IV.1 Influence of Energetic Neutrals.....	70
IV.2 Influence of Ion Bombardment at Different Substrate Temperatures	73

V. Ionized Magnetron Sputtering.....	75
V.1 Influence of the Substrate Temperature	76
V.2 The Influence of the Ion Current Density	83
V.3 Influence of the Substrate Bias Potential	99
VI. Chromia - Alumina Coatings, Composite or Solid Solution?	107
VI.1 Magnetron Sputtering of Chromia	107
VI.2 Magnetron Sputtering of Chromia-Alumina Films.....	110
VI. Conclusions and Future Directions.....	114
VI.1 Summary and Conclusions.....	114
VI.1.1 High Rate Deposition of Alumina.....	115
VI.1.2 Phase Formation Studies - Ionized Magnetron Sputtering.....	117
VI.3 Future Directions - Ways to Crystalline Low Temperature Alumina.....	120
VI.3.1 Ionized Aluminum Route	120
VI.3.2 Alloying, or Multilayer Route	121
VI.3.3 High Energetic Neutral Route	121

List of Figures

Figure I.1.1a: Unit cell of α -alumina.....	2
Figure I.1.1b: Unit cell of κ -alumina.....	2
Figure I.3.1: Structure Zone Model proposed by Movchan and Demchishin.....	8
Figure I.3.2: Structure Zone Model proposed by Thornton.....	8
Figure I.3.3: Typical micro structure obtained for condensing Ni vapor atoms arriving under normal incidence (a) without ion bombardment, (b) with 50 eV Ar, $j_i/j_a=0.04$, $\alpha=30^\circ$, (c) with 50 eV Ar, $j_i/j_a=0.16$, $\alpha=30^\circ$ after Mueller.....	10
Figure I.3.4: Refractive Index versus O_2^+ ion current density of alumina films produced at $T<150^\circ C$ after Williamson et al.....	11
Figure I.3.5: Refractive Index versus deposition rate at different target power settings taken from Shih and Dove.....	11
Figure I.4.1: Schematic of the sputtering Process after Thornton[32].....	13
Figure I.4.2: A Schematic of a Magnetron.....	14
Figure I.4.3: Schematic of a type I and type II magnetrons after Windows and Savvides[33,34].....	14

Figure I.4.4: Oxygen partial pressure and target voltage versus oxygen flow, while a constant flow is maintained.....	18
Figure I.4.5: D.C. sputtering of a non-conduct material, and subsequent charge accumulation.....	21
Figure I.4.6: Reactive Sputtering with pulsed D.C. power: (a) physical sputtering, and charge accumulation occur; (b) insulating compound surface is discharged.....	23
Figure I.4.7a: Alumina target voltage versus oxygen partial pressure.....	29
Figure I.4.7b: Chromia target voltage versus oxygen partial pressure.....	29
Figure I.5.1a: Relative ionization level of the sputtered Al as a function of the chamber pressure for Ar and Ne working gases, after Rossnagel and Hopwood.....	32
Figure I.5.1b: Relative ionization level of the sputtered Al as a function of the R.F. coil power at different source power settings, after Rossnagel and Hopwood.....	31
Figure II.1.1: Schematic of the opposed cathode closed-field unbalanced magnetron sputtering system.....	39
Figure II.2.1: Conventional Magnetron Sputtering System.....	41

Figure II.2.2: Schematic drawing of the ionized magnetron sputtering system.....	42
Figure II.2.3: Relative films thickness versus the distance to the centerline of the magnetron.....	44
Figure II.2.4: Target voltage versus O ₂ flow characteristic.....	45
Figure II.2.5: Substrate bias voltage versus time plot for a typical samples produced by ionized magnetron sputtering.....	47
Figure II.3.1: Load displacement curve of sapphire at a load of 4 mN.....	49
Figure II.3.2: The corrected plastic penetration depth (h_{pc}) versus the plastic penetration depth (h_p).....	52
Figure III.1: AlO _x hysteresis curve @ 3kW target power, 1kW R.F. substrate bias power and 5 mTorr total pressure.....	58
Figure III.2: AlO _x hysteresis curve with deposition rate information @ 3kW target power, 1kW R.F. substrate bias power and 5 mTorr total pressure.....	59
Figure III.3: Transmission versus wavelength for AlO _x coatings produced at various oxygen partial pressures.....	61

Figure III.4: Scanning Auger Microprobe oxygen to alumina intensity ratio versus deposition rate relative to the metal rate.....	64
Figure III.5: Load displacement curve of a typical amorphous alumina film and the sapphire standard used for calibration.....	66
Figure III.6: Elastic modulus and hardness versus AlO_x/Al deposition rate ratio.....	67
Figure III.7: Fracture cross-section of the sample produced at 92% of the metal rate by field emission scanning electron microscopy.....	69
Figure IV.1: Hardness and Elastic modulus by nanoindentation versus Total Pressure for Magnetron Sputtering with Floating Substrates at $T_s < 98^\circ C$	72
Figure IV.2: Hardness versus Substrate Temperature for Conventional Magnetron Sputtering, with and without Substrate Bias.....	74
Figure V.1.1: Schematic - Substrate Temperature versus Deposition Technology.....	77
Figure V.1.2: Hardness versus Substrate Temperature, for ionized magnetron sputtering (IMS) at 30 mTorr total pressure, with and without substrate bias.....	79
Figure V.1.3: θ - 2θ Scans versus Substrate Temperature at $T_s=300^\circ C$ and $T_s=472^\circ C$	81

Figure V.1.4: Morphology and RA versus Substrate Temperature at 30 mTorr Total Pressure and -70V Average Substrate Bias Potential.....	82
Figure V.2.1: Substrate ion current density versus R.F. coil power.....	84
Figure V.2.2: Bragg-Brentano diffractogram of stainless steel coated silicon, used as substrate for all experiments.....	87
Figure V.2.3: Bragg-Brentano diffractogram of κ -alumina deposited at an ion current density of 3.6 mA^{-2}	88
Figure V.2.4: Bragg-Brentano diffractogram of κ -and θ -alumina deposited at an ion current density of 4.9 mA cm^{-2}	89
Figure V.2.5: Bragg-Brentano diffractogram of κ -and θ -alumina deposited at an ion current density of 5.9 mA cm^{-2}	90
Figure V.2.6: Bragg-Brentano diffractogram of κ -and θ -alumina deposited at an ion current density of 25.6 mA cm^{-2}	91
Figure V.2.7: Load displacement curves for the sapphire bulk standard and a alumina coating produced at an ion current density of 4.9 mA cm^{-2}	93
Figure V.2.8: XPS Al 2p binding energy.....	95
Figure V.2.9: XPS Al/O concentration ratio versus substrate ion current density.....	96

Figure V.2.10: Field emission scanning electron microscopy (FESEM) cross-section of a sample deposited at an ion current density of 25.6 mA cm^{-2}	98
Figure V.3.1: Substrate ion current density versus deposition rate.....	100
Figure V.3.2: Bragg-Brentano diffractogram of stainless steel coated silicon, which was used as the substrate for all experiments.....	102
Figure V.3.3: Bragg-Brentano diffractogram of θ -alumina deposited at -40V substrate bias potential and 180°C	103
Figure V.3.4: Bragg-Brentano diffractogram of $\kappa+\theta$ -alumina deposited at -70V substrate bias potential and 320°C	104
Figure V.3.5: Bragg-Brentano diffractogram of amorphous alumina deposited at -90V substrate bias potential and 240°C	105
Figure VI.1.1: θ - 2θ scans of CrO_x films produced at various oxygen partial pressure values.....	108
Figure VI.1.2: High resolution θ - 2θ scan of the film grown at 1 mTorr oxygen partial pressure.....	109
Figure VI.2.1: θ - 2θ scan of an $\text{AlO}_x\text{-CrO}_x$ film (target composition 23 at% Al, substrate temperature= 220°C).....	111

Figure VI.2.2: θ - 2θ scan of an $\text{AlO}_x\text{-CrO}_x$ film (target composition 50 at% Al, substrate Temperature= 220°C).....112

Figure VI.2.3: (300) interplanar spacing of the produced coatings versus the Al to Cr ratio of the target.....113

Figure VII.1: State of the art in high rate deposition of alumina coatings...116

Figure VII.2: Phases identified by XRD as a function of substrate temperature and ion current density.....118

I. Introduction and Review

I.1 Why is there an Interest in Alumina Coatings?

The current interest in the deposition of alumina coatings is due to the unique properties that this material exhibits. α -alumina exhibits chemical and mechanical stability even at temperatures of up to 1000°C and has a melting point of 2053°C¹. The hardness of alumina is the highest of all oxides. It is insoluble in inorganic acids, and only gets attacked in boiling hydrofluoric acid and molten salts at temperature greater than 1000°C². Due to its chemical inertness and wear resistance at high temperatures the main commercial use of alumina hard coatings lies in tool coatings for demanding cutting applications like high speed (10 m/sec) turning and milling of cast iron and low carbon steels^{3,4}, as well as in protective coatings for magnetic head sliders³.

Alumina is a polymorphous material. α -alumina is the only thermodynamically stable phase in the aluminum oxygen system and crystallizes in a rhombohedral structure and can be described as O²⁻ ions in the approximately hexagonal closed packed arrangement and Al³⁺ ions occupying two thirds of the octahedral interstices (see Figure I.1a). Liu and Skogsmo suggested a orthorhombic structure for κ -alumina on the basis of their convergent-beam electron diffraction experiments⁵ (see Figure I.1b). Other alumina phases frequently observed in PVD coatings are cubic γ -alumina, tetragonal delta and monoclinic τ -alumina, see for example reference ⁶ and references therein.

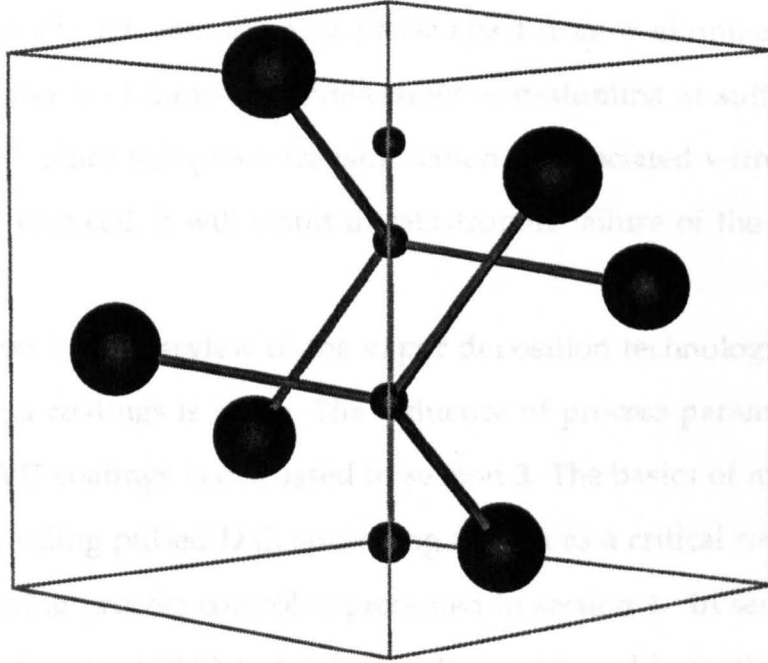


Figure I.1.1a: Unit cell of α -alumina

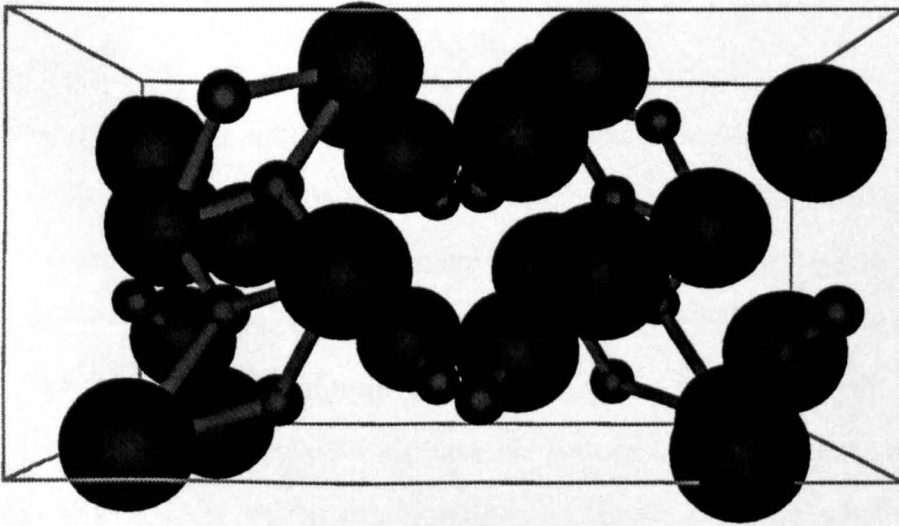


Figure I.1.1b: Unit cell of κ -alumina

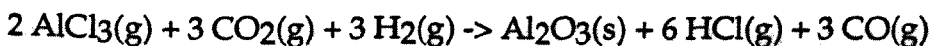
The CVD formation of α , κ and τ -alumina has been reported^{7,8}. κ -alumina is the only practically relevant alumina phase apart from α -alumina⁹. All metastable phases will transform irreversibly to α -alumina at sufficiently high temperatures¹⁰. Since this phase transformation is associated with a change in volume of the unit cell, it will result in catastrophic failure of the coating.

In section 2 an overview of the vapor deposition technologies used to deposit alumina coatings is given. The influence of process parameters on the structure of PVD coatings is discussed in section 3. The basics of magnetron sputtering, including pulsed D.C. sputtering as well as a critical review of reactive sputtering process control is presented in section 4. In section 5 the development of ionized PVD technologies discussed, and in section 6 the state of the art in the deposition of alumina by PVD is critically reviewed.

I.2 How can Alumina Coatings be Produced?

I.2.1 Chemical Vapor Deposition (CVD)

The general principle of the CVD technique involves contact between the vapor of a volatile compound (mainly halides or metal carbonyls) and the substrate surface. The sample temperature provides the energy necessary to induce a chemical reaction giving a solid product when this thermal energy is sufficiently high. A resulting disadvantage is the limited use of this technology other than for substrates of high thermal stability. There is also an environmental concern with this type of technology due to the reaction products. Chemically vapor deposited layers of alumina have been extensively worked on since the early seventies^{7,8,11,12}. The process is based on the hydrolysis of aluminum chloride:



If the substrate temperature is $> 950^\circ\text{C}$, α and or κ -alumina (occasionally also τ) is produced. The substrate material is usually cemented carbide. To prevent disturbances during growth caused by substrate elements such as Co and C, which in turn can result in inferior mechanical properties a interlayer is usually deposited. TiC and TiN are commonly used as interlayers^{13,14}.

It is well established that the phase content of CVD alumina coatings is strongly influenced by the nucleation surface^{13,15}. However there are conflicting reports on how the nucleation surface influences the phase content. Chemical composition and therefore lattice parameter of a fcc binding layer consisting of Ti and Al have been shown to influence the phase content of the coating. Chatfield et al suggested that TiC will oxidise in air or by excess water in the gas

phase during nucleation of alumina. The oxidized TiC surface will favor growth of α -alumina while a 'clean' TiC surface will favor κ -alumina due to the epitaxial relationship of (0001) κ -alumina // (1-11) TiC [10-10] κ -alumina // [110]TiC¹³. Halvarsson and Vurionen¹⁵ could not observe the formation of Ti₂O₃ on the TiC, and reported epitaxial growth of κ -alumina on TiCN and α -alumina on Ti₂O₃. The same group studied the influence of Ti/Al bonding layers. They found growth of κ and α -alumina on bonding layers which could not be distinguished between in terms of chemical composition and lattice parameter, suggesting that there are other important factors such as crystal facets of importance to the growth¹⁶. Selective growth of either the κ or α -phase can also be achieved by using different Al/Ti ratios for the so called bonding layer¹⁴. κ -alumina generally consists of a submicron columnar grown crystallites, α -alumina on the other hand grows in micrometer size equiaxed crystallites¹⁴. It was also found that impurities such as C, Si and air leaks enhances the transformation of κ to α -alumina¹⁷. Although κ and α -alumina coatings are commercially available for well over 17 years, the factors governing nucleation of alumina are not well understood.

I.2.2 Physical Vapor Deposition (PVD)

Physical Vapor Deposition (PVD) can be divided into two main groups, evaporation and sputtering. In evaporation the vapor is created by resistive or electron beam heating. The vapor condenses at the substrate and forms the coating. If reactive gas is added compounds can be formed.

In sputtering the coating material is transferred to the vapor phase by inert gas ion bombardment. When these energetic ions impact the surface, material (atoms and clusters) are ejected by momentum transfer. The energy of the sputtered vapor is higher than that of the evaporated vapor (factor 10 to 100). As in evaporation, a reactive process is possible.

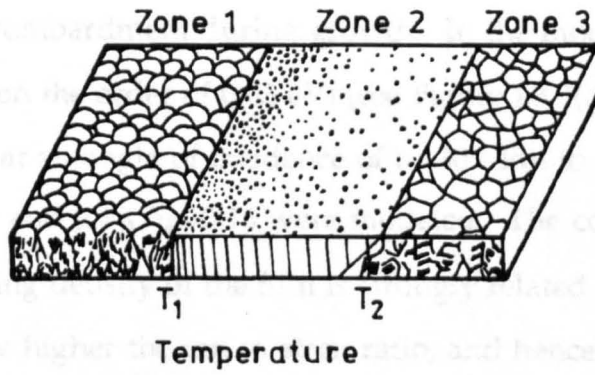
In the sections 4 and 5 of this chapter, a more detailed description of reactive magnetron sputtering and ionized PVD techniques are given. For a general description of PVD processes the reader is referred to "Thin Film Processes II"¹⁸ edited by J.L. Vossen and W. Kern, the "Handbook of Plasma Processing Technology"¹⁹ edited by S.M. Rossnagel, J.J. Cuomo and W.D. Westwood, "Advanced Surface Coatings - A Handbook of Surface Engineering"²⁰ edited by D.S. Rickerby and A. Matthews and the "Handbook of Ion Beam Processing Technology" edited by J.J. Cuomo, S.M. Rossnagel and H.R. Kaufman²¹.

I.3 Structure of PVD Coatings

The structure of PVD coatings is influenced by the energy, mass, flux and angle of incidence of the bombarding particles. Also of importance is the influence of non-energetic particles i.e. depositing or absorbing species. Movchan and Demchishin were the first to correlate the micro structure of coatings produced by thermal evaporation with T/T_m (T being the substrate temperature and T_m the melting point of the evaporated material). They found that depending on T/T_m the micro structure can be described by three zones (see Figure I.3.1), each with their individual morphological characteristics and physical properties.

Thornton²² modified this model for the sputter deposition of coatings, taking the higher energy of sputtered atoms (5-25 eV as opposed to evaporation with 0.1 eV), and the possible loss of this energy due to scattering in the gas phase into account, by defining zones as a function of temperature and total pressure, as can be seen in Figure I.3.2)

Further modification of the empirical models were proposed by Messier, Giri and Roy²³, including bombardment effects to the thermal mobility effects on the morphology of the coating, during ion assisted deposition.



	Zone 1	Zone 2	Zone 3
Metals	$< 0.3 T_m$	$0.3 - 0.45 T_m$	$> 0.45 T_m$
Oxides	$< 0.26 T_m$	$0.26 - 0.45 T_m$	$> 0.45 T_m$

Figure I.3.1: Structure Zone Model proposed by Movchan and Demchishin²⁴

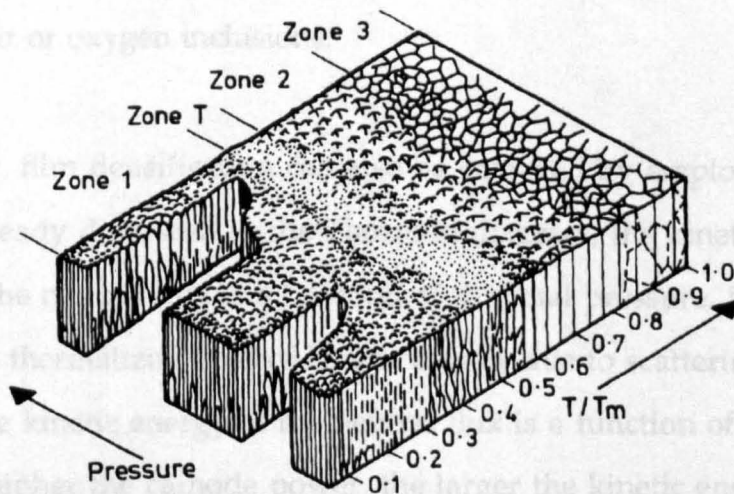


Figure I.3.2: Structure Zone Model proposed by Thornton²²

Mueller²⁵ employed molecular dynamics calculations for the simulation of the effect of ion bombardment during growth. In the model Ni is thermally evaporated (energy on the order of 0.03 eV) (see Figure I.3.3(a) and bombarded with 50 eV Ar ions, at an angle of incidence of $\alpha=30^\circ$. Ion to neutral flux ratios j_i/j_a of (b) $j_i/j_a=0.04$ and (c) $j_i/j_a=0.16$ were modeled. The computer simulation shows that the packing density of the film is strongly related to the energy per deposited atom. The higher the ion to atom ratio, and hence the energy at the surface, the larger the packing density

Experimental evidence for Muellers modeling results in general, and for the densification of alumina films in particular is given by Williams et al²⁶. The film packing density is related to the refractive index and was increased from 80% to 92% by increasing the flux of O_2^+ ions at 300 eV from 0 to $100 \mu A cm^{-2}$, as can be seen in Figure I.3.4. The density was correlated to the measured refractive index by Maxwell-Garnett²⁷, based on the assumption the film density is reduced by air or oxygen inclusions.

Similarly, film densification can also be achieved by employing energetic neutrals: As already discussed in the Thornton diagram, the kinetic energy component of the neutral flux is a function of the total pressure. If the sputtered flux is not fully thermalized (loss of kinetic energy due to scattering collisions²⁸), the kinetic energy of the neutral flux is a function of the cathode potential. The higher the cathode power, the larger the kinetic energy component of the neutral flux. Shih and Dove²⁹ found that the refractive index of R.F. sputtered alumina films is high, if a high power is supplied to the magnetron. The results are shown in Figure I.3.5 where the target power is drawn versus the refractive index.

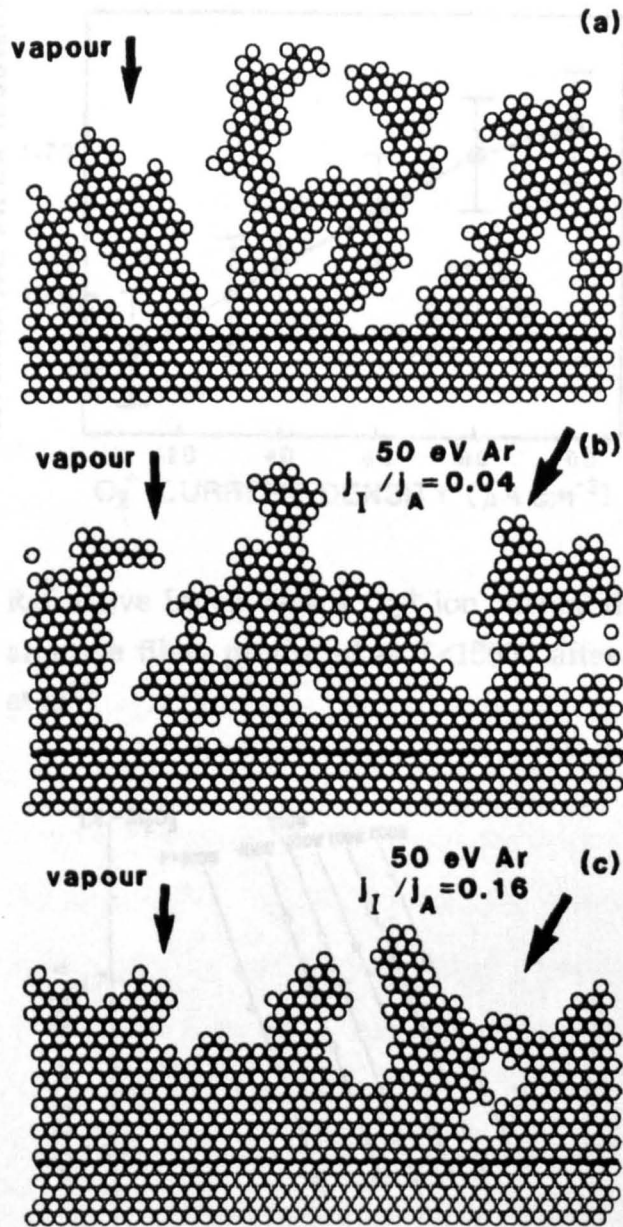


Figure I.3.3: Typical micro structure obtained for condensing Ni vapor atoms arriving under normal incidence (a) without ion bombardment, (b) with 50 eV Ar, $j_I/j_A=0.04$, $\alpha=30^\circ$, (c) with 50 eV Ar, $j_I/j_A=0.16$, $\alpha=30^\circ$ after Mueller²⁵

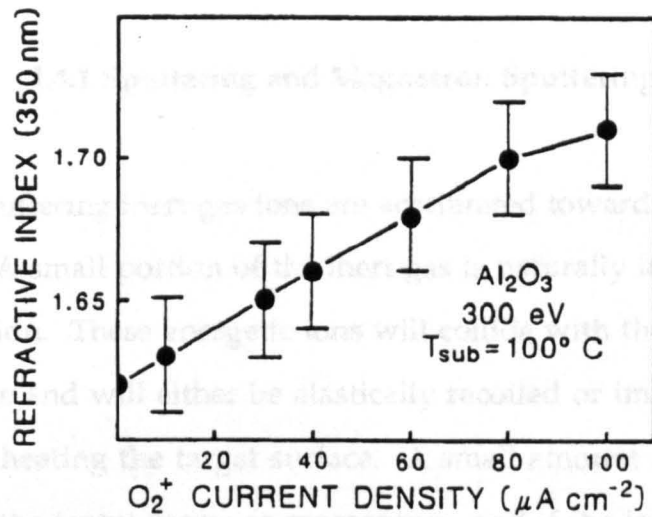


Figure I.3.4: Refractive Index versus O₂⁺ ion current density of alumina films produced at T<150°C after Williamson et al²⁶

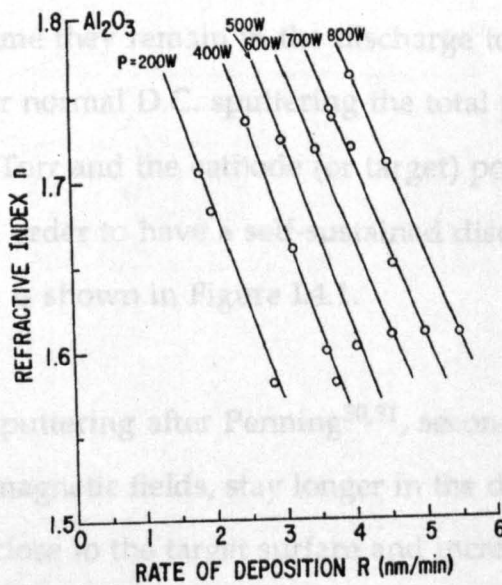


Figure I.3.5: Refractive Index versus deposition rate at different target power settings taken from Shih and Dove²⁹

I.4 Magnetron Sputtering

I.4.1 Sputtering and Magnetron Sputtering

In D.C. sputtering inert gas ions are accelerated towards a negatively charged target. A small portion of the inert gas is naturally ionized, or ionized by cosmic radiation. These energetic ions will collide with the target surface, lose their charge and will either be elastically recoiled or implanted. This will mainly result in heating the target surface. A small amount of energy however is transferred to the target atoms as momentum, and if the local binding energy can be overcome, atoms and or clusters will be emitted. Furthermore so called secondary electrons may be ejected, which cause ionizing collisions on their way to the anode (usually the chamber walls). This mechanism sustains the discharge. Since the electrons have a very small mass, they are easily accelerated, and the time they remain in the discharge to cause ionizing collisions is small. For normal D.C. sputtering the total pressure has to be on the order of tens of mTorr and the cathode (or target) potential is on the order of thousands of Volts, in order to have a self-sustained discharge. A schematic of the sputtering process is shown in Figure I.4.1.

In magnetron sputtering after Penning^{30,31}, secondary electrons are trapped by means of magnetic fields, stay longer in the discharge (increased electron path length) close to the target surface and increase the probability of an ionization event (see Figure I.4.2). More ions in the vicinity of the target results in a higher Ar ion flux to the target and hence in a higher deposition rate. The total pressure can be as low as 1 mTorr and target potentials are on the order of hundreds of V.

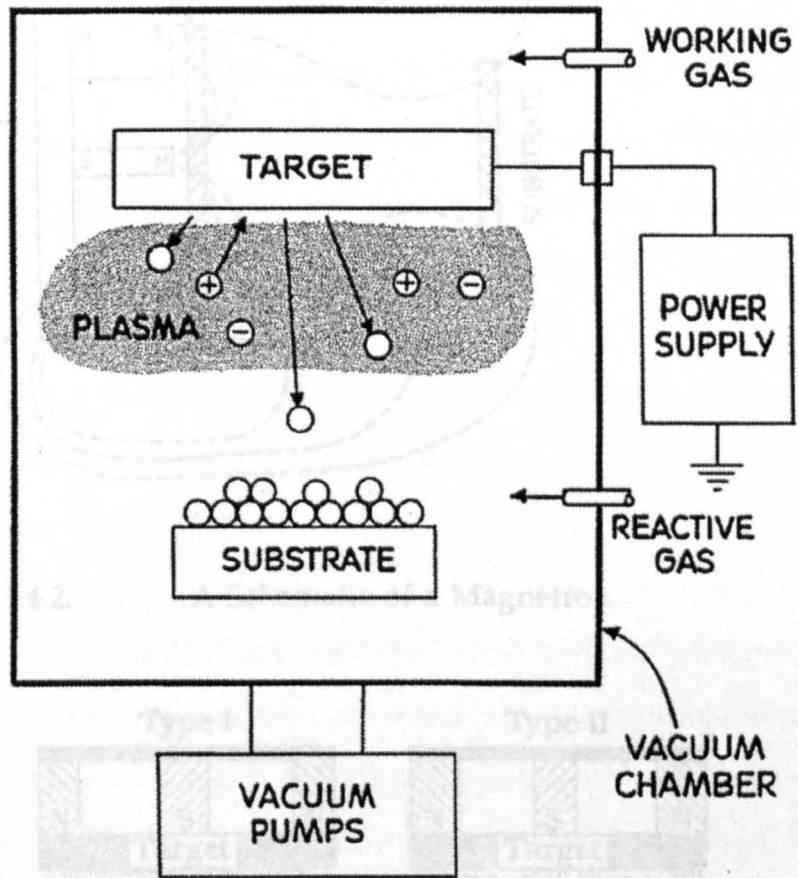


Figure I.4.1: Schematic of the sputtering Process after Thornton³²

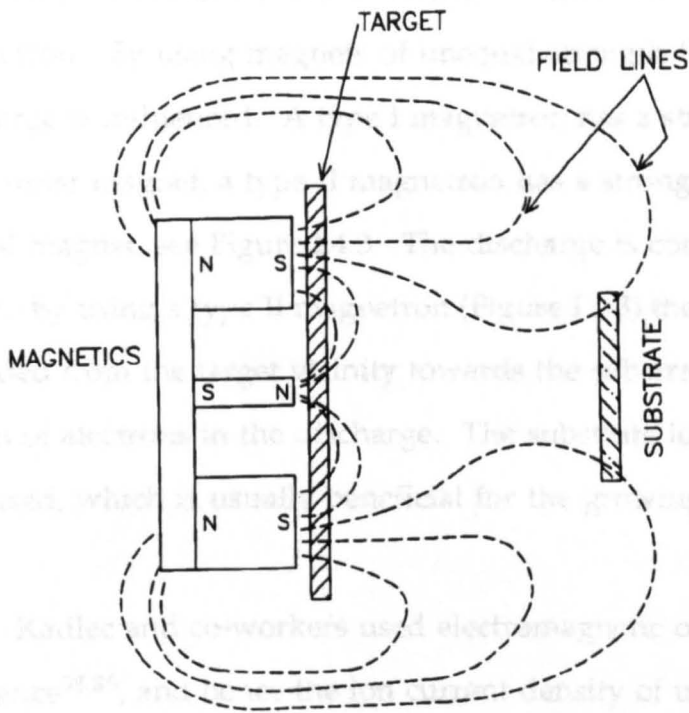


Figure I.4.2: A Schematic of a Magnetron

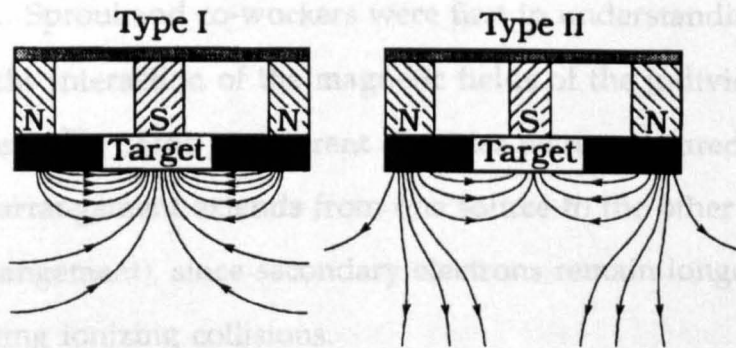


Figure I.4.3: Schematic of a type I and type II magnetrons after Windows and Savvides^{33,34}

In 1986 Windows and Savvides^{33,34} introduced the unbalanced magnetron. By using magnets of unequal strength the electron density in the discharge is influenced. A type I magnetron has a strong central magnet and a weak outer magnet, a type II magnetron has a strong outer magnet and a weak central magnet, see Figure I.4.3. The discharge is confined to the vicinity of the target. By using a type II magnetron (Figure I.4.3) the discharge region can be extended from the target vicinity towards the substrate, by increasing the path length of electrons in the discharge. The substrate ion current density is increased, which is usually beneficial for the growing film.

Kadlec and co-workers used electromagnetic coils to alter the degree of imbalance^{35,36}, and hence the ion current density of up to 6 mA cm^{-2} at a source to substrate distance of 200 mm ³⁷.

Experiments with multiple sources were carried out to increase the deposition rate. Sproul and co-workers were first in understanding the importance of the interaction of the magnetic fields of the individual magnetron sources³⁸. Large ion current densities were measured³⁹ when the magnetic field arrangement extends from one source to the other (so called closed filed arrangement), since secondary electrons remain longer in the discharge, causing ionizing collisions.

I.4.2 Reactive Magnetron Sputtering

Reactive sputtering deals with sputtering in reactive gas or a mixture of reactive gas and inert gas atmosphere. The formation of a compound, the reaction product of the sputtered flux and the reactive gas, is desired. Many reviews have been written on reactive sputtering^{40,41} and reactive magnetron sputtering^{42,43}. Today, many complex compounds and multilayered designs can be realized with reactive magnetron sputtering. Deposition rates close to that of the pure sputtered material can be achieved for both conductive⁴⁴ and non conductive materials, as demonstrated in chapter 3 of this thesis.

I.4.2.1 Effect of the Reactive Gas at the Target

In reactive magnetron sputtering, the reactive gas can form a compound layer on the target surface. If the compound formed as reaction product of the target material with the reactive gas has a higher secondary electron emission coefficient, than the pure target material this will result in a reduction of the plasma impedance and the target potential, if the target current is kept constant. The target current constitutes the sum of the ion current impacting on the target and the electron current. Hence, the ionic component of the current is reduced as the electron current is increased. The formation of a compound layer on the target surface results in a lower deposition rate, since less ions, with lower energy bombard the target surface. In addition most compounds have a lower sputtering yield as the pure target material, when they are bombarded by ions of equal energy, which reduces the sputtered flux, and hence the net deposition rate, even further.

In the past, researchers distinguished between two different sputter modes⁴³: Firstly sputtering of a metallic target, at low reactive gas partial pressures, and secondly sputtering from the compound target (or poisoned target), at large reactive gas partial pressures, as described in the beginning of this section. It was believed, that at a certain transition point⁴⁵⁻⁴⁹ the target changes from the metallic sputtering mode into the poisoned mode. Heller⁴⁷ and Goranchev et al^{48,49} showed that the sputtering mode can be identified from the target current/voltage characteristic.

In Figure I.4.4 the transition between the metallic- and the poisoned sputter mode is shown for reactive sputtering of aluminum in a oxygen argon ambient. The oxygen flow is maintained constant, and the oxygen partial pressure values as well as the target voltage values are recorded. The transition is marked by a sharp increase of the pO_2 , and a sharp drop of the target voltage, as the flow is increased.

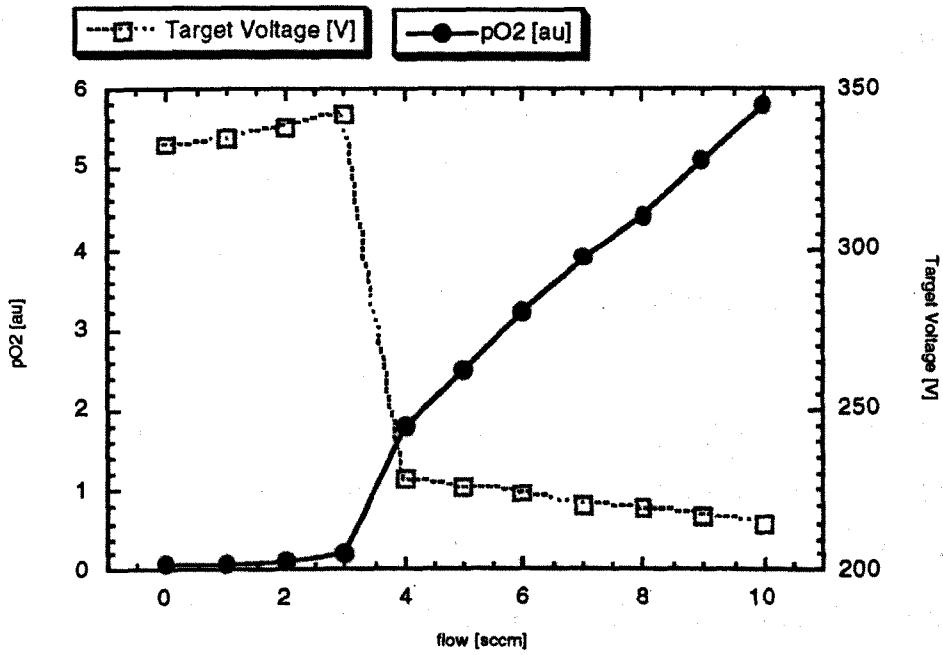


Figure I.4.4: Oxygen partial pressure and target voltage versus oxygen flow, while a constant flow is maintained

Schiller et al⁵⁰ showed that the transition point can in fact be transition region, in the past frequently referred to as the 'unstable region', due to the fact that stable long term operation was not possible in this region. However it was quickly realized, that this region is of high technological significance, if the deposition of stoichiometric compounds at high rate is desired. The efforts that have been made to access this region, and deposit coatings at high rate, with a certain chemical composition is discussed in detail in section I.4.4.

I.4.2.2 Effect of the Reactive Gas on the Deposition Rate

Sproul et al demonstrated, that by employing a adequate control technique, the deposition of transition metal-nitrides^{51,52} and carbides⁴⁴ could be carried out in the 'unstable' region. For example the formation of stoichiometric TiN was reported at 100%, and HfN and ZrN at 95% of the metal deposition rate⁵¹. High rate deposition with precise control of the coatings stoichiometry was achieved by maintaining a certain partial pressure value of the reactive gas precisely, throughout the deposition process. At constant reactive gas partial pressure, the sputtered flux is kept constant automatically, and the chemical composition and film homogeneity is maintained.

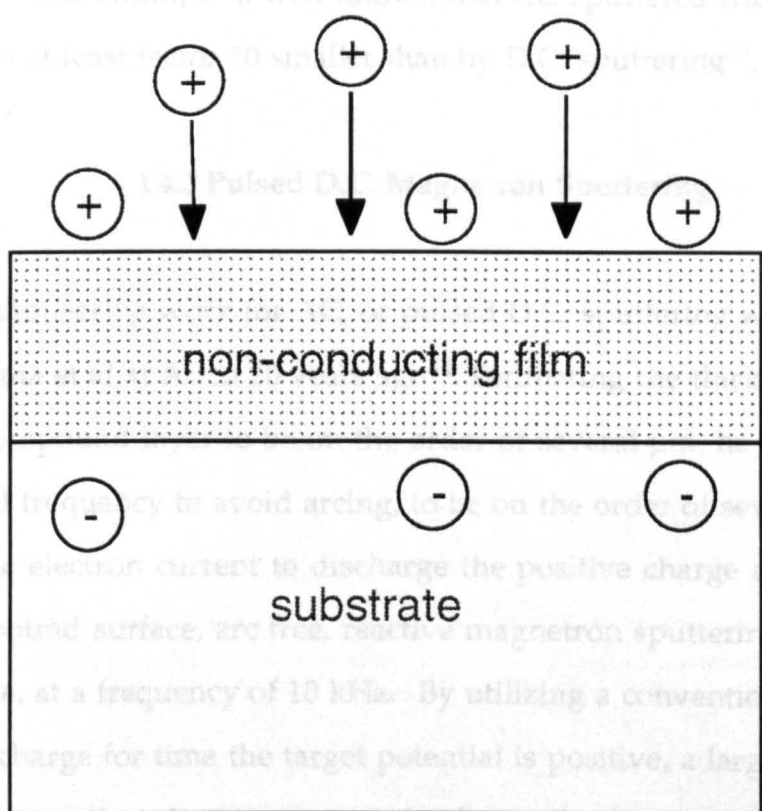
I.4.2.3 Reactive Magnetron Sputtering of Non-Conductive Materials

The reactive gas partial pressure required for the formation of a particular stoichiometric compound may result in a partly reacted target surface. Stable operation of the sputter source can be maintained, if formed compound is a conductor. In the case of a non conductive compound layer,

such as TiO_2 , AlN or Al_2O_3 , the positive ions impinging on the target, can not be neutralized by electrons from the target, which leads to charge accumulation, as shown in Figure I.5.

Electrically this represents a capacitor. If the dielectric strength of the compound is larger than the potential difference between the dark space side and target side of the compound layer, more and more charge is accumulated. At the same time the voltage drop across the cathode dark space is reduced to the point where the impinging ions are too low in energy to cause sputtering. If the dielectric strength of the compound layer is smaller than the potential difference between the dark space side and the target side of the insulating layer, the compound layer will break down, which leads to the concentration of a large part of the discharge current in small surface volume segment, and causes local evaporation. This process is known as 'arc evaporation' of the target material, and is accompanied by two undesirable effects: The ejection of droplets, leading to inhomogeneity and defects in the film, and a drastic change in processing parameters, such as cathode potential and the vapor to reactive gas concentration ratio. This represents a problem for the control of the sputtering process, and generally leads to instabilities.

The process of A.C. sputtering or pulsed D.C. sputtering of non-conducting materials such as alumina or zirconia were mainly deposited by R.F. sputtering. Since the sputter yield of, for example, alumina is lower than that of metallic substrates, it is well known that the sputtered flux using R.F. sputtering is at least 10 times less than by D.C. sputtering.



negative DC substrate bias potential

The basic idea of this potential is illustrated in Figure I.4.6a and b. The actual process is split into two sub processes. During one negative part of the period the target potential is positive, a large positive voltage is required at the target, to maintain the discharge. Simultaneous sputtering of the anode

Figure I.4.5: D.C. sputtering of a non-conduct material, and subsequent charge accumulation

Until the advent of A.C. sputtering or pulsed D.C. sputtering, insulating films such as alumina or zirconia were mainly deposited by R.F. sputtering. Since the sputter yield of, for example, alumina is lower than the yield for aluminum, it is well known that the sputtered flux using R.F. sputtering is at least factor 10 smaller than by D.C. sputtering⁵³.

I.4.3 Pulsed D.C. Magnetron Sputtering

The pioneering work for AC, or pulsed D.C. sputtering was carried out by Corima et al at Airco 20 years ago⁵⁴. Estimating the thickness of the dielectric compound layer to be on the order of several μm , he calculated the required frequency to avoid arcing, to be on the order of several kHz. Utilizing the electron current to discharge the positive charge accumulated at the compound surface, arc free, reactive magnetron sputtering of TiO_2 was possible, at a frequency of 10 kHz. By utilizing a conventional anode, to create a discharge for time the target potential is positive, a large positive voltage is required at the target, to maintain the diode mode. Simultaneous sputtering of the anode occurs.

The basic idea of this patent is illustrated in Figure I.4.6a and b. The actual process is split into two sub processes. During one negative part of the period, the sputtered vapor is created, during the positive part of the period, the accumulated charge on the insulating surface is discharged.

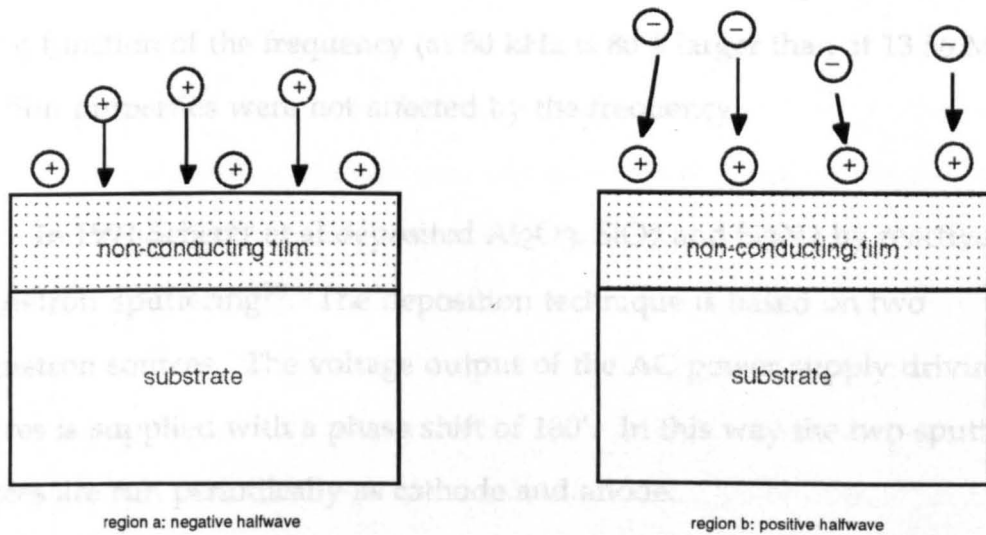


Figure I.4.6: Reactive Sputtering with pulsed D.C. power: (a) physical sputtering, and charge accumulation occur; (b) insulating compound surface is discharged

In 1986 to 1988 patents were issued in both former East-⁵⁵ and West-Germany⁵⁶ for pulsed power in the kHz frequency range. In the same time period, Este and Westwood⁵⁷ published their work on rate enhanced sputtering of dielectric material by a 'quasi-direct-current sputtering technique'. AlN was sputtered utilizing frequencies in the range of 80 to 500 kHz and 13.56 MHz. They summarize that the AlN deposition rate is a strong function of the frequency (at 80 kHz is 80% larger than at 13.56 MHz). The film properties were not affected by the frequency.

In 1991 Scherer et al deposited Al₂O₃, SiO₂ and Si₃N₄ by reactive AC magnetron sputtering⁵⁸. The deposition technique is based on two magnetron sources. The voltage output of the AC power supply driving the sources is supplied with a phase shift of 180°. In this way the two sputter sources are run periodically as cathode and anode.

I.4.4 Process Control of Reactive Magnetron Sputtering

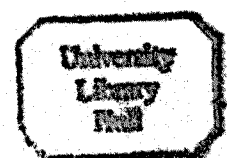
I.4.4.1 Why is Process Control needed in Reactive Magnetron Sputtering?

In section I.4.2 of this chapter it was discussed, that in reactive magnetron sputtering the reduction in deposition rate is believed to be due to the formation of a compound layer on the target surface and the reduced sputtering yield of the reactive gas molecules. For any industrial application, the deposition rate, or better the maximization of the deposition rate is of major importance. But not only the deposition rate, also the films properties show a strong dependence on the ratio of sputtered flux to reactive gas concentration, for example the refractive index of ITO⁵⁹

or the hardness and preferred orientation of TiN⁶⁰. The motivation for the development of reactive sputtering controllers is obvious: Firstly to control and in some cases maximize the deposition rate, and secondly to control the film stoichiometry, and hence micro structure and properties.

I.4.4.2 How can the Reactive Sputtering Process be Controlled?

Early work concerned with the mechanism of reactive sputtering, especially with the step like decrease of the deposition rate of metals sputtered in a reactive gas atmosphere^{46,61-63}, and basic investigations on the influence of a reactive gas on discharge current⁴⁷ and current - voltage characteristic^{48,49} were instrumental for the development of reactive sputtering controllers. Different control concepts have been suggested over the years: Separation of the reactive gas from the target by Schiller et al in 1979⁵⁰, pulsing of the reactive gas flow by Thornton in 1979⁶⁴, automatic feed back control of the reactive gas flow, using light emitted by the plasma by Chapin and Condon in 1979⁶⁵, the target voltage by Schiller in 1982⁶⁶, the total pressure by Ridge and Howson in 1982⁵⁹, the partial pressure of the reactive gas by Sproul et al in 1983^{51,52}, as control parameter. Also, light emitted by the plasma was used to control the power supplied to the cathode by Enjouji et al in 1983⁶⁷. It has been shown that the pumping speed can be increased beyond a critical value^{68,69}, no high powered controllers are necessary, because the transition from metal to compound sputter mode is a gradual transition. However, for high volume vacuum chambers, as employed for industrial application, the pumping rate requirements are large, and therefore rather expensive.



Some of these control concepts are still in use, others proved to be of limited use. The advantageous and disadvantageous of these control concepts are now discussed in detail and their further development and relevance is critically reviewed.

I.4.4.3 The Complete Separation of Reactive Gas from the Target

The complete separation of the reactive gas from the target, in a way that no compound film is formed was first suggested by Schiller in 1979⁵⁰. This can be achieved for TiO_2 and Ta_2O_5 by using the target voltage characteristic⁷⁰, to estimate the critical oxygen partial pressure range where sputtering in the metallic mode occurs. For compounds with a higher reactivity, variations of the basic idea was successfully employed. To increase the reactive gas concentration at the substrate, while sputtering of a metallic target, a slit or baffle arrangement was placed between source and substrate. Maniv, Miner and Westwood in 1981⁷¹ employed slits for the deposition of Cd_2SnO_4 . Este and Westwood in 1984⁷², Scherer and Wirtz 1984⁷³ employed a grid, Pang et al⁷⁴ employed an aperture arrangements for the deposition of alumina in 1989. All these techniques where mechanical grids and similar device are utilized, 60% to 90% of the sputtered flux is deposited on the grid⁵³. In 1989 Jones and Logan 1989⁵³ utilized a hallow cathode substrate holder, to activate the oxygen at the substrate, while sputtering off a metallic target, and produced stoichiometric alumina films, however this technology is developed for flat substrates, and difficult to utilize for three dimensional substrates.

I.4.4.4 Pulsing the Reactive Gas Flow

Pulsing the reactive gas flow as a method of control, was put forward by Thornton in 1979⁶⁴. As the reactive gas flow is pulsed (switched on then switched off), the target periodically cycles through the metallic state to the compound state. This technology was further developed by Aronson in 1980⁷⁵ and Sproul in 1984⁷⁶. Most recently Billard et al⁷⁷ pulsed the power supplied to the sputter source, essentially achieving the same effect, then pulsing the reactive gas; the target surface periodically cycles through the compound and metallic mode. While providing significant improvements in growth rate, 60% of the metal deposition rate for TiN was reported by Aronson⁷⁵, it is likely with all the pulsing techniques the produced films show chemical composition gradients, in the same frequency as the pulsing of the power or reactive gas flow takes place.

I.4.4.5 Optical Emission Control

An optical spectrometer was employed to control the reactive gas flow by Chapin in 1979⁶⁵. An optical wavelength is selected that is sensitive of the reactive gas partial pressure, has a sufficient peak to background ratio, and no peak overlap with other wavelengths. The concept was successfully employed by Schiller in 1987⁷⁸ and Howson in 1989⁷⁹ for the deposition of Indium Tin Oxide (ITO) and Indium Oxide, respectively. Enjouji 1983⁶⁷ employed an optical spectrometer to control the power supplied to the sputter source, and demonstrated control of the rate and stoichiometry for also for stoichiometry control of ITO.

I.4.4.5 Target Voltage and Target Current Control

Schiller suggested in 1982⁶⁶ to utilize the target voltage to control the reactive gas flow. Successful application was demonstrated for Cd_2SnO_4 by Schiller⁶⁶, and for AlN by Affinito and Parsons in 1984⁸⁰. Interestingly with the same setup the deposition of AlO_x films could not be realized.

Naturally, the target voltage versus reactive gas partial pressure characteristic is a function of materials involved in the process: Alumina for example shows one maximum and one minimum, whereas chromia shows two maxima and one minimum, as shown in Figure I.4.7a and b, respectively.

Alumina is an ideal material for voltage control, because a small oxygen partial pressure variation results in a large voltage change, and the voltage drops consistently as the oxygen partial pressure is increased until a minimum is reached. While sputtering chromia on the other hand, the target voltage is decreasing first, and then after reaching a minimum value increasing, as the oxygen partial pressure is increased. If voltage control is utilized for this material, a positive and a negative controller have to be utilized for the individual slope regions of the target voltage - oxygen partial pressure characteristic.

I.4.4.6 Reactive Gas Partial Pressure Control

Sproul and Thomashek^{51,52} introduced the partial pressure control of the reactive gas in 1984. The reactive gas partial pressure is measured by a mass spectrometer, and the reactive gas flow is adjusted to keep a constant reactive gas partial pressure. The ratio of the sputtered flux and the reactive gas partial pressure are constant, hence the films are homogenous.

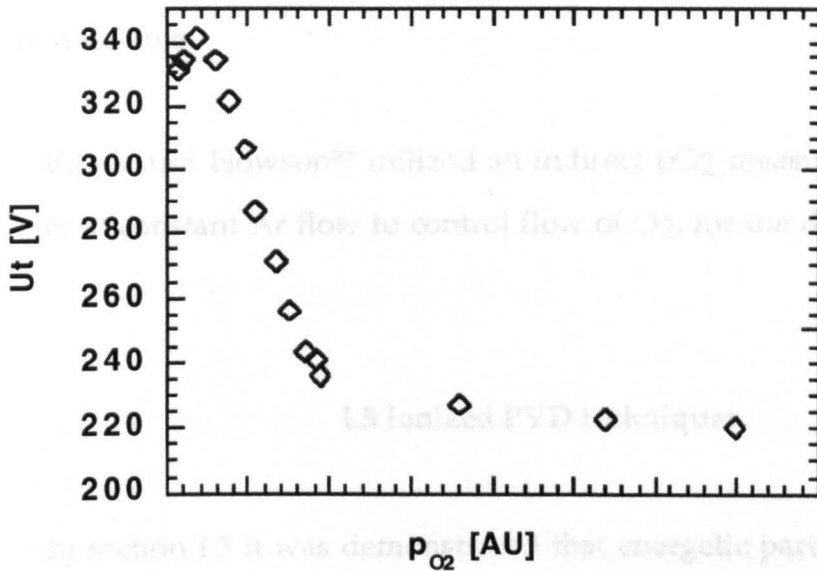


Figure I.4.7a: Alumina target voltage versus oxygen partial pressure

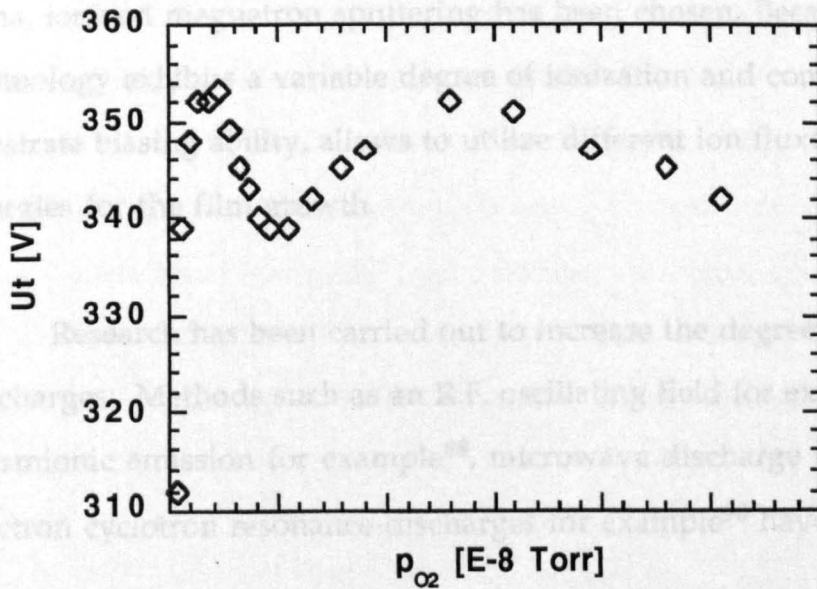


Figure I.4.7b: Chromia target voltage versus oxygen partial pressure

Very high rate deposition of the nitrides and carbides of Ti, Nb and Zr has been demonstrated^{44,51,60,81,82}. The obvious drawback of utilizing a differentially pumped mass spectrometer is, that sampling has to take place in a remote area.

Ridge and Howson⁵⁹ utilized an indirect pO_2 measurement via total pressure at constant Ar flow to control flow of O_2 , for the deposition of ITO.

I.5 Ionized PVD techniques

In section I.3 it was demonstrated that energetic particle bombardment can influence the coating micro structure and properties in a desirable way. While the energy of neutrals is more difficult to control and to measure, the control of energetic ions is a much easier task. To study the influence of energetic particle bombardment on the structure and properties of alumina films, ionized magnetron sputtering has been chosen. Because this deposition technology exhibits a variable degree of ionization and combined with a substrate biasing ability, allows to utilize different ion fluxes and different ion energies for the film growth.

Research has been carried out to increase the degree of ionization in PVD discharges: Methods such as an R.F. oscillating field for example⁸³⁻⁸⁷, thermionic emission for example⁸⁸, microwave discharge for example⁸⁹, and electron cyclotron resonance discharges for example⁹⁰ have been identified.

1969 Beucherie et al⁸³ researched a R.F. inductive plasma sputtering of metals. The films were found to be dense and well adhered.

In 1974 Murayama deposited Au films with significantly improved properties (in terms of pinholes and defects) compared to films produced by D.C. ion plating⁸⁴. Apparently the ions created in the R.F. oscillating field had a positive effect on the film formation of the Au films.

Murayama went on to study the properties of the R.F. reactive ion plated In_2O_3 , TiN and TaN⁸⁵. He found that oxidation and nitriding was enhanced by the excitation of the R.F. oscillating field.

Researchers at IBM studied highly ionized aluminum argon^{86,87} and copper argon discharges^{90,91} for metallization of semiconductor structures, with the objective to fill high aspect ratio trenches (with the metal film). They reported metal ionized flux ratios on the order of 85%^{86,87} to 100%⁹⁰ in high density inductively coupled plasmas. The ionized metal flux is accelerated across the sheath of the electrically biased substrate. The ion energy is a function of the substrate bias potential. Rossnagel and Hopwood⁸⁷ measured the aluminum ion fraction in a high density inductively coupled plasma, by using an energy analyzer and optical emission spectroscopy.

The process parameters with a major influence on the ionized metal fraction were identified as the total pressure (see Figure I.5.1a) and the power supplied to the R.F. coil (see Figure I.5.1b). Depending on the total pressure and the power supplied to the R.F. coil, relative ionization ratios of up to 85% for Al in Ar could be reached.

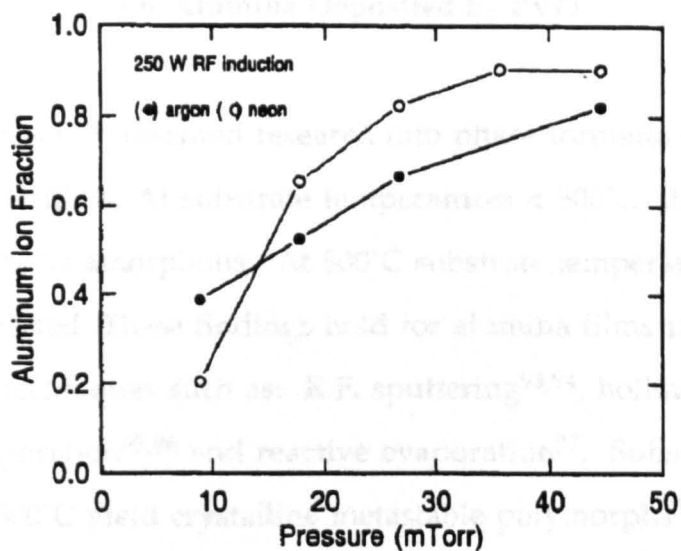


Figure I.5.1a: Relative ionization level of the sputtered Al as a function of the chamber pressure for Ar and Ne working gases, taken from ⁸⁷

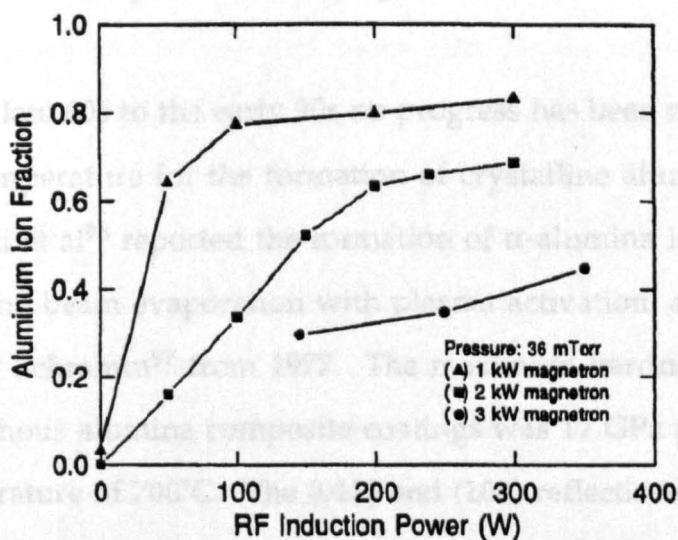


Figure I.5.1b: Relative ionization level of the sputtered Al as a function of the R.F. coil power at different source power settings, taken from ⁸⁷

I.6 Alumina Deposited by PVD

In 1966 Frieser⁹² presented research into phase formation of D.C. sputter deposited alumina films. At substrate temperatures $< 500^{\circ}\text{C}$, the structure was generally found to be amorphous. At 500°C substrate temperature cubic γ -alumina was reported. These findings hold for alumina films produced by a number of PVD techniques such as: R.F. sputtering^{93,94}, hollow cathode R.F. sputtering⁶, evaporation^{95,96} and reactive evaporation⁹⁷. Substrate temperatures $> 500^{\circ}\text{C}$ yield crystalline metastable polymorphs⁹⁵. Sputtered films annealed at 1200°C appeared to yield α -alumina⁶. γ -alumina was reported by Bunshah and Schramm⁹⁷ at 700°C to 800°C and α -alumina at 1100°C to 1200°C substrate temperature by reactive evaporation. Movchan and Demchishin claimed in a private communication as reported in⁹⁷ that the films produced by electron beam evaporation²⁴ had the crystal structure of α -alumina at substrate temperatures ranging from 450°C to 900°C .

From the late 60s to the early 90s no progress has been made on lowering the substrate temperature for the formation of crystalline alumina polymorphs. In 1995 Zywitzki et al⁹⁸ reported the formation of α -alumina in an amorphous matrix by electron beam evaporation with plasma activation, adapting the work of Bunshah and Schramm⁹⁷ from 1977. The maximum hardness of these α -alumina/amorphous alumina composite coatings was 17 GPa produced at a substrate temperature of 700°C . The (012) and (104) reflections of α -alumina could be identified using X-ray diffraction. Selected area diffraction (SAD) gave a grain size in the range of 3 to 5 nm of the alumina crystallites. In the paper the plasma activation is not described. In 1996 the same group⁹⁹ deposited α -alumina by pulsed D.C. magnetron sputtering at a substrate temperature of 760°C . The substrate was floating and the total pressure was 0.75 mTorr (0.1 Pa).

This suggests a close to collisionless discharge. The primary influence on the structure and properties of the growing film is the energy of the neutrals flux impinging on the growing film. The neutral energy distribution is a strong function of the target power. In a later work Zywitzki et al ⁹⁹ showed a correlation between the magnetron power and the formation temperature of α -alumina. The higher the power, and therefore the higher the average neutral energy, the lower the α -alumina phase formation temperature. The driving force of the process is therefore high energetic neutrals.

Also in 1996 Helmersson, Ivanov and Macak¹⁰⁰ reported α -alumina growth at substrate temperatures of 850°C, by magnetically enhanced D.C. magnetron sputtering, utilizing large fluxes of low energy argon ions.

The work of Frieser⁹², Dragoo ⁹⁵and Diamond as well as Thornton⁶ showed that the substrate temperature is very influential on the formation of the crystal structure of the growing alumina film. In the following section physical properties of alumina films are discussed, for the different alumina polymorphs.

Bulk α -alumina is 22 GPa hard and has an elastic modulus of 435 GPa parallel to the c axis². The elastic modulus and hardness of CVD κ and α -alumina was recently investigated by Jaemeting et al ¹⁰¹. κ -alumina was found to be slightly harder than α -alumina, and α -alumina was slightly stiffer than κ -alumina. Zywitzki reported hardness values of 22 GPa but no elastic modulus for his magnetron sputtered films at 750°C⁹⁹. The hardness of amorphous alumina is reported to be in the range of 8-12 GPa¹⁰²⁻¹⁰⁴. The elastic modulus ranges from 80-100 GPa¹⁰²⁻¹⁰⁴.

As already mentioned, alumina hard coatings are used in cutting tool applications. Typically these coatings are deposited at substrate temperatures of 1000°C by chemical vapor deposition (CVD)⁴ onto sintered substrates such as cemented carbide. Cutting involves the gross deformation or micro fracture of the workpiece and leads consequently to high contact stresses (5-10000 atm¹⁰⁵) and sliding wear at the tool workpiece interface. During high speed cutting of steel, temperatures of ~1200°C⁹ can be reached. It is well known that at high cutting temperatures tool wear is dominated by chemical effects, based on the solubility of the tool material and the workpiece material, see reference¹⁰⁵ and references therein. Kramer and Judd presented a quantitative model, based on abrasive wear and chemical dissolution wear to evaluate potential tool coatings in 1985¹⁰⁵. The best material in chemical wear was α -alumina, and in abrasive wear only SiC, WC and Si₃N₄ were more resistant to wear.

The thermal stability of κ -alumina was studied by Vurionen and Karlsson⁹. The annealing experiments conducted in a temperature range of 1020°C to 1100°C, in an Ar ambient represent a realistic temperature range for cutting tool applications^{9,105}. CVD κ -alumina was found to be stable at temperatures of up to 1030°C, however at temperatures of 1090°C rapid phase transformation from κ -> α -alumina could be observed.

Another important property of α -alumina is the low thermal conductivity with 0.4 W/(cm k) and 0.1 W/(cm k) at 25°C and 1000°C² respectively, helps to protect the tool substrate material, and although materials with even lower thermal conductivity (the thermal conductivity for cubic zirconia is 2 W/(m k)²) are used today as thermal barrier materials in aero engines, alumina could find application as part of advanced thermal barrier coatings designs, based on increased phonon-scattering by the interfaces of

thousands of individual layers, and or by introducing amorphous layers which reduces the thermal conductivity. Furthermore, alumina is commonly used in aero engine multilayered coating designs as an oxidation barrier¹⁰⁶.

Alumina is non-thrombogenic² as well as non reactive with body fluids and therefore shows potential for coatings for implants.

II. Methods of Research

The first two sections of this chapter describe the deposition equipment and the deposition procedure used, the sections following these describe methods for the analysis of the films produced.

Two different deposition systems were used in this work for different aspects of the deposition of alumina. An opposed cathode closed-field unbalanced magnetron sputtering system with a volume of approximately 300 liter, and a 70 liter unbalanced magnetron sputtering system, with optional ionized sputtering capability.

During the work on this thesis a novel alumina high rate deposition process was developed by the present author. The process was also successfully applied to the high rate deposition of zirconia by the present author¹⁰⁷. The work was carried out in an industrial size deposition system.

The alumina phase formation studies, and alumina-alloy studies were carried out in a smaller research system, with an adjustable degree of ionization, substrate heating and substrate biasing. The system was re-designed during the course of this study to allow for more effective ionization of the sputtered flux, which is crucial if low temperature growth of crystalline alumina is attempted.

II.1 Conventional Magnetron Sputtering

The opposed cathode closed-field unbalanced magnetron sputtering system used in these experiments is shown in Figure II.1.1 and has been described in detail elsewhere¹⁰⁸. The chamber has a volume of ~300 l, and is pumped by two sets of pumps: One set is a 2400 l/sec diffusion pump that is backed by a 38 l/sec mechanical pump; and a second set is a 1500 l/sec turbomolecular pump backed by a roots blower and mechanical pump with a pumping speed of 68 l/sec. The sputter sources were Materials Research Corporation (MRC) Mu Inset cathode (12.7cmx38.1cm), and they are powered by a D.C. power supply pulsed at 50 kHz (AE MDX 10kW + AE SPARC-LE 50kHz) running in a constant power mode at 3 kW. The sputtering targets were Al (purity = 99.99%). Sputtering was carried out in a mixed Ar (99.999%) and O₂ (99.999%) atmosphere at a total pressure of 5 mTorr (0.67 Pa), which was maintained by a capacitance manometer linked to a mass flow controller. Optical microscope glass slides were used as substrates in single fold rotation. Prior to deposition they were ultrasonically cleaned in acetone and ethanol and then dried with carbon dioxide. The target to substrate distance was 7 cm. The substrate was R.F. biased (13.56 MHz) with at a power of 1 kW during ion etching in 5 mTorr Ar prior to deposition as well as during reactive sputtering. The etching time was 10 minutes. The reactive gas was introduced into the chamber in a controlled way, to avoid target poisoning, and subsequent reduction of the deposition rate. The development of a novel process control technology, based on a combination of partial pressure control^{51,52} of the reactive gas and the utilization of medium frequency pulsed D.C. power⁵⁴ combination is discussed in detail in Chapter 3.

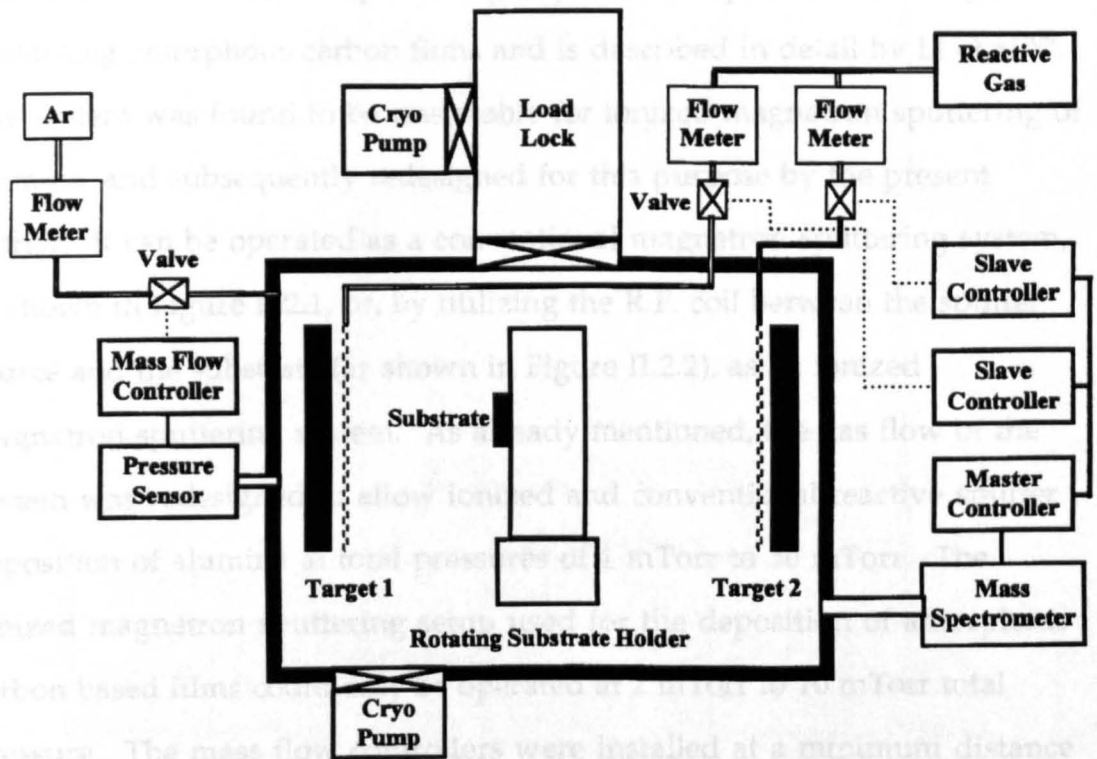


Figure II.1.1: Schematic of the opposed cathode closed-field unbalanced magnetron sputtering system

II.2 Ionized magnetron sputtering system

A research scale ionized magnetron sputtering system after Rosnagel and Hopwood⁸⁷ was set up in our group for the deposition of nitrogen containing amorphous carbon films and is described in detail by Li et al¹⁰⁹. The system was found to be unsuitable for ionized magnetron sputtering of alumina, and subsequently redesigned for this purpose by the present author. It can be operated as a conventional magnetron sputtering system, as shown in Figure II.2.1, or, by utilizing the R.F. coil between the sputter source and the substrate (as shown in Figure II.2.2), as an ionized magnetron sputtering system. As already mentioned, the gas flow of the system was redesigned to allow ionized and conventional reactive sputter deposition of alumina at total pressures of 1 mTorr to 30 mTorr. The ionized magnetron sputtering setup used for the deposition of amorphous carbon based films could only be operated at 2 mTorr to 10 mTorr total pressure. The mass flow controllers were installed at a minimum distance from the chamber to optimize the response time of the gas flow.

As discussed in section I.5, in ionized magnetron sputtering the degree of ionization is a strong function of the total pressure⁸⁷. To utilize the benefits of ionized magnetron sputtering, the total pressure has to be around 30 mTorr, otherwise the degree of ionization can not be significantly increased. To achieve this, the pumping speed was increased and a throttle valve was added to allow for depositions at total pressures from 1 to 30 mTorr.

The base pressure of the 70 l vacuum system, pumped by a two 92 l/sec turbomolecular pump was 7×10^{-7} Torr. Aluminum (purity=99.9%)

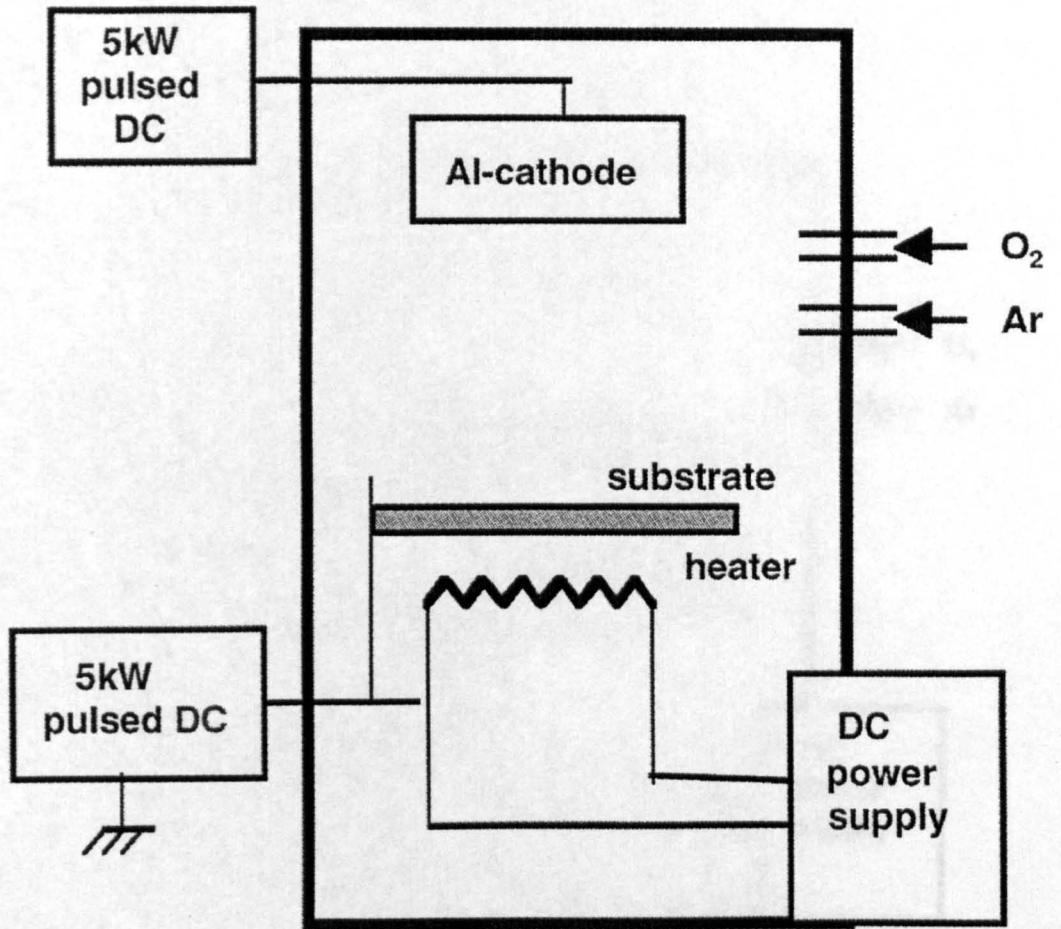


Figure II.2.1: Conventional Magnetron Sputtering System

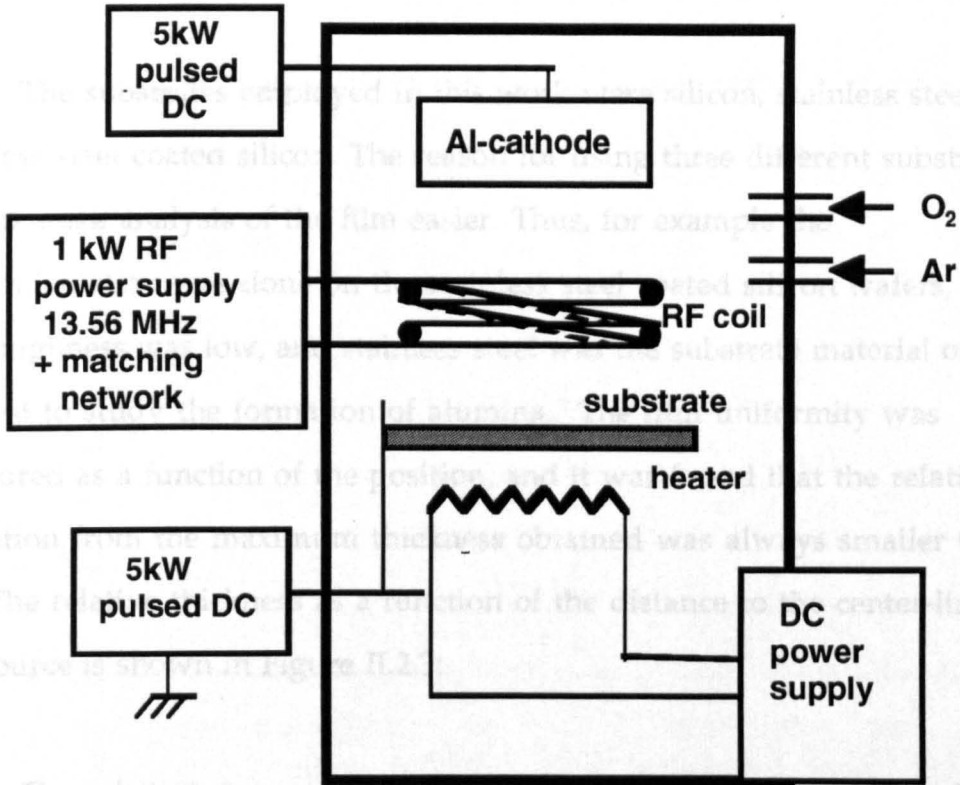


Figure II.2.2: Schematic drawing of the ionized magnetron sputtering system

was sputtered at a total pressure of 1 mTorr to 30 mTorr in an argon/oxygen atmosphere. The power density at the magnetron was kept constant at 10 W/cm². The source as well as the substrate were powered by 5 kW ENI Reactive Plasma Generators in a master-slave setup. The pulse frequency was 150 kHz for most of the experiments.

The substrates employed in this work were silicon, stainless steel and stainless steel coated silicon. The reason for using three different substrates was to make analysis of the film easier. Thus, for example the nanoindentation was done on the stainless steel coated silicon wafers, since the roughness was low, and stainless steel was the substrate material of interest to study the formation of alumina. The film uniformity was measured as a function of the position, and it was found that the relative deviation from the maximum thickness obtained was always smaller than 9%. The relative thickness as a function of the distance to the center-line of the source is shown in Figure II.2.3:

The substrate temperature during deposition was measured with a K type thermocouple, which touched the substrate surface. The probe potential was equal to the potential of the substrate, so that the temperature could be continuously monitored during deposition.

No partial pressure sensor was needed to achieve high rate deposition because of the small source size and the high pumping speed. The target voltage versus O₂ flow rate was monitored (see Figure II.2.4), and a flow rate of 2 sccm was chosen for these experiments. This flow rate resulted in an oxygen partial pressure of 4×10^{-4} Torr, measured against an ion gauge. Utilizing results discussed in chapter 3, the correlation between

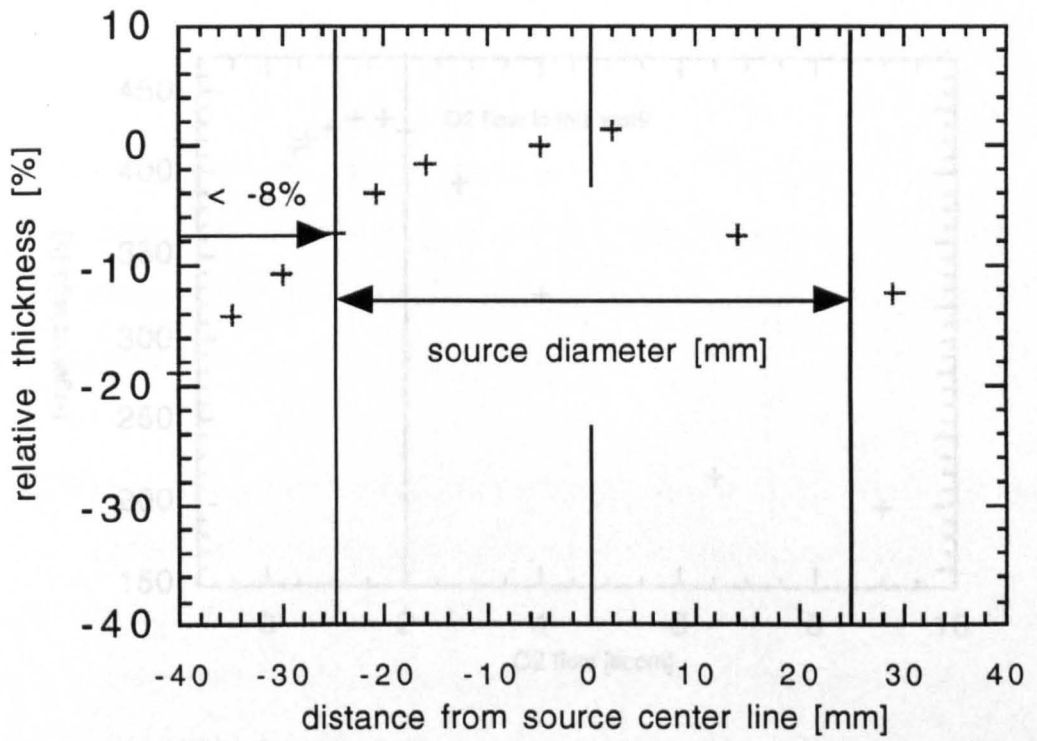


Figure II.2.3: Relative films thickness versus the distance to the centerline of the magnetron.

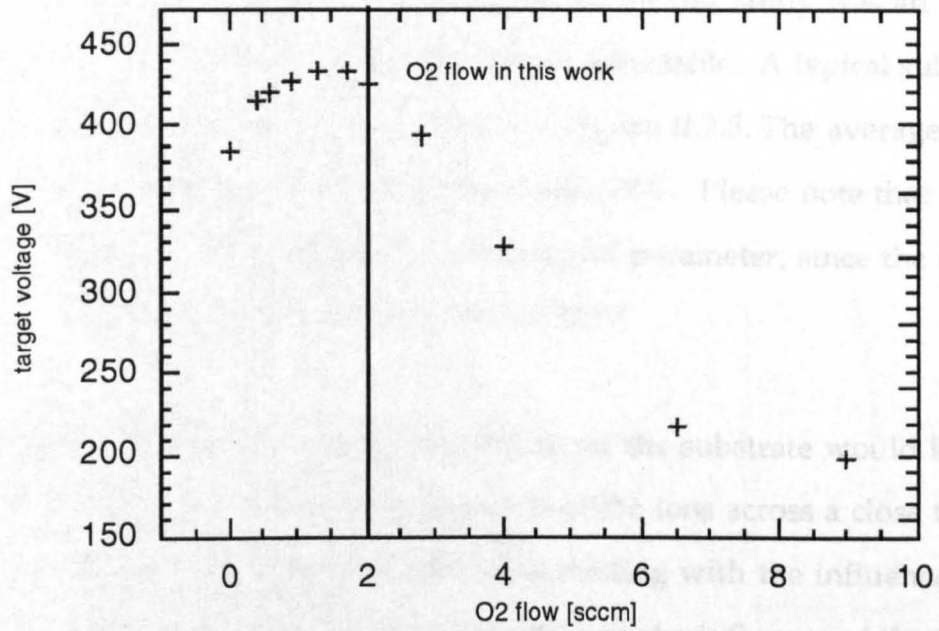


Figure II.2.4: Target voltage versus O₂ flow characteristic.

reactive gas partial pressure, reactive gas flow and target voltage the high rate deposition region was estimated from the voltage flow characteristic shown in Figure II.2.4.

In section I.4.3 it was discussed that if pulsed D.C. power is utilized, the target voltage, the target current and hence the target power are a function of time. The power supply employed for this study was an ENI RPG 50¹¹⁰. The frequency and duty cycle are adjustable. A typical substrate bias voltage versus time trace is shown in Figure II.2.5. The average substrate bias voltage for this experiment was -70V. Please note that the average voltage is not necessarily a meaningful parameter, since the peak to peak voltage in this case is on the order of 520V.

The maximum ion energy impinging on the substrate would be on the order of -360 eV, assuming acceleration of the ions across a close to collisionless substrate sheath. Rather than dealing with the influence of the substrate bias potential, it is necessary to discuss the influence of the ion energy distribution, as well as the ion flux distribution.

Films were grown in four different discharges: (1) conventional magnetron sputtering onto floating substrates at different total pressures at $T_S < 100^\circ\text{C}$; (2) conventional magnetron sputtering with and without substrate bias at $T_S = 70^\circ\text{C}$ to 500°C and 30 mTorr total pressure (results are discussed in chapter IV); (3) Ionized magnetron sputtering, with and without (4) substrate biasing at $T_S = 280^\circ\text{C}$ to 500°C and 30 mTorr total pressure (results are discussed in chapter V).

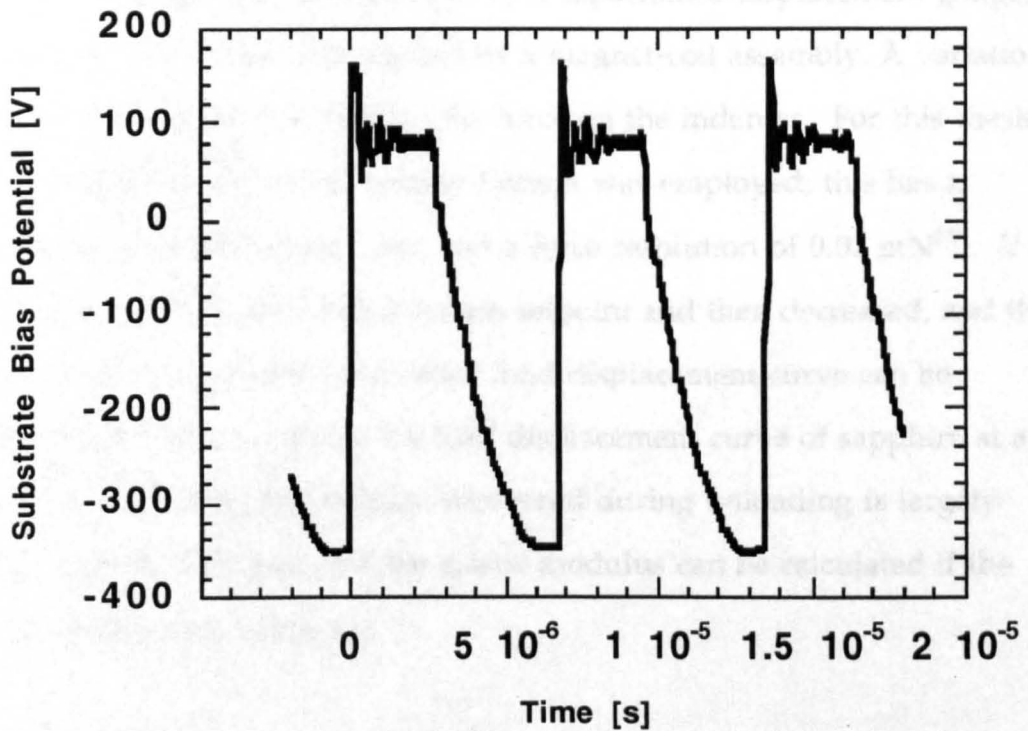


Figure II.2.5: Substrate bias voltage versus time plot for a typical samples produced by ionized magnetron sputtering

II.3 Nanoindentation

Nanoindentation instruments or depth sensing indentation instruments provide a means of studying the elastic and plastic properties of thin films. A so-called Berkovich indenter was used (with the same area to depth ratio as a traditional Vickers indenter) in all experiments. The exact position of the indenter is measured by a capacitance displacement gauge, the load on the indenter is applied by a magnet-coil assembly. A variation of the current to the coil changes the force on the indenter. For this thesis a UMIS 2000 Ultra Micro Indentation System was employed; this has a displacement resolution of 1 nm and a force resolution of 0.01 mN¹¹¹. If the force is stepwise increased to a certain setpoint and then decreased, and the displacement is recorded, a so-called load displacement curve can be obtained. Figure II.3.1 shows the load displacement curve of sapphire at a load of 4 mN. The displacement recovered during unloading is largely elastic, and the hardness and the elastic modulus can be calculated if the elastic contact area is known.

II.3.1 Hardness Measurement

Hardness can be defined as the average pressure under the indenter. The hardness H can be calculated by dividing the applied maximum load P_{\max} by the projected area A of contact between the indenter tip and the sample.

$$H = P_{\max} A^{-1} \quad (\text{II.1})$$

The total penetration h_{total} is calculated without the use of the slope of the unloading curve. The total penetration h_{total} is the sum of the elastic penetration h_{e} and the plastic penetration h_{p} . However, the plastic penetration h_{p} is not recovered during unloading, and the indenter tip area in contact with the sample is constant. For the calculation of h_{e} , the plastic contribution is subtracted

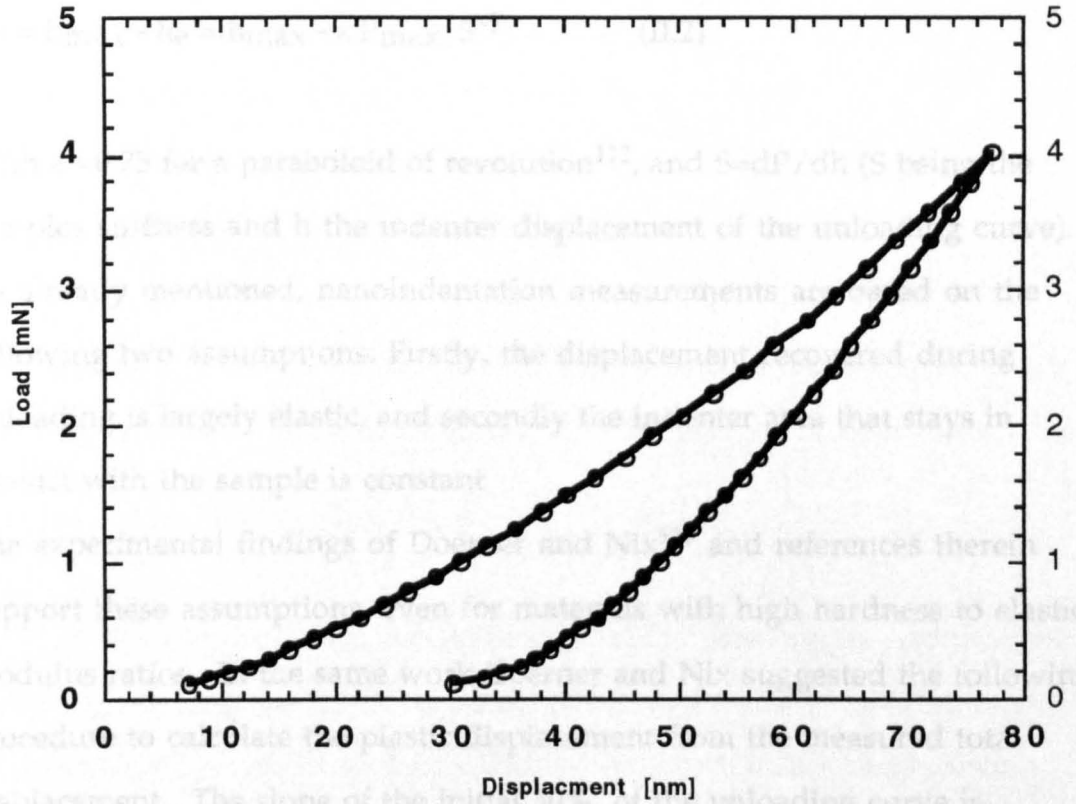


Figure II.3.1: Load displacement curve of sapphire at a load of 4 mN.

In Nanoindentation the contact area A is measured without imaging and is a function of the plastic penetration. The total penetration h_{\max} includes both, plastic h_p and elastic h_e contributions. However, the displacement recovered during unloading is largely elastic, and the indenter area that stays in contact with the sample is constant. For the calculation of the hardness, the elastic contribution is subtracted

$$h_p = h_{\max} - h_e = h_{\max} - \epsilon P_{\max} S^{-1} \quad (\text{II.2})$$

With $\epsilon = 0.75$ for a paraboloid of revolution¹¹², and $S = dP/dh$ (S being the samples stiffness and h the indenter displacement of the unloading curve). As already mentioned, nanoindentation measurements are based on the following two assumptions: Firstly, the displacement recovered during unloading is largely elastic, and secondly the indenter area that stays in contact with the sample is constant

The experimental findings of Doerner and Nix¹¹³ and references therein support these assumptions, even for materials with high hardness to elastic modulus ratios. In the same work Doerner and Nix suggested the following procedure to calculate the plastic displacement from the measured total displacement. The slope of the initial 30% of the unloading curve is mathematically described and fitted, and the intersect of the fitting function with the displacement axis calculated. The intersect with the displacement axis represents purely plastic deformation h_c .

II.3.2 Tip Correction

All the above equations assume an perfectly sharp tip. Since the indenter utilized in a measurement has a radius to it, a correction needs to be employed, the so-called tip correction. This is usually done by measuring a standard bulk material with known plastic and elastic properties.

Throughout this work the standards used to estimate the tip correction function were fused silica and sapphire. The elastic moduli of both materials are known, see reference¹¹⁴ and¹¹⁵ respectively.

The sample stiffness is given by:

$$S = dP/dh = 2 \pi^{-0.5} E_r A^{0.5} \quad (\text{II.3})$$

With E_r being the reduced elastic modulus. E_r is related to the elastic modulus of the sample E_s and the indenter E_i through the relationship:

$$E_r^{-1} = (1-\nu_s^2) E_s^{-1} + (1-\nu_i^2) E_i^{-1} + F \quad (\text{II.4})$$

With ν_s and ν_i being the Poisson's ratio for the sample and indenter, and F representing the elastic response of the load frame¹¹². The equations are solved for h_p , and by using the known elastic modulus and Poisson's ratio of the standard materials, a corrected h_p value, so called h_{pc} can be calculated, representing the plastic depth corrected for the deviation of the real tip from a perfect tip. The correlation of h_{pc} and h_p is called the tip correction function.

$$h_{pc} = F(h_p)$$

In Figure II.3.2 the h_{pc} is plotted vs h_p , and a power law fit is shown.

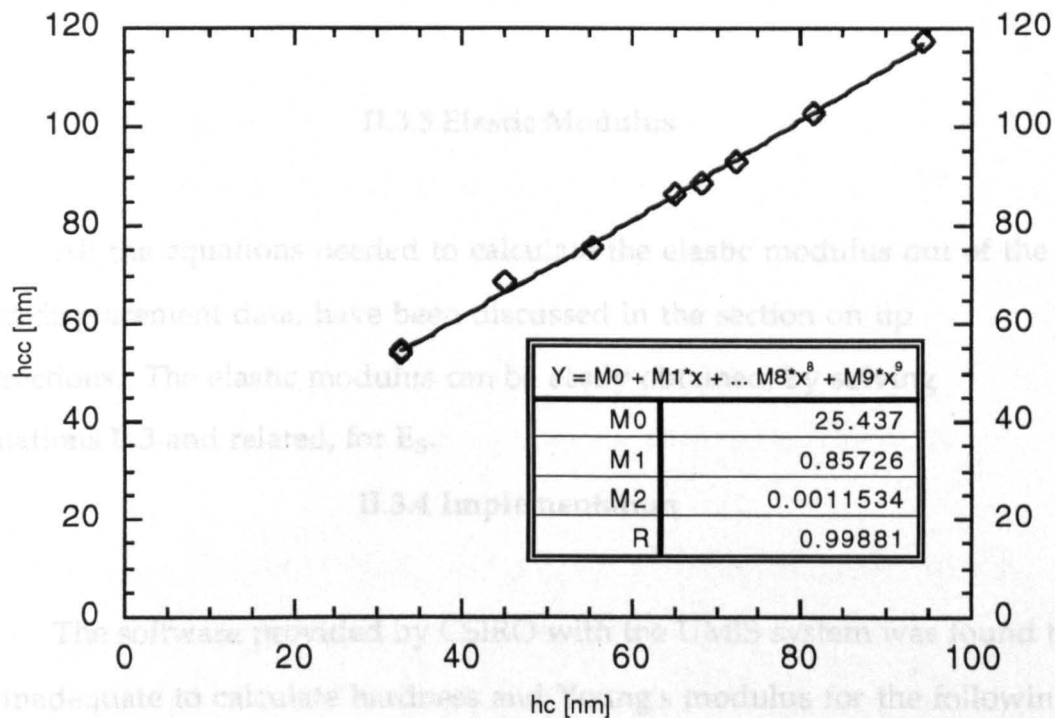


Figure II.3.2: The corrected plastic penetration depth (h_{pc}) versus the plastic penetration depth (h_p) and the

Now the corrected contact area for a Berkovich indenter can be calculated with:

$$A = 24.5 h_{pc}^2$$

From there, corrected hardness values can be obtained.

II.3.3 Elastic Modulus

All the equations needed to calculate the elastic modulus out of the load displacement data, have been discussed in the section on tip corrections. The elastic modulus can be easily obtained, by solving Equations II.3 and related, for E_s .

II.3.4 Implementation

The software provided by CSIRO with the UMIS system was found to be inadequate to calculate hardness and Young's modulus for the following reasons:

- no indenter shape correction was taken into account, or in other words the software is based on a flat punch geometry.
- the fitting algorithms for both the initial penetration estimation, and the tip correction functions were found to be crude.

Therefore a mathcad module was written by the present author, which is based on the work of Oliver and Pharr¹¹² (as described in sections

II.3.1 to II.3.3) and can be found in Appendix 'Nanoindentation'. This program was used to calculate both the tip correction function as well as the elastic and plastic properties out of the load-displacement raw data provided by the UMIS 2000 system. The program is used routinely by my coworkers at BIRL.

II.4 X-Ray Diffraction (XRD)

Phase analysis was carried out using a Rigaku powder diffractometer with Cu K α radiation in the standard Bragg-Brentano geometry. The X-ray generator settings were 40 kV and 20 mA. The step-size was 0.05°, and scans were acquired from 20-60 2 θ .

II.5 Field Emission Scanning Electron Microscopy (FESEM)

A Hitachi S-4500 FESEM was used for the morphological analysis. Due to the insulating character of the samples investigated, the acceleration voltage was set to 3 keV. No sample preparation was necessary.

II.6 Scanning Auger Microprobe (SAM)

A Physical Electronics scanning Auger microprobe with depth profiling capability was used to investigate the chemical composition of the coatings. The beam voltage was 3 keV, the filament current 1.4 A, and the emission current was 0.5 mA, which minimized the charging and subsequent peak shape deformation. Ion etching was performed until no change in the metal to oxygen ratio was observed. Sapphire bulk material was used as a standard for the chemical composition evaluation.

II.7 X-Ray Photoelectron Spectroscopy (XPS)

Film chemical composition and binding energy analysis were performed using X-ray photoelectron spectroscopy (XPS). A Surface Science Instruments M-Probe instrument with monochromatic Al K α X-rays was calibrated to give a full width at half maximum (FWHM) of 0.77 eV for the Au 4f $_{7/2}$ peak at 25 eV pass energy and 400x1000 mm spot.

The binding energy scale was adjusted using copper standards with the Cu 3s and Cu 2p $_{3/2}$ peaks at 122.39 eV and 932.47 eV, respectively. A low fluence electron gun was used to remove possible positive surface charging. The binding energy scale was then verified using C 1s peaks from carbon present on the sample surface. A Voight function was used to fit the peaks. Sapphire and Al-metal disks were used as references.

II.7 Spectrophotometer;

The optical transmission of the coatings was obtained from a Cary 2400 spectrophotometer, in the wavelength range of 350 nm to 700 nm.

III. High Rate Deposition of Alumina

In this chapter the development of a novel very high rate deposition process is presented. Experiments were carried out in a industrial size vacuum chamber with a chamber volume of ~300 liters, at substrate temperatures $< 250^{\circ}\text{C}$. The influence of the O_2 partial pressure on the deposition rate, optical and mechanical properties is discussed. Utilizing both, pulsed D.C. power to sputter $\text{Al}+\text{AlO}_x$ off the target surface and partial pressure control of the reactive gas to maintain a certain partial pressure value, the deposition of transparent, fully dense, and stiff alumina coatings at a relative deposition rate of up to 76% of the metal rate is described.

III.1 Deposition Rate

Amorphous alumina coatings have been produced by a variety of PVD techniques, for example by D.C. reactive sputtering⁴⁸, dual pulsed D.C. magnetron sputtering¹¹⁶, D.C. s-gun sputtering¹¹⁷ and R.F. sputtering¹⁰³. These coatings may be used on magnetic read-write heads³ as diffusion barrier coatings¹¹⁸, corrosion resistant coatings¹¹⁹, in optical applications¹²⁰, and for food packaging¹⁰². In any industrial application, a high deposition rate is of great importance. Aluminum can be sputtered at rates which are a factor 10 higher than alumina. Hence the possibility to achieve high deposition rates while sputtering off a metallic target.

Several techniques for rate enhancement for the deposition of alumina coatings by magnetron sputtering have been investigated in the past: separation of the reactive gas from the target by the use of baffles^{73,74}, or hollow cathode substrate holders⁵³ and dual pulsed D.C. magnetron

sputtering¹¹⁶. The use of baffles resulted in a considerable rate increase compared to R.F. magnetron sputtering, but 60-90% of the sputtered flux was lost due to deposition on the baffles. The hollow cathode substrate holder⁵³ increased the rate significantly, but is difficult to implement for 3 dimensional substrates. Recently, an alumina deposition rate of 60% relative to the metal rate was reported by dual magnetron, pulsed D.C. sputtering¹¹⁶.

Figure III.1 shows the hysteresis curve for AlO_x with partial pressure control of the Oxygen at steady state experimental conditions. The box in Figure III.1 shows the part of the hysteresis curve studied in the experiment, which is shown in more detail in Figure III.2. Films were produced at 0, 0.36, 0.41 and 0.43 mTorr O_2 partial pressure in single fold rotation, resulting in 100%, 92%, 76% and 38% deposition rate, relative to the metal deposition rate. The accuracy of the reactive gas partial pressure control is better than 0.005 mTorr. The deposition rate in a pure Ar discharge is $9.9 \text{ \AA}/\text{sec}$. The rate data for the AlO_x is given in Figure III.2. As expected, increasing the O_2 partial pressure reduces the deposition rate. The films produced at 76% and 38% of the metal rate appeared transparent, whereas the films produced at 92% appeared to be brown. To the best of the author's knowledge at this time, 76% of the metal rate is the highest rate ever obtained by reactive pulsed D.C. magnetron sputtering of transparent AlO_x .

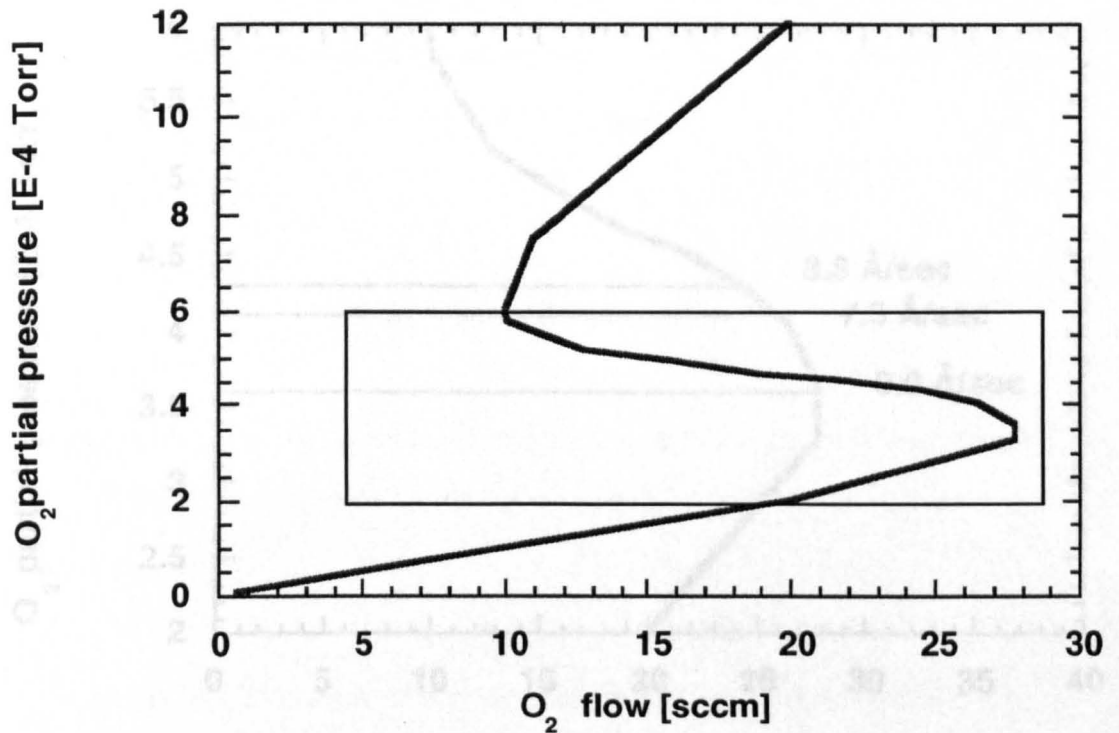


Figure III.1: AlO_x hysteresis curve @ 3kW target power, 1kW R.F. substrate bias power and 5 mTorr total pressure

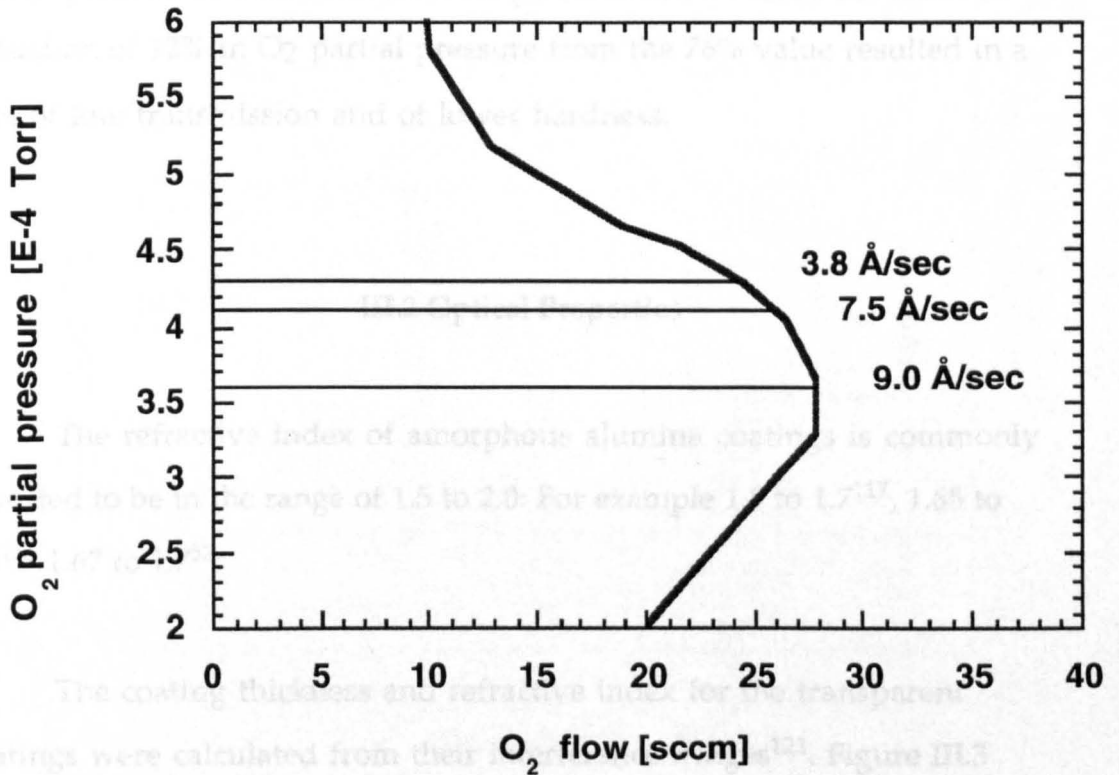


Figure III.2: AlO_x hysteresis curve with deposition rate information @ 3kW target power, 1kW R.F. substrate bias power and 5 mTorr total pressure

These experiments show clearly that this high rate can only be achieved by precisely maintaining a certain O₂ partial pressure value (position on the hysteresis curve). A shift towards higher O₂ partial pressures drastically reduces the deposition rate. An O₂ partial pressure increase of 5% (see Figure III.2) decreased the deposition rate from 76% to 38% of the metal deposition rate. Conversely a shift towards lower O₂ partial pressures resulted in the incorporation of free Al in the film. A reduction of 12% in O₂ partial pressure from the 76% value resulted in a film of low transmission and of lower hardness.

III.2 Optical Properties

The refractive index of amorphous alumina coatings is commonly reported to be in the range of 1.5 to 2.0: For example 1.5 to 1.7¹¹⁷, 1.65 to 2.0¹¹⁶ 1.67 to 1.7⁵³.

The coating thickness and refractive index for the transparent coatings were calculated from their interference fringes¹²¹. Figure III.3 shows the transmission of the coating produced at 76% of the metal rate. Neglecting absorption, the refractive index was calculated to be approximately 1.65 at 550 nm for the transparent films. These values are in the range of values published by other workers¹¹⁶. The calculated coating thickness agrees well with the measurement obtained from a Dektak 3030ST surface profilometer.

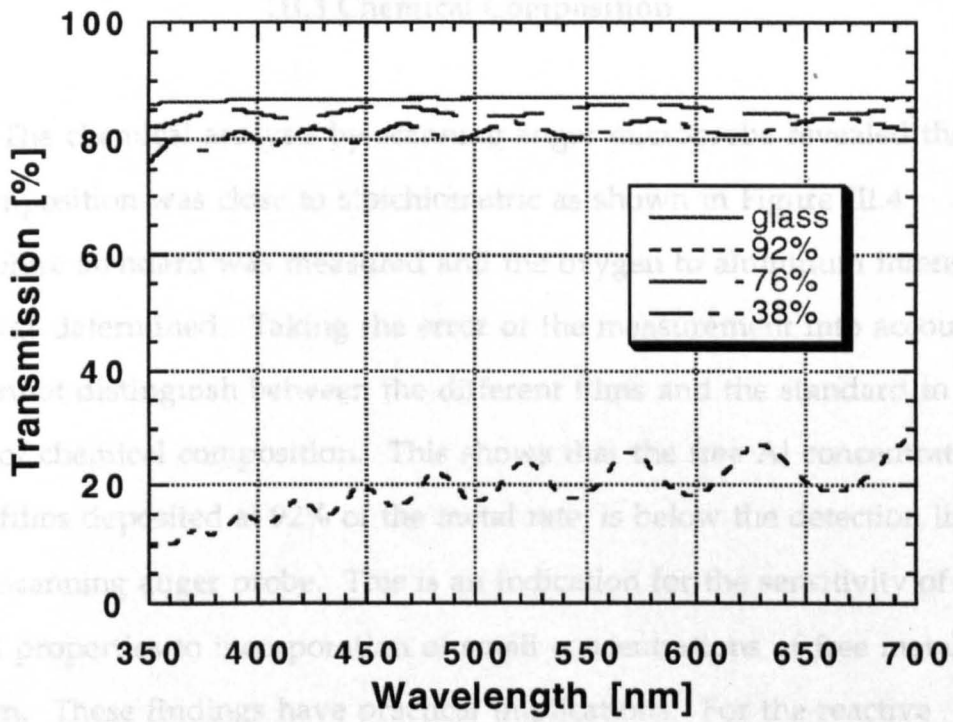


Figure III.3: Transmission versus wavelength for AlO_x coatings produced at various oxygen partial pressures

A shift towards lower O₂ partial pressures resulted in the incorporation of free Al in the film. A reduction of 12% in O₂ partial pressure from the 76% value resulted in a film of low transmission and of lower hardness. Free metal incorporated in a film causes absorption and hence the reduced transmission observed and the gray-brown color of the film.

III.3 Chemical Composition

The chemical analysis by scanning auger microprobe revealed that the composition was close to stoichiometric as shown in Figure III.4. A sapphire standard was measured and the oxygen to aluminum intensity ratio was determined. Taking the error of the measurement into account, one cannot distinguish between the different films and the standard in terms of chemical composition. This shows that the free Al concentration in the films deposited at 92% of the metal rate, is below the detection limit of the scanning auger probe. This is an indication for the sensitivity of the optical properties to incorporation of small concentrations of free metal in the film. These findings have practical implications: For the reactive deposition of oxides without sophisticated process control equipment, this problem can be overcome by operating at large oxygen partial pressures (and 'poison' the target), with the penalty of a ~ factor 10 lower deposition rate. In an industrial situation both good optical properties and high rate deposition is required. This can be achieved with precise control of the oxygen partial pressure, in a way that one position on the oxygen flow versus oxygen partial pressure curve can be maintained. Without suitable control, fluctuations of the oxygen partial pressure will lead to large changes in the deposition rate (as discussed in section III.1) While operating close to

the 'knee' of the hysteresis curve, without suitable control, the incorporation of free metal concentrations smaller than the detection limit of the scanning auger probe in the film will occur. This will cause absorption of the film (as shown in Figure III.3 for the films produced at 92% of the metal rate).

of the film. The low and high deposition rates were approximately 2000 Å/min and 10000 Å/min, respectively. The films deposited at 250°C are in the range of 8 GPa to 11 GPa. The elastic modulus is reported to be in the range of 82 GPa for alumina. The elastic and hardness were evaluated using

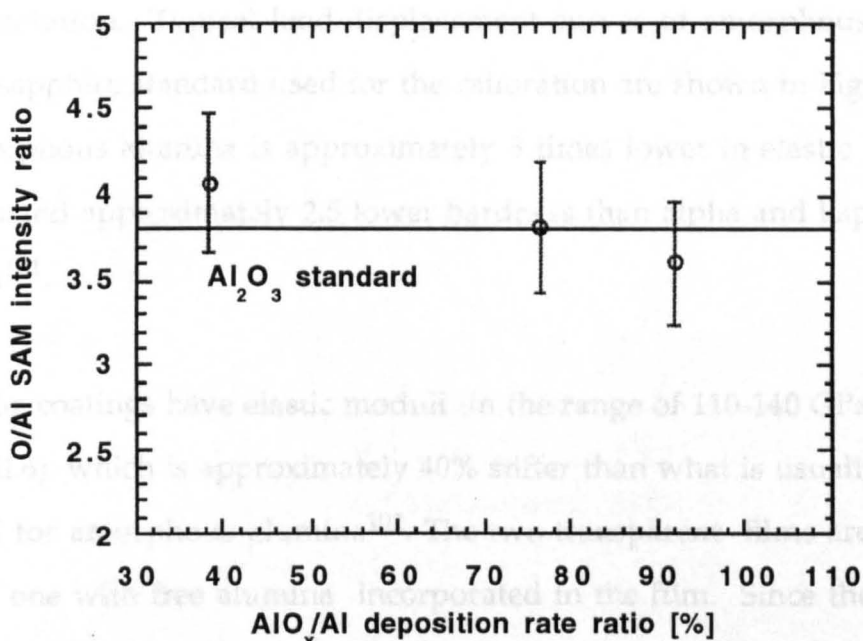


Figure III.4: Scanning Auger Microprobe oxygen to alumina intensity ratio versus deposition rate relative to the metal rate

III.4 Mechanical Properties

In the literature we find hardness values for amorphous alumina coatings at substrate temperatures $< 250^{\circ}\text{C}$ are in the range of 8 GPa to 12 GPa^{53,102,116}. The elastic modulus is reported to be in the range of 82 GPa to 95 GPa¹⁰². Elastic modulus as well as hardness were evaluated using nanoindentation. Typical load-displacement curves of amorphous alumina and the sapphire standard used for the calibration are shown in Figure III.5. The amorphous alumina is approximately 3 times lower in elastic modulus and approximately 2.5 lower hardness than alpha and kappa alumina¹⁰¹.

The coatings have elastic moduli in the range of 110-140 GPa (see Figure III.6), which is approximately 40% stiffer than what is usually reported for amorphous alumina¹⁰². The two transparent films are stiffer than the one with free alumina incorporated in the film. Since the elastic modulus reflects the strength of the chemical bond, further investigations are necessary to resolve the chemical bonding and the structure of these very stiff films. The hardness values (see Figure III.6) are on the high end of what is reported in the literature¹⁰², and the hardness of shows a maximum of 11.1 ± 1.1 GPa for the film deposited at 76% of the metal rate.

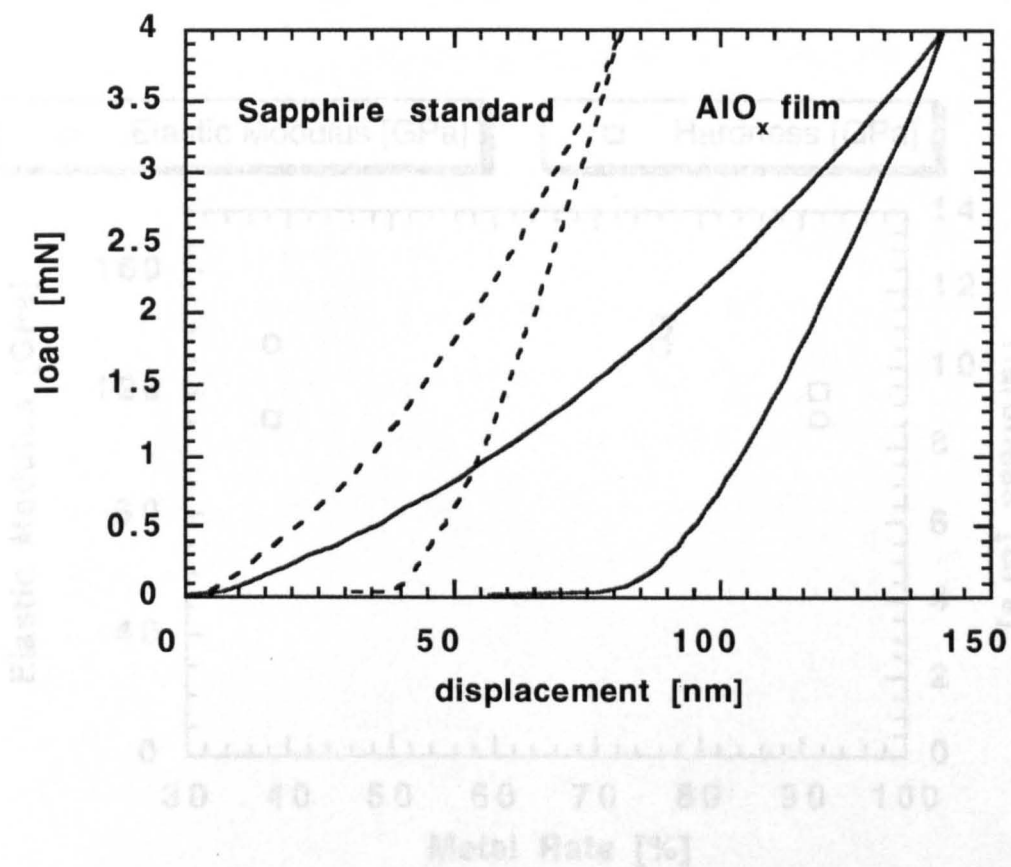


Figure III.5: Load displacement curve of a typical amorphous alumina film and the sapphire standard used for calibration

Figure III.6: Elastic modulus and hardness versus AlO_x/Al deposition rate ratio

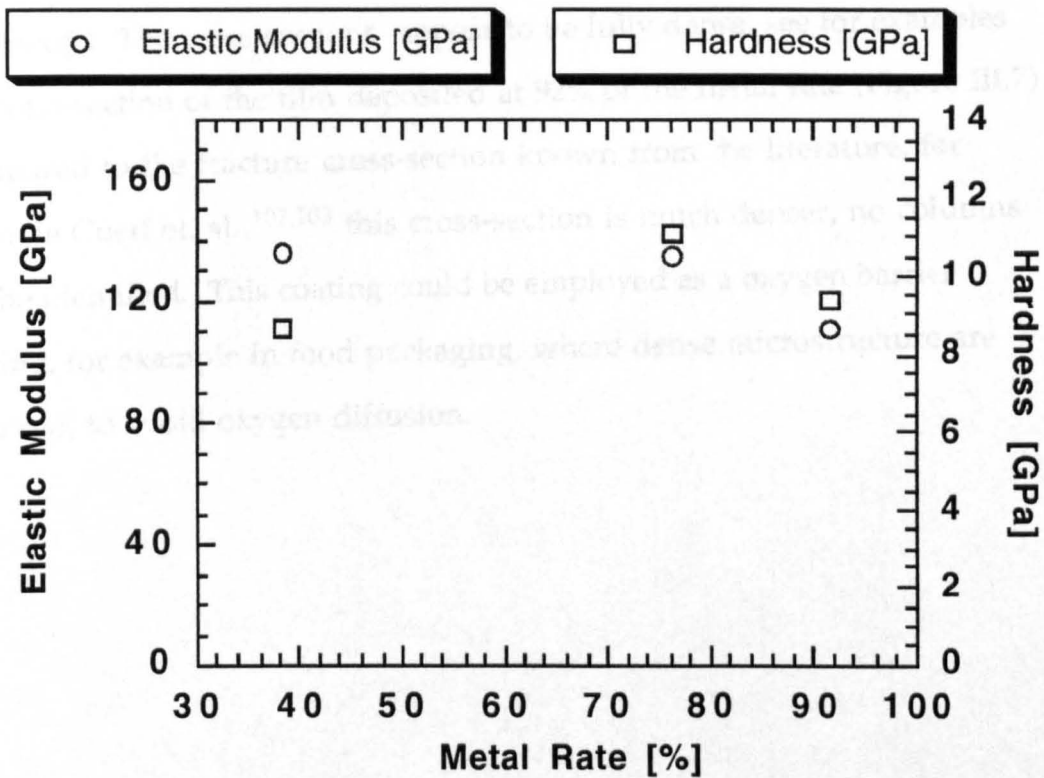
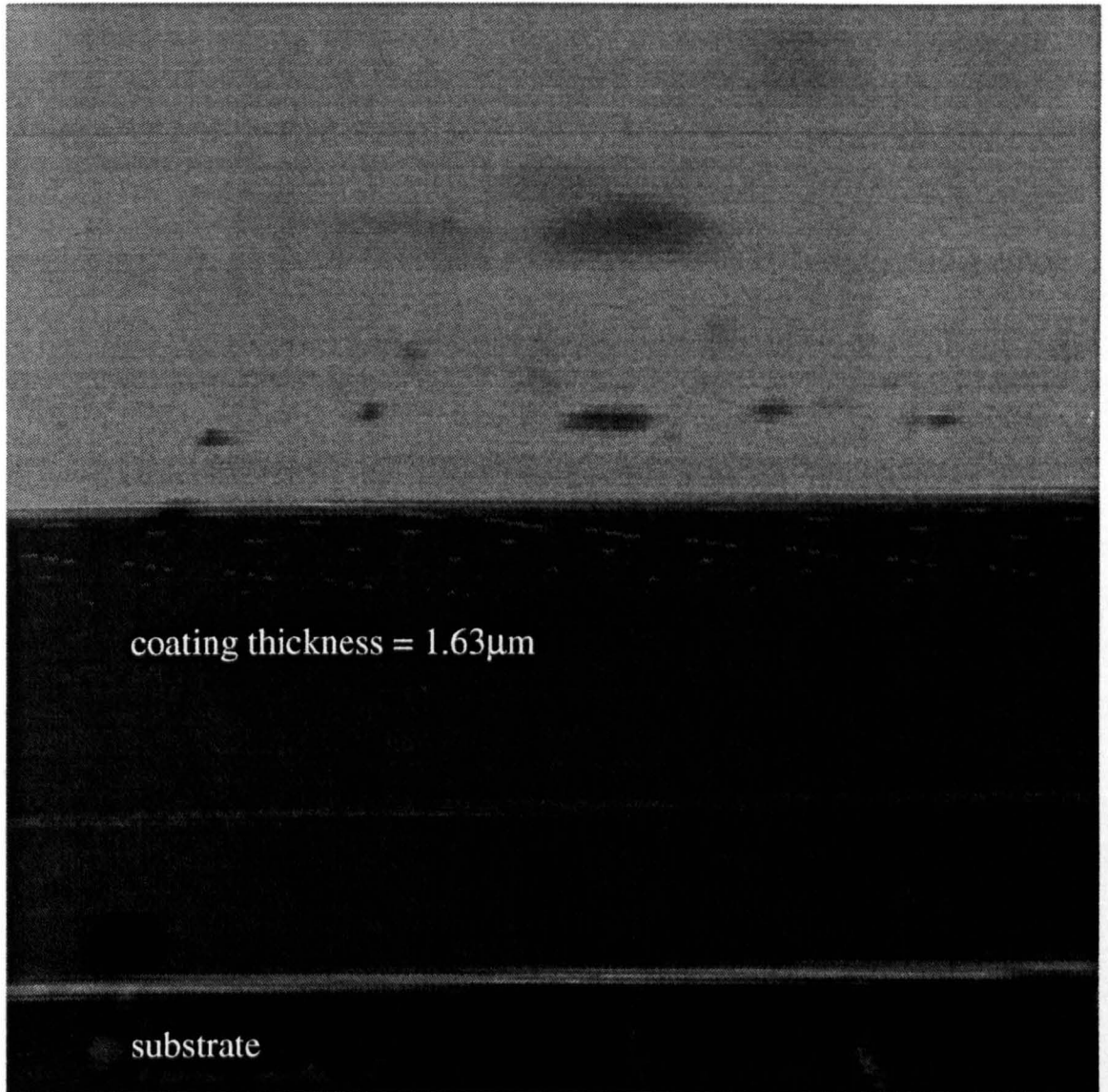


Figure III.6: Elastic modulus and hardness versus AlO_x/Al deposition rate ratio

III.5 Microstructure

X-ray diffraction showed that all films were X-ray amorphous, which is expected, and in good agreement with the literature. The coating morphology was investigated by field emission scanning electron microscopy. The cross-sections appear to be fully dense, see for examples the cross-section of the film deposited at 92% of the metal rate (Figure III.7). Compared to the fracture cross-section known from the literature, for example Cuff et. al. ^{102,103} this cross-section is much denser, no columns can be identified. This coating could be employed as a oxygen barrier coating, for example in food packaging, where dense microstructure are required, to avoid oxygen diffusion.

...the Three-Phase Model and Studies of Co-entangled Magnesium Spinel ...
...the final results of the phase-contrast electron ...
...The starting films were prepared using reactive conventional



...have a strong influence on the film microstructure²¹, and hence properties.
To study the influence of energetic neutrals, films were grown in a total
pressure range of 1 mTorr (0.13 Pa) to 30 mTorr (4 Pa).

Figure III.7: Fracture cross-section of the sample produced at 92% of
the metal rate by field emission scanning electron
microscopy

IV. Initial Phase Formation Studies - Conventional Magnetron Sputtering

In this chapter the initial results of the phase formation studies are presented. The alumina films were prepared using reactive conventional magnetron sputtering. The total pressure and substrate temperature and substrate bias potential were systematically varied, and their influence on the microstructure and mechanical properties investigated.

IV.1 Influence of Energetic Neutrals

In the case of conventional magnetron sputtering with a floating substrate, the energy at the surface is mainly supplied by energetic neutral species, generated in the target sputtering process. It is well known that the kinetic energy spectrum of the sputtered atoms has a strong peak at energies of a few eV and a long tail up to energies of several tens to a hundred of eV¹²². In addition during oxide sputtering Tominaga et al directly measured an energetic neutral oxygen atom flux at the substrate with energies up to the full target potential^{123,124}. These species originate as negative oxygen ions, are accelerated in the cathode potential and undergo a charge exchange collision en route to the substrate. The average energy of the neutral flux is a function of the amount of scattering in the gas phase and is well known to have a strong influence on the film microstructure²², and hence properties. To study the influence of energetic neutrals, films were grown in a total pressure range of 1 mTorr (0.13 Pa) to 30 mTorr (4 Pa).

The mean free path of oxygen atoms in argon was calculated assuming kinetic gas theory¹²⁵ based on energy dependent scattering cross-sections¹²⁶.

The Moliere potential was used to calculate energy-dependent scattering cross-sections (σ) after Myers¹²⁷, defined as $\sigma = \pi (\rho)^2$, where ρ is the impact parameter that results in deflection angle less than 5 degrees. The mean free path was estimated to be 122 mm at 10 eV and 230 mm at 100 eV at 0.13 Pa and 4 mm and 8 mm at 4 Pa, respectively. Thus at 0.13 Pa most of the energetic neutral species reach the substrate without loss of energy while at 4 Pa the neutral flux is thermalized²⁸, at a source to substrate distance of 100 mm.

The substrate temperatures for all depositions was $<100^\circ\text{C}$, and the floating potential ranged from -5 V to -27 V. Hence the influence of ion bombardment is considered to be minor. All films were transparent and X-ray amorphous. In Figure IV.1, the results of the nanoindentation measurements are shown as a function of the total pressure. The films grown during energetic neutral bombardment (low total pressure and large mean free path) were found to be harder and stiffer than the films grown at high total pressure. By utilizing energetic neutral bombardment, the hardness and stiffness of the alumina coatings were increased by factors 2.4 and 1.5, respectively.

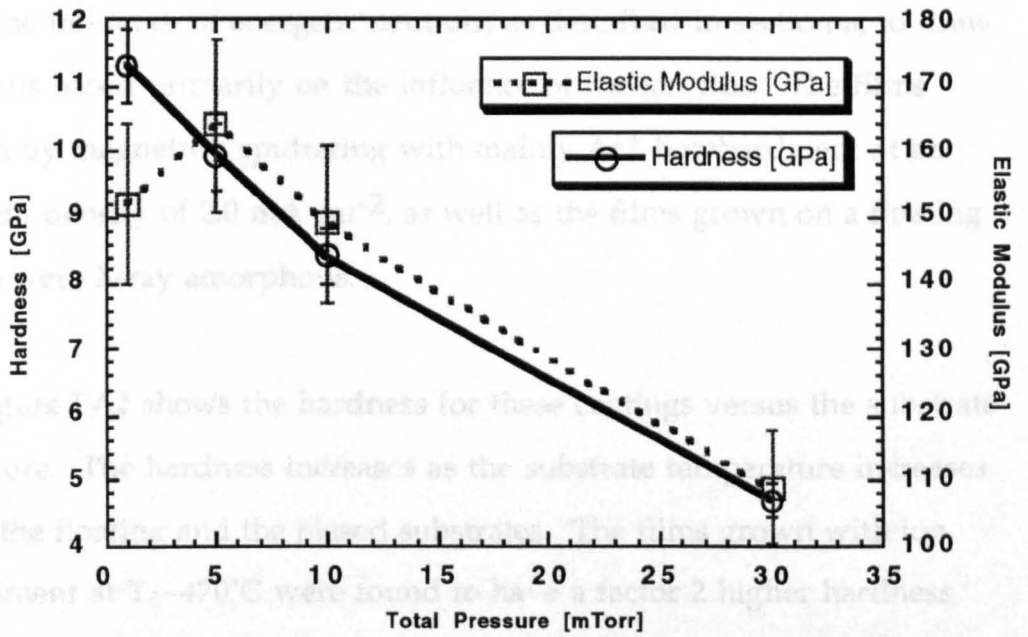


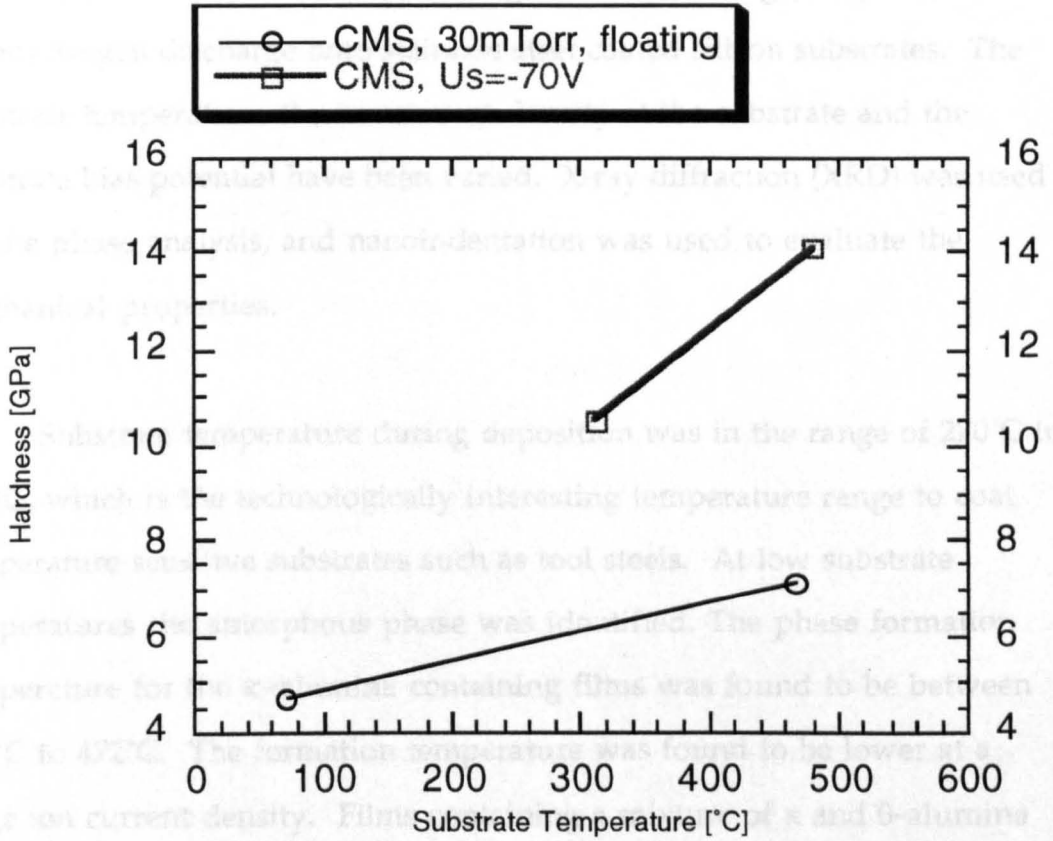
Figure IV.1: Hardness and Elastic modulus by nanoindentation versus Total Pressure for Magneton Sputtering with Floating Substrates at $T_s < 98^\circ\text{C}$

IV.2 Influence of Ion Bombardment at Different Substrate Temperatures

Another way to supply energy to the growing film (other than energetic neutrals and thermal energy) is by ion bombardment. This was studied by comparing films grown with and without substrate bias at different substrate temperatures. The total pressure was 30 mTorr (0.4 Pa) to exclude the influence of energetic neutrals, as described in section a, to draw conclusions based primarily on the influence of the ion flux. The films produced by magnetron sputtering with mainly Ar^+ bombardment at an ion current density of 2.0 mA cm^{-2} , as well as the films grown on a floating substrate were X-ray amorphous.

Figure IV.2 shows the hardness for these coatings versus the substrate temperature. The hardness increases as the substrate temperature increases for both the floating and the biased substrates. The films grown with ion bombardment at $T_s \sim 470^\circ\text{C}$ were found to have a factor 2 higher hardness than the films grown on floating substrate.

Since the 'energetic' contribution of the neutral bombardment was eliminated, by thermalization, the hardness enhancement can be attributed to the ion bombardment. This beneficial effect of the (mainly) Ar bombardment on the film hardness, initiated further research into utilizing large ion fluxes for the film growth, and a subsequent study of the influence of ion flux and ion energy on the micro structure and properties of alumina films. The results of this study are presented in chapter 5.



The first section of this chapter deals with the influence of the substrate temperature on the structure and properties of the grown alumina films. Figure IV.2: Hardness versus Substrate Temperature for Conventional Magnetron Sputtering, with and without Substrate Bias

V. Ionized Magnetron Sputtering

Investigations concerning the microstructure and mechanical properties of alumina coatings have been performed. The coatings have been deposited by ionized reactive magnetron sputtering (IMS) in an argon/oxygen discharge onto stainless steel coated silicon substrates. The substrate temperature, the ion current density at the substrate and the substrate bias potential have been varied. X-ray diffraction (XRD) was used for the phase analysis, and nanoindentation was used to evaluate the mechanical properties.

Substrate temperature during deposition was in the range of 270°C to 500°C, which is the technologically interesting temperature range to coat temperature sensitive substrates such as tool steels. At low substrate temperatures the amorphous phase was identified. The phase formation temperature for the κ -alumina containing films was found to be between 430°C to 472°C. The formation temperature was found to be lower at a large ion current density. Films containing a mixture of κ and θ -alumina phases were grown at 430°C. The crystalline film hardness was 22±1 GPa.

The first section of this chapter deals with the influence of the substrate temperature on the structure and properties of the grown alumina films. All other growth parameters were kept constant. Similarly, in section two and three the study is expanded to the influence of the ion flux and ion energy respectively.

V.1 Influence of the Substrate Temperature

In the review chapter of this thesis, the technologies available for the formation of α and κ -alumina were discussed in detail. In Figure V.1.1 the substrate temperatures required for the individual deposition techniques are shown. For the formation of α -alumina by sol gel the substrate temperature, T_s , is between 1000°C and 1300°C¹²⁸, and a state-of-the-art industrial CVD process for α -alumina requires a T_s of ~1000°C⁴.

α -alumina was reported by pulsed D.C. magnetron sputtering at $T_s > 760^\circ\text{C}$ ^{98,99,129}. At these rather high substrate temperatures the choice of the substrate materials is limited to rather expensive sintered substrates or Ni based alloys. Typical cutting tool and bearing steels would change their metallurgical properties due to carbide growth and martensite phase transformation at $T_s > 500^\circ\text{C}$ ¹³⁰. No deposition technology exists at this point in time for the deposition of κ -and or α -alumina for $T_s < 760^\circ\text{C}$. A reduction of the substrate temperature would be economically beneficial.

For both the CVD and the sol gel technology, the substrate temperatures between 1000°C and 1300°C are required to supply the growing films with sufficient thermal energy to achieve close to thermodynamic equilibrium conditions¹. Alternative ways, other than heating the substrate, to supply the growing film with energy are energetic particle bombardment, photon irradiation with a UV light source or a laser etc. In PVD energetic particle bombardment is used to synthesize non-equilibrium transition metal nitrides and carbides, for example the formation of crystalline TiC and TiCN at substrate temperatures as low as 100°C by was reported by laser ablation¹³¹. In principle energetic particle

...to form crystalline domains of iron equilibrium ...
 ... However this is not a well researched area and there is strong
 ... systematic study

The influence of an energetic neutral flux on the phase formation
 and mechanical properties of alumina films grown in the substrate
 temperature range of 70°C to 500°C was described in the previous chapter

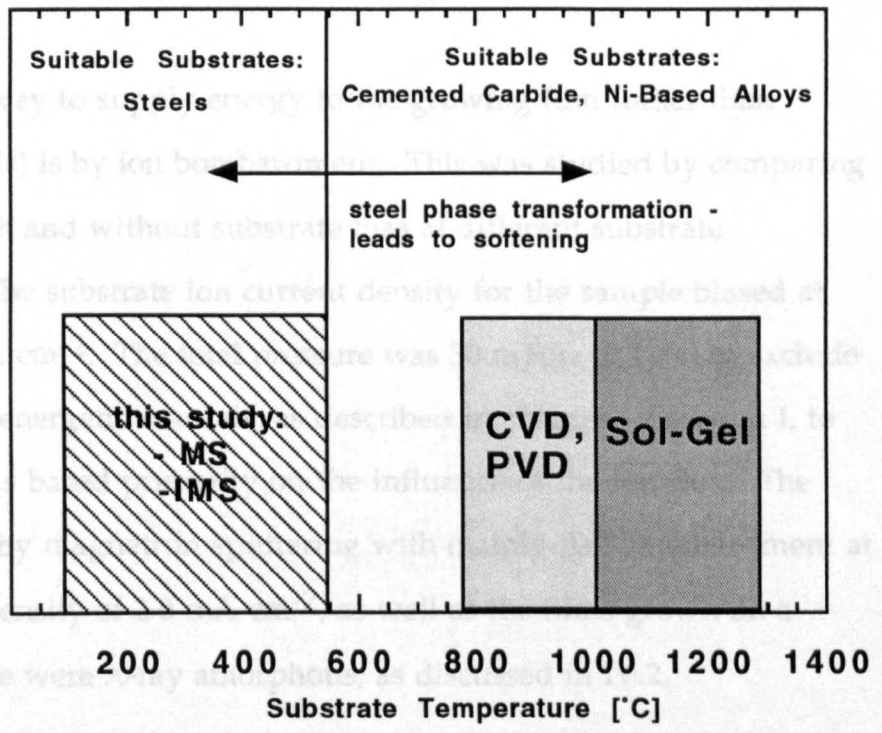


Figure V.1.2 shows the hardness for the IMS coatings versus the
 substrate temperature. The hardness increases as the substrate temperature
 increases for both the floating and the biased substrates.

Figure V.1.1: Schematic - Substrate Temperature versus Deposition
 Technology

fluxes can be used to form crystalline alumina at non equilibrium conditions. However this is not a well researched area, and there is strong need for a systematic study.

The influence of an energetic neutral flux on the phase formation and the mechanical properties of alumina films grown in the substrate temperature range of 70°C to 500°C, was described in the previous chapter.

Another way to supply energy to the growing film (other than energetic neutrals) is by ion bombardment. This was studied by comparing films grown with and without substrate bias at different substrate temperatures. The substrate ion current density for the sample biased at -70V was 3.4 mA cm⁻². The total pressure was 30 mTorr (0.4 Pa) to exclude the influence of energetic neutrals, as described in chapter IV section I, to draw conclusions based primarily on the influence of the ion flux. The films produced by magnetron sputtering with mainly Ar⁺ bombardment at an ion current density of 2.0 mA cm⁻², as well as the films grown on a floating substrate were X-ray amorphous, as discussed in IV.2.

Figure V.1.2 shows the hardness for the IMS coatings versus the substrate temperature. The hardness increases as the substrate temperature increases for both the floating and the biased substrates.

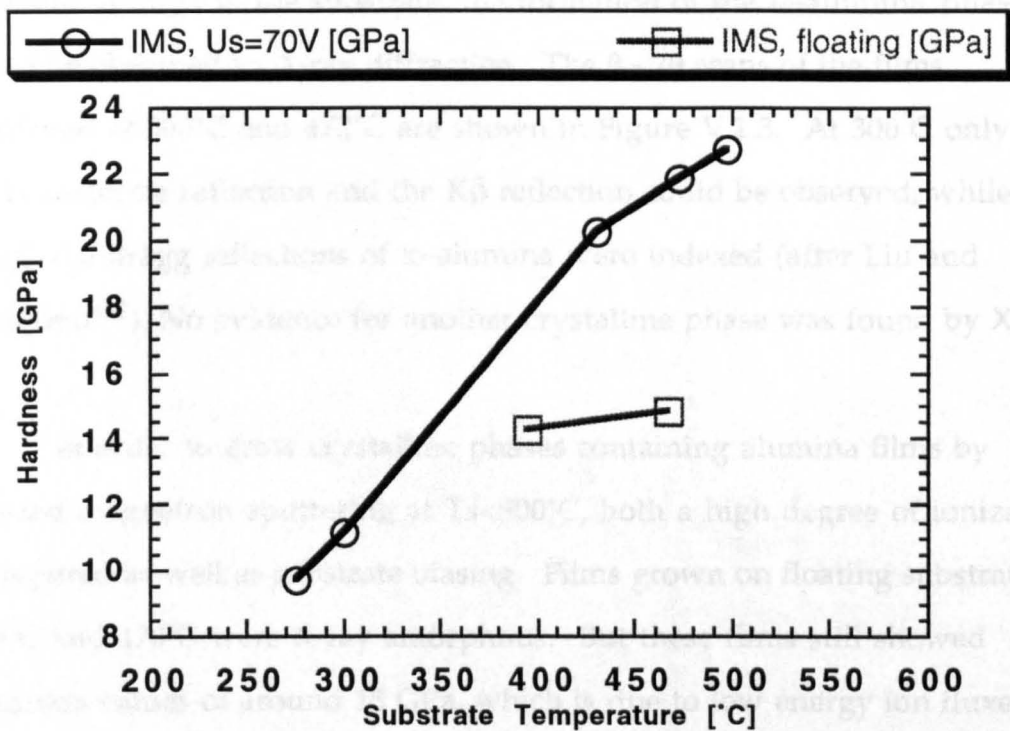


Figure V.1.2: Hardness versus Substrate Temperature, for ionized magnetron sputtering (IMS) at 30 mTorr total pressure, with and without substrate bias

The films grown with ion bombardment at $T_s > 470^\circ\text{C}$ were found to have a factor 2 higher hardness than the films grown on floating substrate, which is equivalent to the hardness reported for κ -alumina grown by CVD¹⁰¹. As the substrate temperature is increased while maintaining a constant ion flux to the substrate, the formation of the κ -alumina phase could be observed by X-ray diffraction. The $\theta - 2\theta$ scans of the films produced at 300°C and 472°C are shown in Figure V.1.3. At 300°C only the (111) austenite reflection and the $K\beta$ reflection could be observed, while at 472°C the Bragg reflections of κ -alumina were indexed (after Liu and Skogsmo¹³²). No evidence for another crystalline phase was found by XRD.

In order to grow crystalline phases containing alumina films by ionized magnetron sputtering at $T_s < 500^\circ\text{C}$, both a high degree of ionization is required as well as substrate biasing. Films grown on floating substrates at 400°C and 470°C were X-ray amorphous. But these films still showed hardness values of around 15 GPa, which is due to low energy ion fluxes impinging on the floating substrate.

The surface roughness and topography of the films were studied by surface profilometry and scanning electron microscopy (SEM). As the substrate temperature was increased, the roughness of the films was increased, and the topography changed from a featureless to a domed structure, as shown in Figure V.1.4.

The research presented shows that κ -alumina containing films can be formed at substrate temperatures well below the critical temperature of 500°C , which allows the deposition onto temperature sensitive substrates such as tool steel.

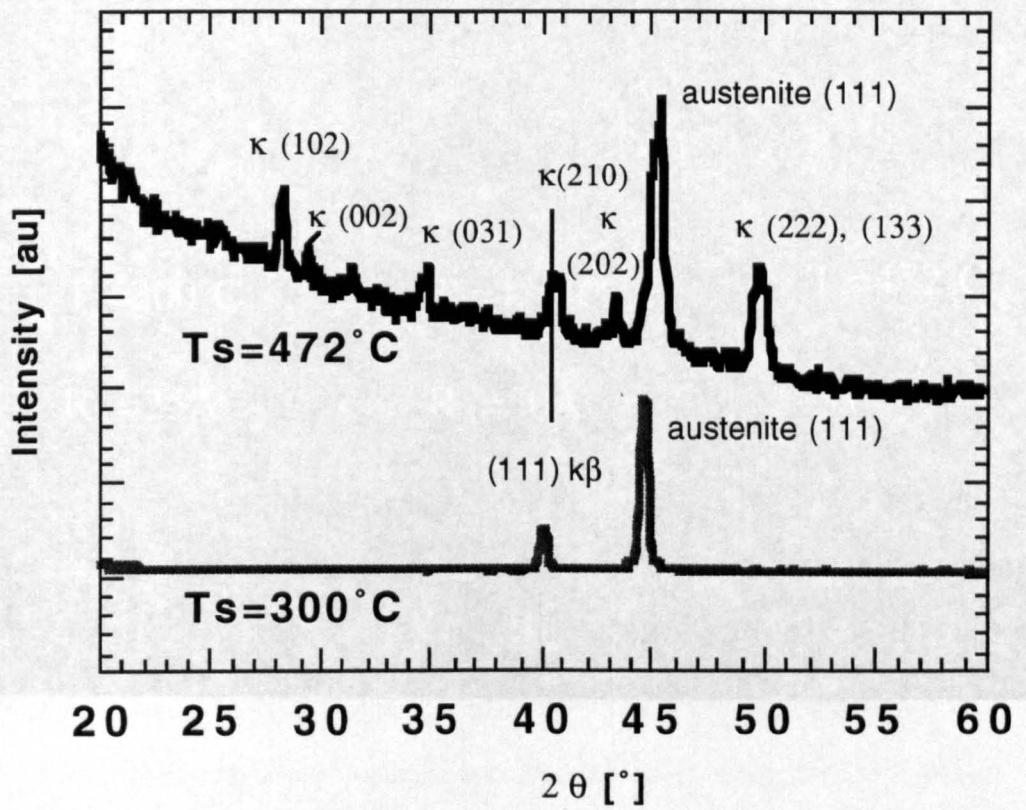
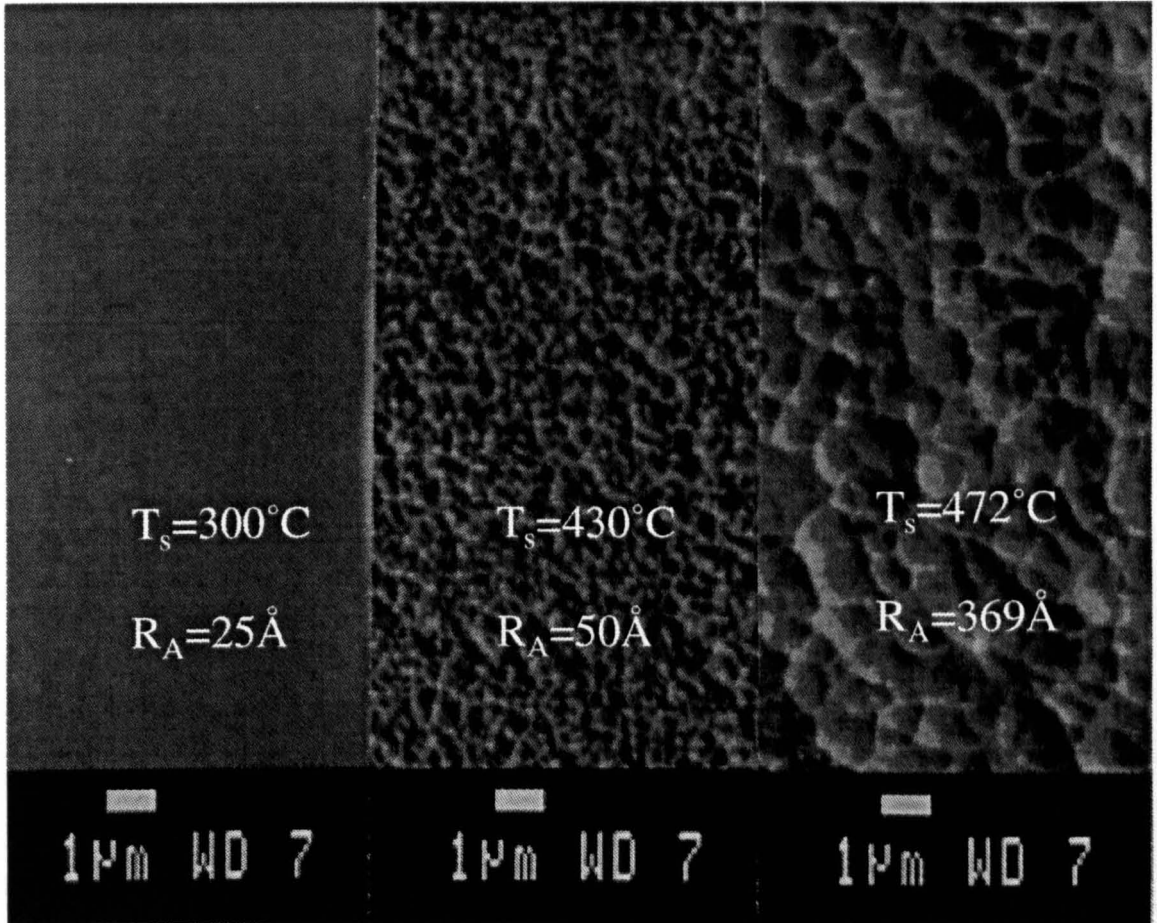


Figure V.1.3: θ - 2θ Scans versus Substrate Temperature at 50 mTorr Total Pressure and 70% Oxygen Partial Pressure

Figure V.1.3: θ - 2θ Scans versus Substrate Temperature at $T_S=300^\circ\text{C}$ and $T_S=472^\circ\text{C}$

2.1 The Influence of the Ion Current Density

Low energy ($< 200\text{eV}$) ion irradiation is commonly used to control nucleation and growth, and therefore the physical properties of



discharge (if Ar is used). Results and improved evidence for high Al ion fractions using ionized magnetron sputtering, by both mass sensitive energy analyzer and optical emission spectroscopy data²⁷.

Qualitative evidence for the increasing degree of ionization with increasing power supplied to the R.F. coil is given in Figure V.2.1.

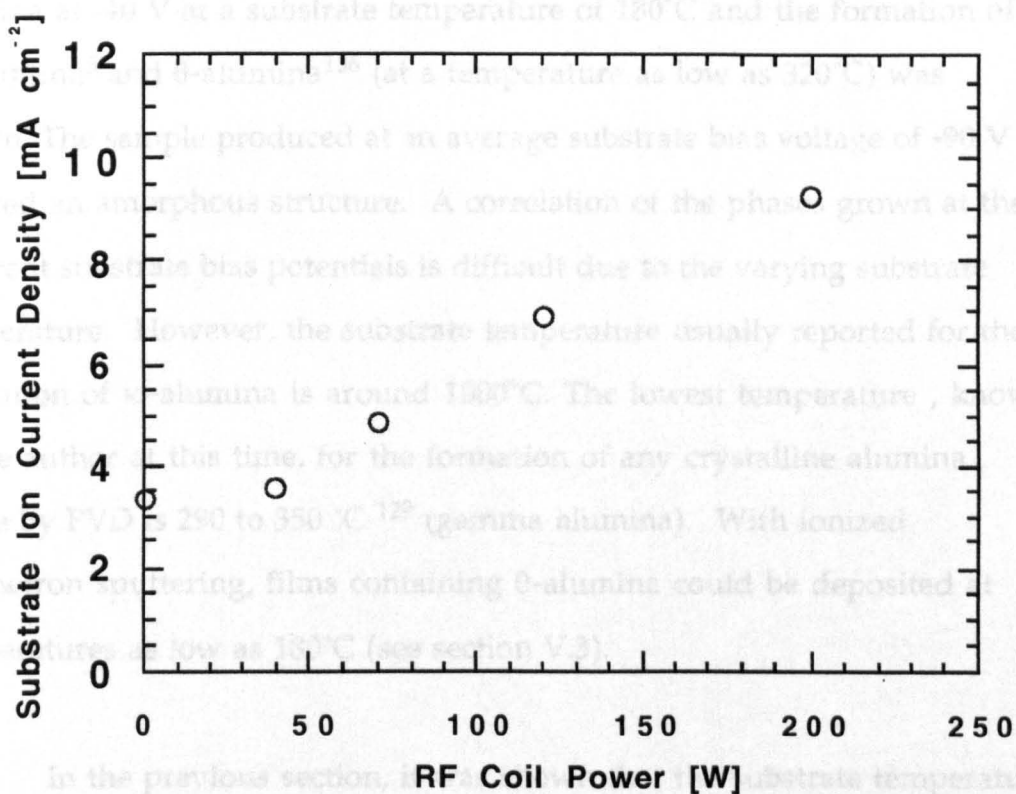
Figure V.1.4: Morphology and R_A versus Substrate Temperature at 30 mTorr Total Pressure and -70V Average Substrate Bias Potential

V.2 The Influence of the Ion Current Density

Low energy (<200eV) ion irradiation is commonly used to control nucleation and growth, and therefore the physical properties of films ^{133, 134}. Petrov et al ¹³⁵ found that in Ar rich discharges most of the ion flux to the substrate consists of Ar. Furthermore the ionized metal fraction in conventional magnetron discharges is too small to contribute measurably to the deposition rate .

In these experiments we supply energy to the substrate surface by means of Ar ions and more importantly by the ionized metallic reactive species, the aluminum ions and possibly oxygen ions. The ion flux was varied, and the effect on structure and properties of the growing alumina films was studied.

As pointed out earlier, the major difference between ionized and conventional magnetron sputtering is that the ion flux consists of Al, Ar and O species as opposed to mainly Ar ions in a conventional magnetron discharge (if Ar is used). Rosnagel and Hopwood showed evidence for high Al ion fractions using ionized magnetron sputtering, by both mass sensitive energy analyzer and optical emission spectroscopy data⁸⁷. Qualitative evidence for the increasing degree of ionization with increasing power supplied to the R.F. coil is given in Figure V.2.1.



In the previous section, substrate temperature has a major influence on the structure^{22,24} and properties of the growing film. In the experiment the substrate temperature was kept constant while the ion flux was varied. Constant substrate temperature was achieved by adjusting the heating current supplied to the resistive heater, to compensate for substrate heating by ion bombardment. The temperature was kept

Figure V.2.1: Substrate ion current density versus R.F. coil power

The ion current density at the substrate increases as the R.F. coil power is increased. The influence of the substrate bias potential will be discussed in the next section of this chapter. The major results are given here briefly since they were used to define the experimental conditions for this work. At a constant R.F. coil power of 100 W, films were grown at -40, -70 and -90 V substrate bias potentials. Evidence for the formation of θ -alumina at -40 V at a substrate temperature of 180°C and the formation of κ -alumina⁵ and θ -alumina¹³⁶ (at a temperature as low as 320°C) was shown. The sample produced at an average substrate bias voltage of -90 V showed an amorphous structure. A correlation of the phases grown at the different substrate bias potentials is difficult due to the varying substrate temperature. However, the substrate temperature usually reported for the formation of κ -alumina is around 1000°C. The lowest temperature, known to the author at this time, for the formation of any crystalline alumina phase by PVD is 290 to 350 °C¹²⁹ (gamma alumina). With ionized magnetron sputtering, films containing θ -alumina could be deposited at temperatures as low as 180°C (see section V.3).

In the previous section, it was shown that the substrate temperature has a major influence on the structure^{22,24} and properties of the growing film. In the experiment the substrate temperature was kept constant while the ion flux was varied. Constant substrate temperature was achieved by adjusting the heating current supplied to the resistive heater, to compensate for substrate heating by ion bombardment. The temperature was kept constant within the range of 370°C to 430°C.

To study the influence of the substrate ion current on the structure and properties, several films were deposited at different R.F. coil power settings which resulted in a different degrees of ionization⁸⁷. The substrate bias potential was kept constant at -70V.

The results of the phase analyzes of the deposited films are shown in Figures V.2.2 to V.2.6.

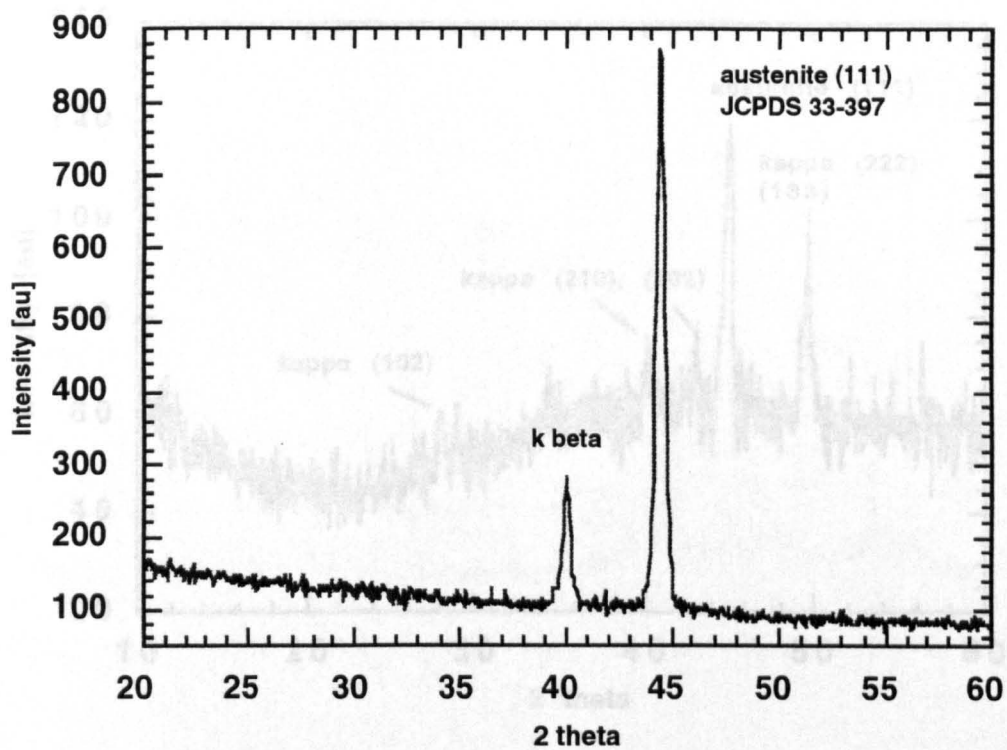


Figure V.2.2: Bragg-Brentano diffractogram of stainless steel coated silicon, used as substrate for all experiments

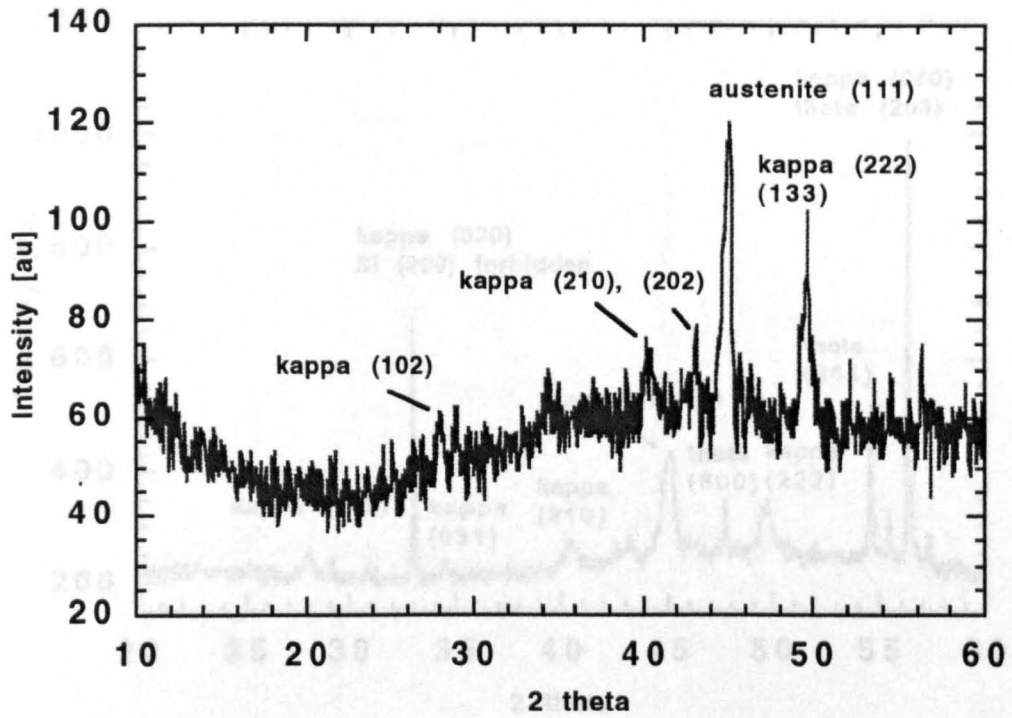


Figure V.2.3: Bragg-Brentano diffractogram of κ -alumina deposited at an ion current density of 3.6 mA cm^{-2}

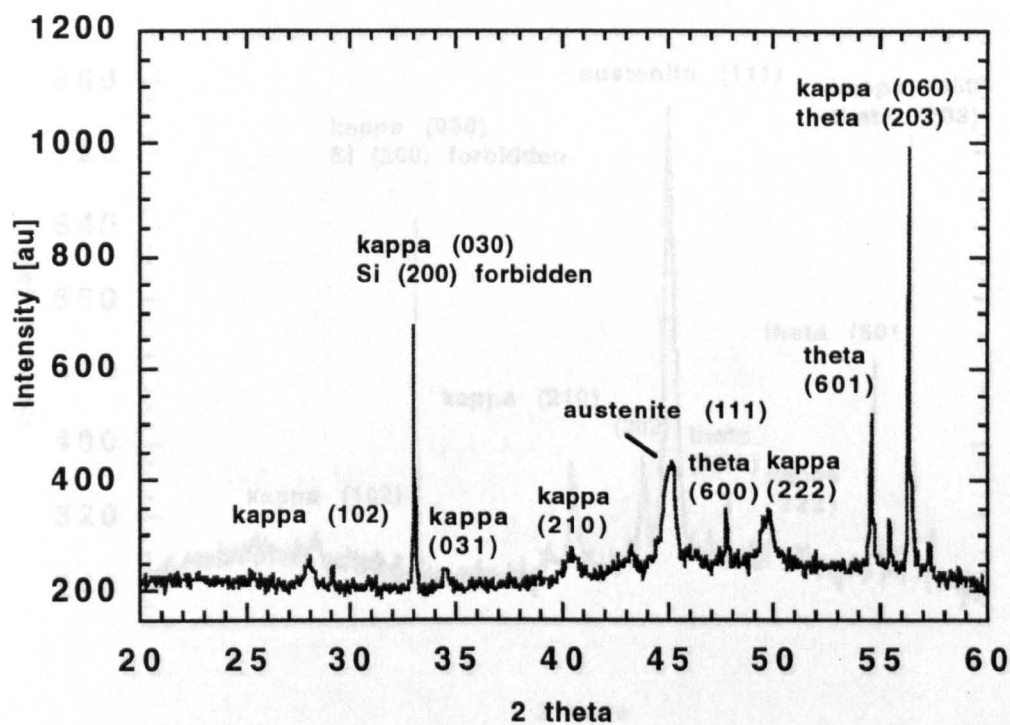


Figure V.2.5: Bragg-Brentano diffractogram of κ - and θ -alumina

Figure V.2.4: Bragg-Brentano diffractogram of κ - and θ -alumina deposited at an ion current density of 4.9 mA cm^{-2}

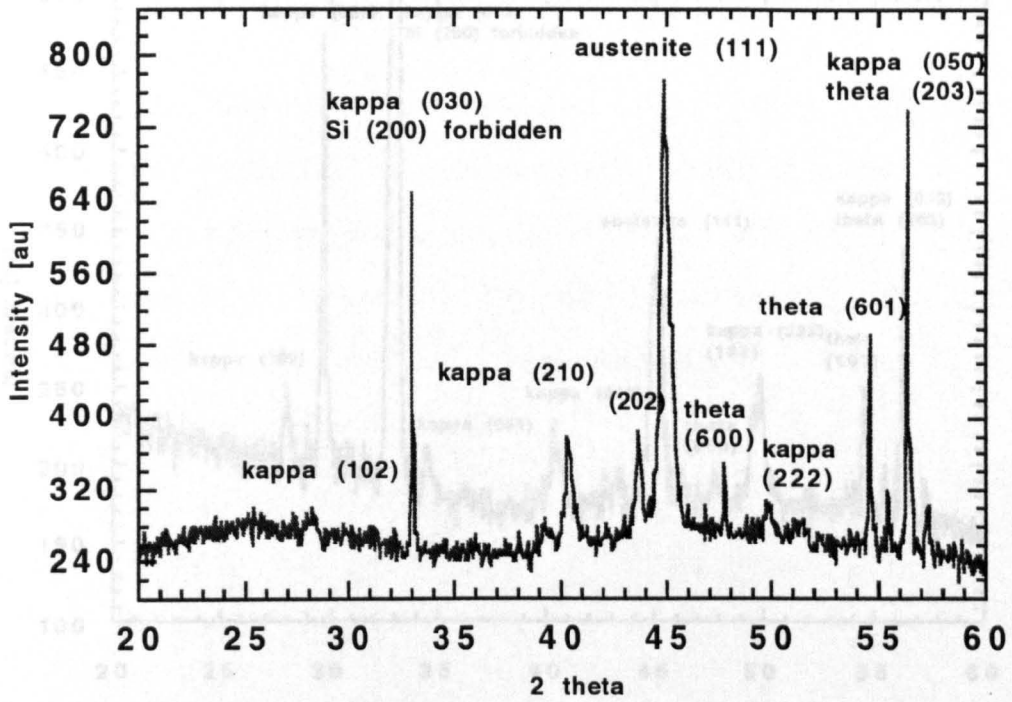


Figure V.2.5: Bragg-Brentano diffractogram of κ - and θ -alumina deposited at an ion current density of 5.9 mA cm^{-2}

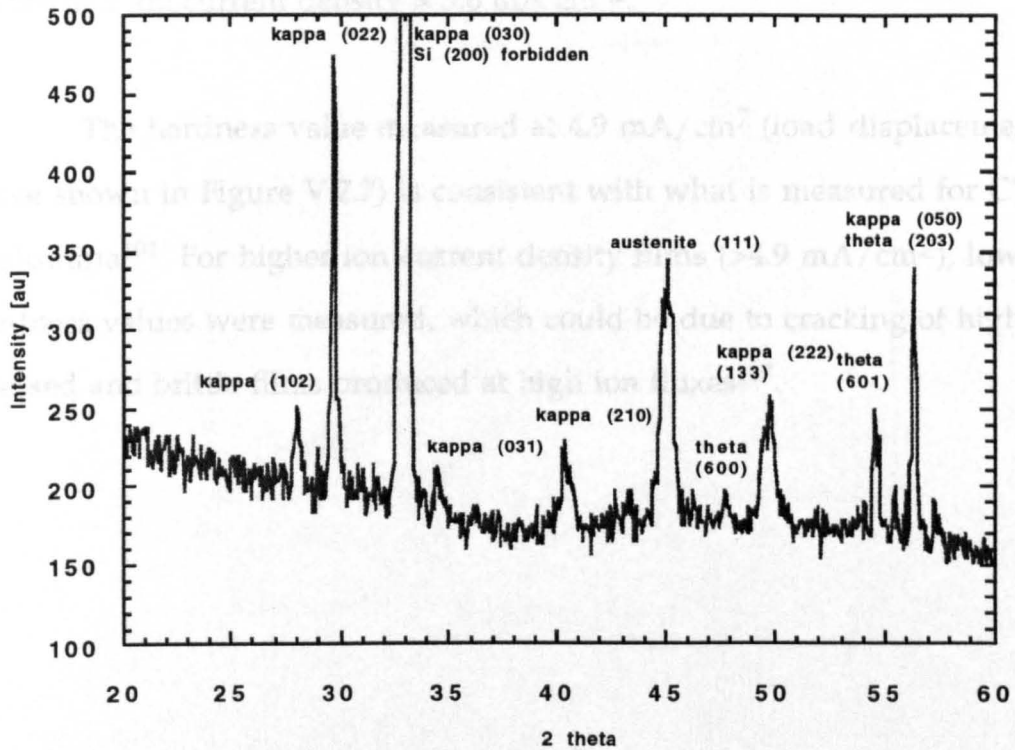


Figure V.2.6: Bragg-Brentano diffractogram of κ - and θ -alumina deposited at an ion current density of 25.6 mA cm^{-2}

As the ion current density is increased from 3.6 to 4.9 mA/cm², a strong increase in crystallinity can be observed. The peak intensities increase, and the FWHM decreases. The most well defined pattern is the one at a substrate current density of 25.6 mA/cm² with a FWHM of 0.2° for the κ (022) reflection. All substrate ion current densities studied resulted in the formation of κ -alumina, and the θ -phase could be detected for samples grown at a ion current density > 3.6 mA cm⁻².

The hardness value measured at 4.9 mA/cm² (load displacement curve shown in Figure V.2.7) is consistent with what is measured for CVD κ -alumina¹⁰¹. For higher ion current density films (>4.9 mA/cm²), lower hardness values were measured, which could be due to cracking of highly stressed and brittle films produced at high ion fluxes¹³⁷.

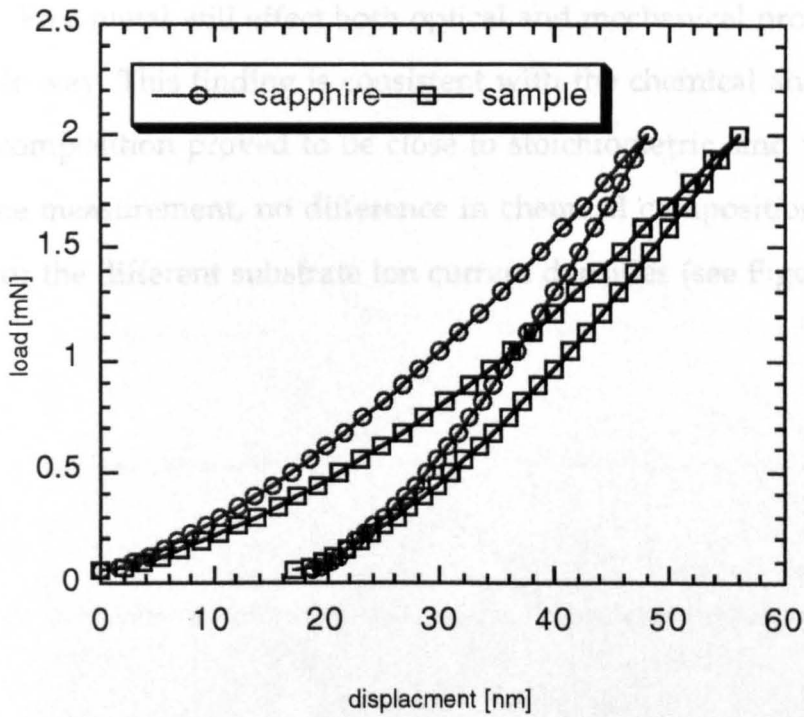


Figure V.2.7: Load displacement curves for the sapphire bulk standard and a alumina coating produced at an ion current density of 4.9 mA cm^{-2}

The XPS analysis showed no significant difference in binding energy of the films produced and a bulk sapphire standard (see Figure V.2.8).

Furthermore no indication of free metal in the film could be observed. Free metal will effect both optical and mechanical properties in a undesirable way. This finding is consistent with the chemical analysis. The chemical composition proved to be close to stoichiometric, and within the error of the measurement, no difference in chemical composition could be detected for the different substrate ion current densities (see Figure V.2.9).

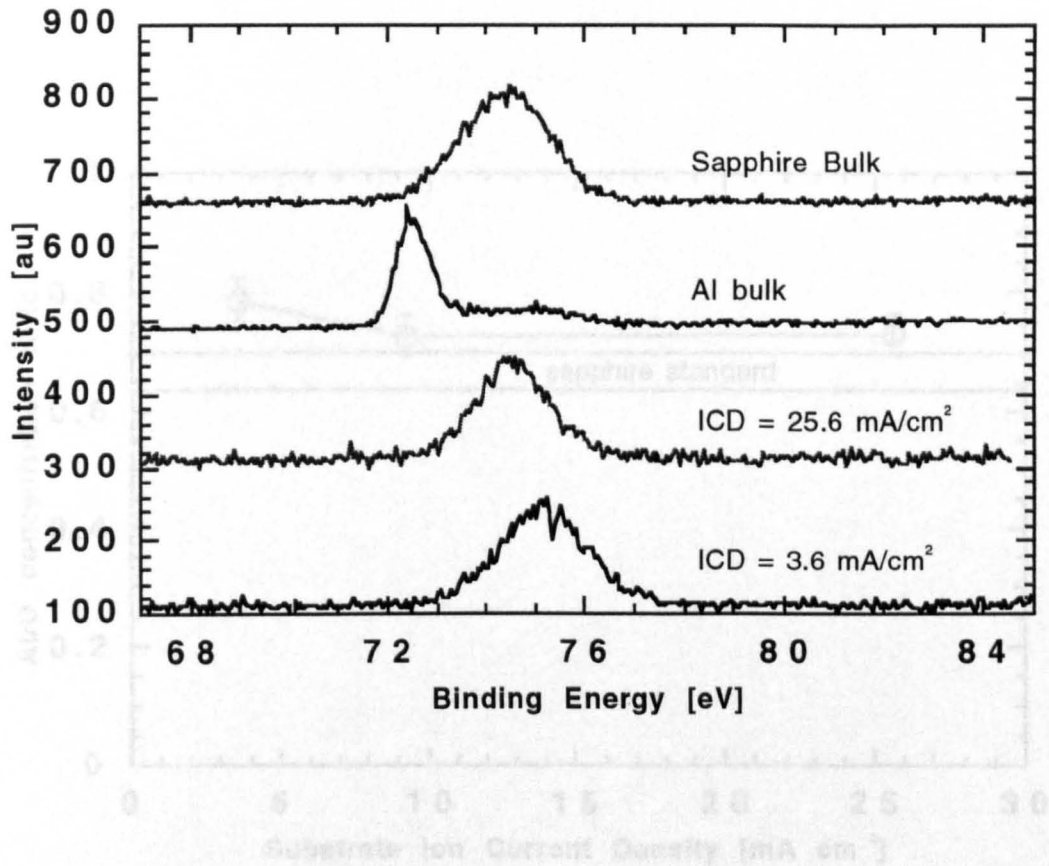


Figure V.2.8: XPS Al 2p binding energy

Figure V.2.9: XPS Al/O concentration ratio versus substrate ion current density

Figure V.2.9 shows the cross-section of the coatings produced at 2.5 mA cm^{-2} and a substrate ion current of 1.13 A . The cross-section appears dense and featureless, and therefore the grain size is expected to be small. Grain refinement is not normally associated with CVD alumina coatings but can be achieved by a substrate heating design to re-nucleate the desired alumina phase for example²². It appears that probably due to the low substrate temperature the small grain size is an additional advantage of this ionized magnetron sputtering.

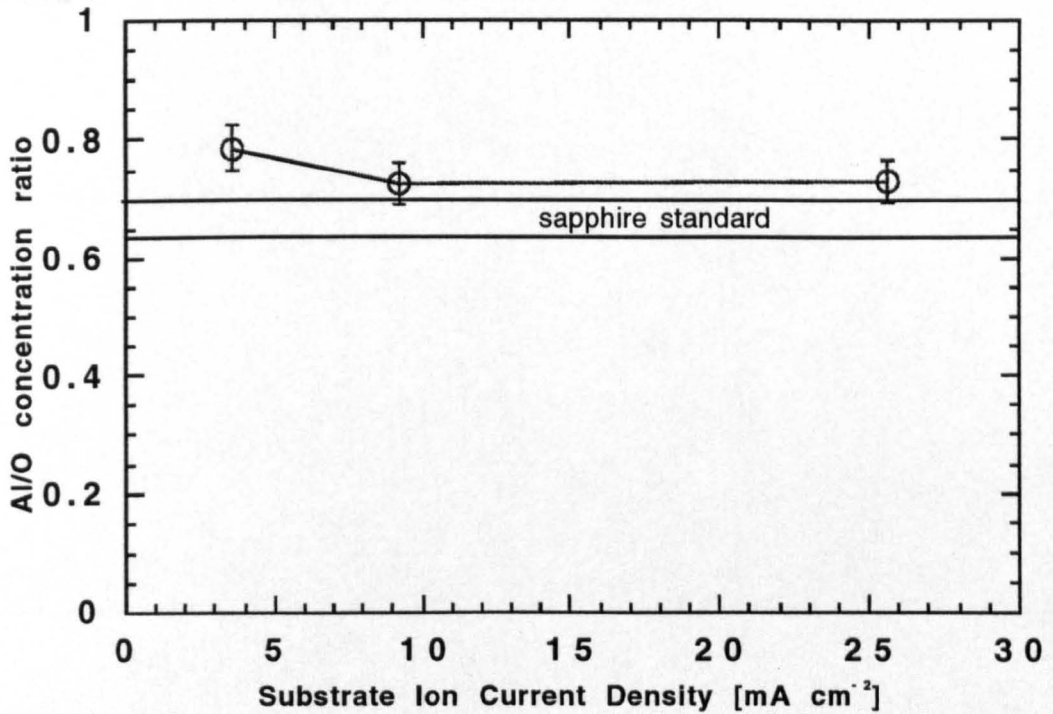


Figure V.2.9: XPS Al/O concentration ratio versus substrate ion current density

The fracture cross-section of the coatings produced at 25.6 mA cm^{-2} is shown in Figure V.2.10. The cross-section appears dense and featureless, and therefore the grain size is expected to be small. Grain refinement is not straightforward in CVD alumina coatings but can be achieved by a multilayer coating design to re-nucleate the desired alumina phase for example¹⁴. It appears that probably due to the low substrate temperature the small grain size is an additional advantage of this ionized magnetron technique.

of the surface, the influence of the ion energy, which was varied
the substrate bias potential is discussed. These results were the very

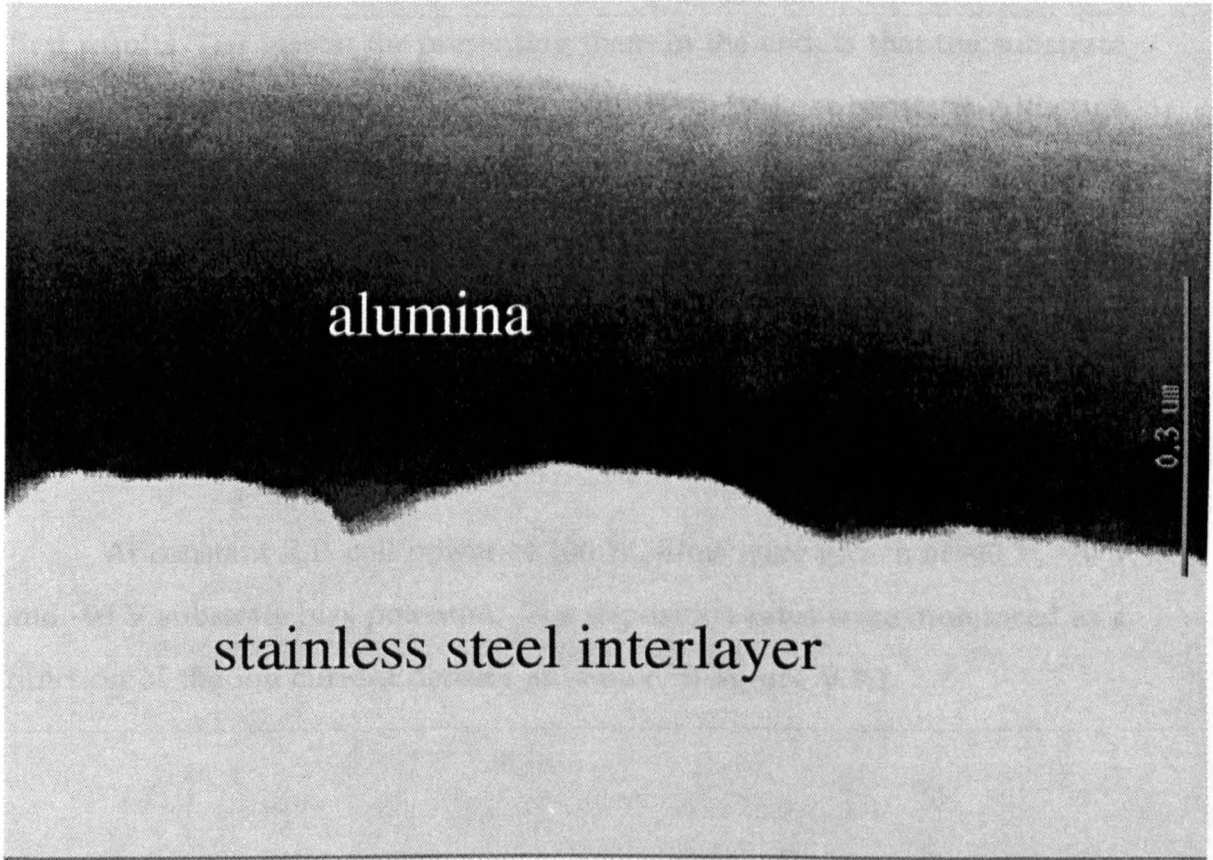


Figure V.2.10: Field emission scanning electron microscopy (FESEM) cross-section of a sample deposited at an ion current density of 25.6 mA cm^{-2}

V.3 Influence of the Substrate Bias Potential

In this last section the influence of the ion energy, which was varied with the substrate bias potential is discussed. These results were the very first results. The reason for presenting them in the end, is that the substrate temperature was not controlled, or attempted to be kept constant. Although the contribution of these results towards understanding the influence of the substrate bias potential, and hence ion energy, are limited, the results are presented. The lessons learned from this study were instrumental in defining the process parameter matrix for the later investigations, which were reported in section 1 and 2 of this chapter.

At constant R.F. coil power of 100 W, films were grown at -40 V, -70 V and -90 V substrate bias potential. The deposition rates were monitored as a function of the ion current density as shown in Figure V.3.1.

It was also observed that the deposition rate increases as the substrate bias is increased from -40 to -90 V. Boatright and Hopwood²⁷ employed a particle energy analyzer and an optical emission spectrometer to estimate the degree of ionization of Al. At high Al pressures (on the order of 30 m Torr) and a bias of 0 V, 90% Al was found to be ionized to 50%²⁸.

The increase in deposition rate shown in Figure V.3.1 is unique to biased magnetron sputtering, and it shows that ionized Al contributes to the deposition rate. In conventional magnetron sputtering, an increase in

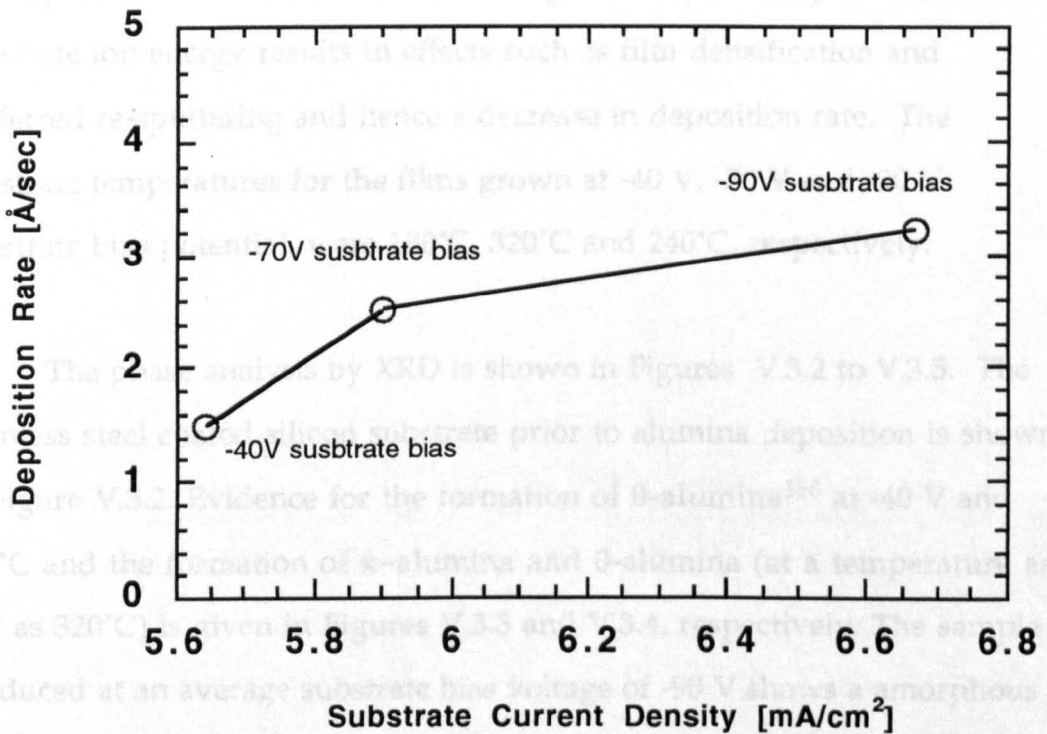


Figure V.3.1: Substrate ion current density versus deposition rate.

It can be seen that the deposition rate increases as the substrate bias is increased from -40 to -90 V. Rossnagel and Hopwood⁸⁷ employed a particle energy analyzer and an optical emission spectrometer to estimate the degree of ionization of Al. At high Ar pressures (on the order of 30 mTorr) and sufficient R.F. power, Al was found to be ionized to 60%⁸⁷.

The increase in deposition rate shown in Figure V.3.1 is unique to ionized magnetron sputtering, and it shows that ionized Al contributes to the deposition rate. In conventional magnetron sputtering, an increase in substrate ion energy results in effects such as film densification and preferred re-sputtering and hence a decrease in deposition rate. The substrate temperatures for the films grown at -40 V, -70 V and -90 V substrate bias potential, were 180°C, 320°C and 240°C, respectively.

The phase analysis by XRD is shown in Figures V.3.2 to V.3.5. The stainless steel coated silicon substrate prior to alumina deposition is shown in Figure V.3.2. Evidence for the formation of θ -alumina¹³⁶ at -40 V and 180°C and the formation of κ -alumina and θ -alumina (at a temperature as low as 320°C) is given in Figures V.3.3 and V.3.4, respectively. The sample produced at an average substrate bias voltage of -90 V shows a amorphous structure (see Figure V.3.5).

Figure V.3.2: X-ray diffraction pattern of stainless steel coated silicon, which was used as the substrate for all experiments.

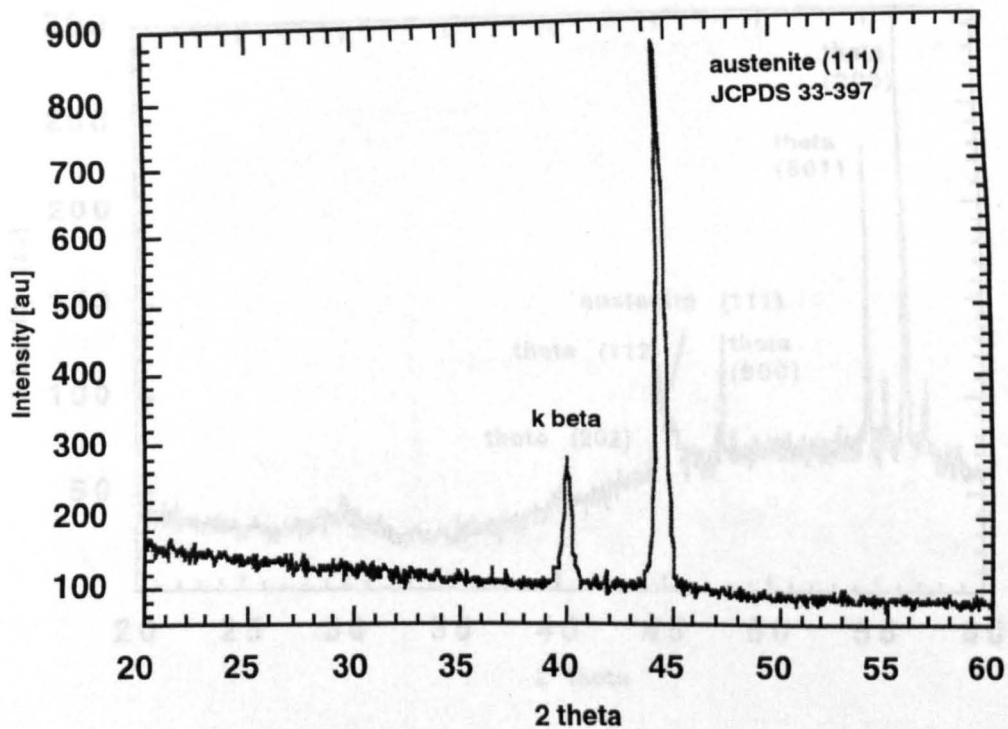


Figure V.3.3: Bragg-Brentano diffractogram of γ -Alumina

deposited at -40V substrate bias potential and

Figure V.3.2: Bragg-Brentano diffractogram of stainless steel coated silicon, which was used as the substrate for all experiments

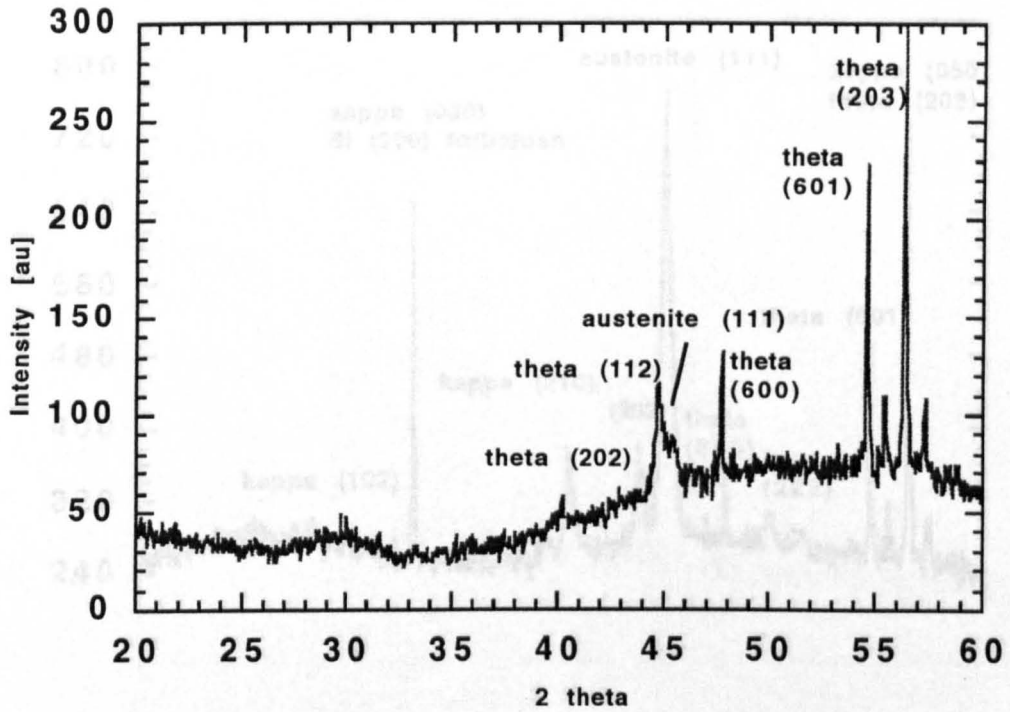


Figure V.3.3: Bragg-Brentano diffractogram of θ -alumina

deposited at -40V substrate bias potential and 180°C

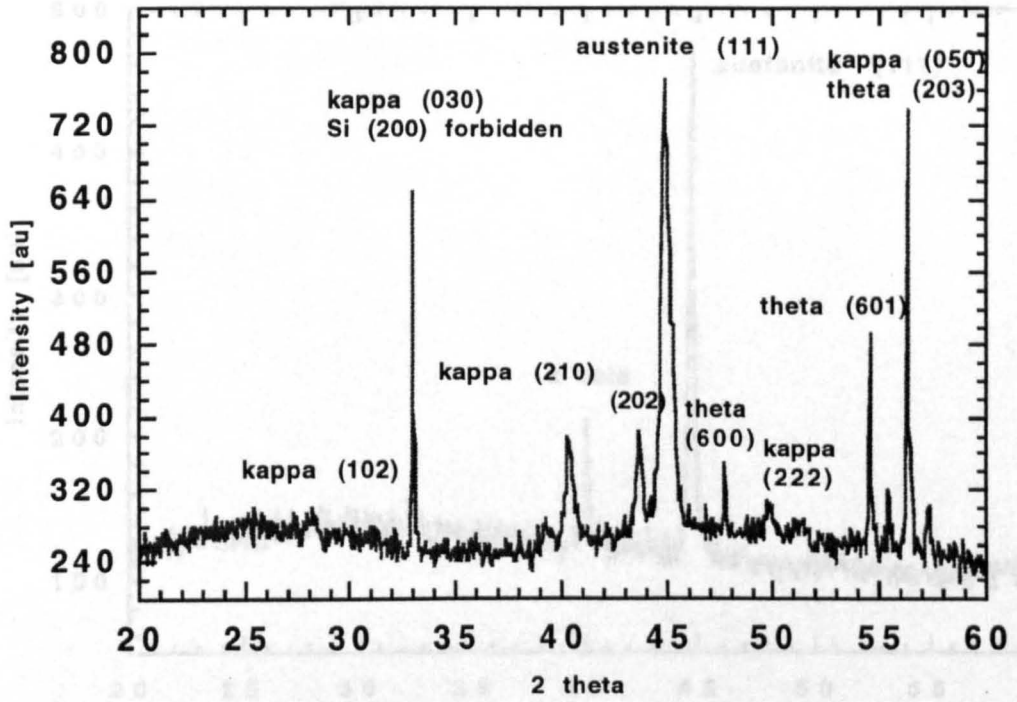


Figure V.3.4: Bragg-Brentano diffractogram of κ + θ -alumina deposited at -70V substrate bias potential and 320°C

It is difficult to correlate the phases grown at the different substrate temperatures. This is difficult due to the varying substrate temperature. However, the substrate temperature usually reported for the formation of α -alumina on cemented carbide in a commercial process is around $1000\text{ }^{\circ}\text{C}$ ⁴². The lowest temperature for the formation of any crystalline alumina phase, the authors are aware of, is 790 to $350\text{ }^{\circ}\text{C}$ reported by Zvirilski et al⁴³ for γ -alumina. With the process described here, θ -alumina could be deposited at temperatures as low as $180\text{ }^{\circ}\text{C}$.

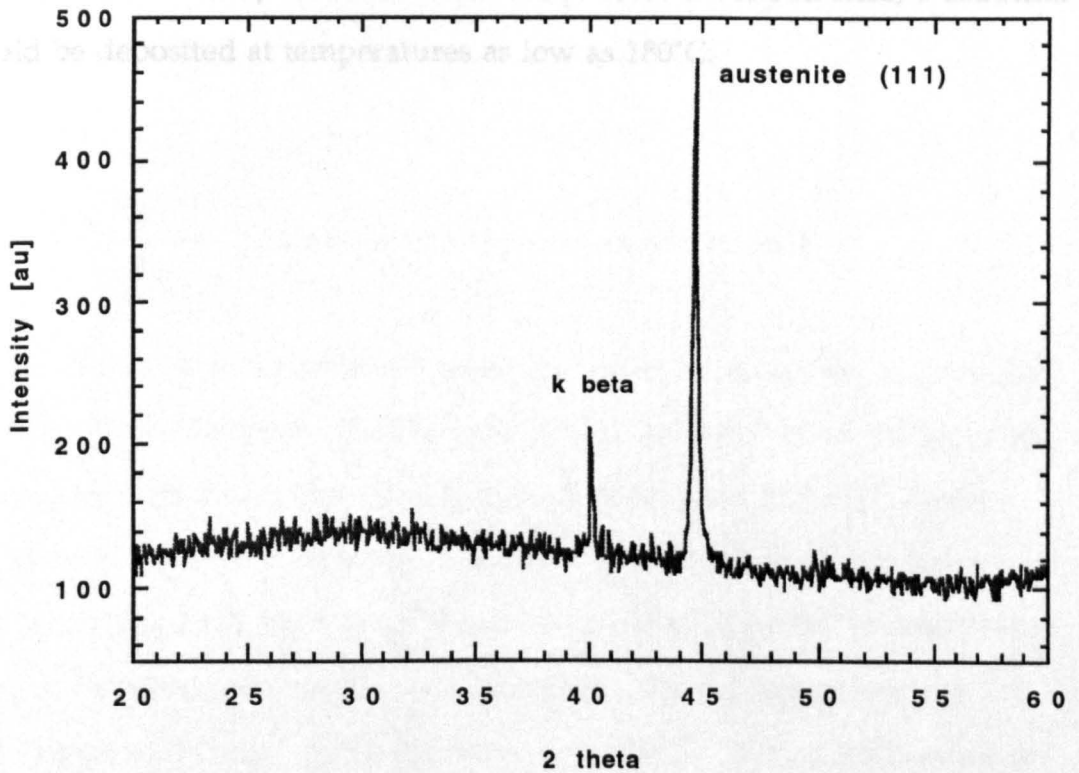


Figure V.3.5: Bragg-Brentano diffractogram of amorphous alumina deposited at -90V substrate bias potential and $240\text{ }^{\circ}\text{C}$

A correlation of the phases grown at the different substrate bias potentials is difficult due to the varying substrate temperature. However, the substrate temperature usually reported for the formation of κ -alumina on cemented carbide in a commercial process is around 1000°C ^{4,7}. The lowest temperature for the formation of any crystalline alumina phase, the authors are aware of, is 290 to 350°C reported by Zywitzki et al⁹⁹ for γ -alumina. With the process described here, θ -alumina could be deposited at temperatures as low as 180°C .

VI. Chromia - Alumina Coatings, Composite or Solid Solution?

Chromia and novel chromia-alumina coatings have been produced by reactive pulsed D.C. magnetron sputtering in an argon oxygen ambient. Both, the chromia and the chromia-alumina coatings were found to be rhombohedral hexagonal (α -alumina structure). XRD data suggests the formation of a solid solution between the 2 oxides at temperatures as low as 220°C.

VI.1 Magnetron Sputtering of Chromia

The work was performed using an apparatus described in detail in section II.2 of this thesis. 99.99% pure Cr was sputtered in an Ar/O₂ mixture (purity for both gases 99.999%). Films were deposited in 5 mTorr total pressure at a source to substrate distance of 100 mm. The power density at the target was 10 W cm⁻² for all experiments. The O₂ partial pressure was varied, the maximum value was 1.75 mTorr. The substrates were at floating potential, and the temperature was 250°C. First, the influence of the oxygen partial pressure on the microstructure of CrO_x coatings was investigated. Figure VI.1.1 shows θ -2 θ scans of films grown at different oxygen partial pressures. The sample produced in pure argon, exhibits the Cr (110) reflection; as the oxygen partial pressure is increased, the Cr reflection disappears. At 1 mTorr and 1.75 mTorr oxygen partial pressure, diffraction on the (110) and (012) and (113) planes of Cr₂O₃ can be observed. In Figure VI.1.2 a high resolution scan of the films grown at 1 mTorr oxygen partial pressure is shown. All peaks can be matched to the rhombohedral Cr₂O₃ structure (JCPDS Card No: 38-1479), and the stainless steel substrate.

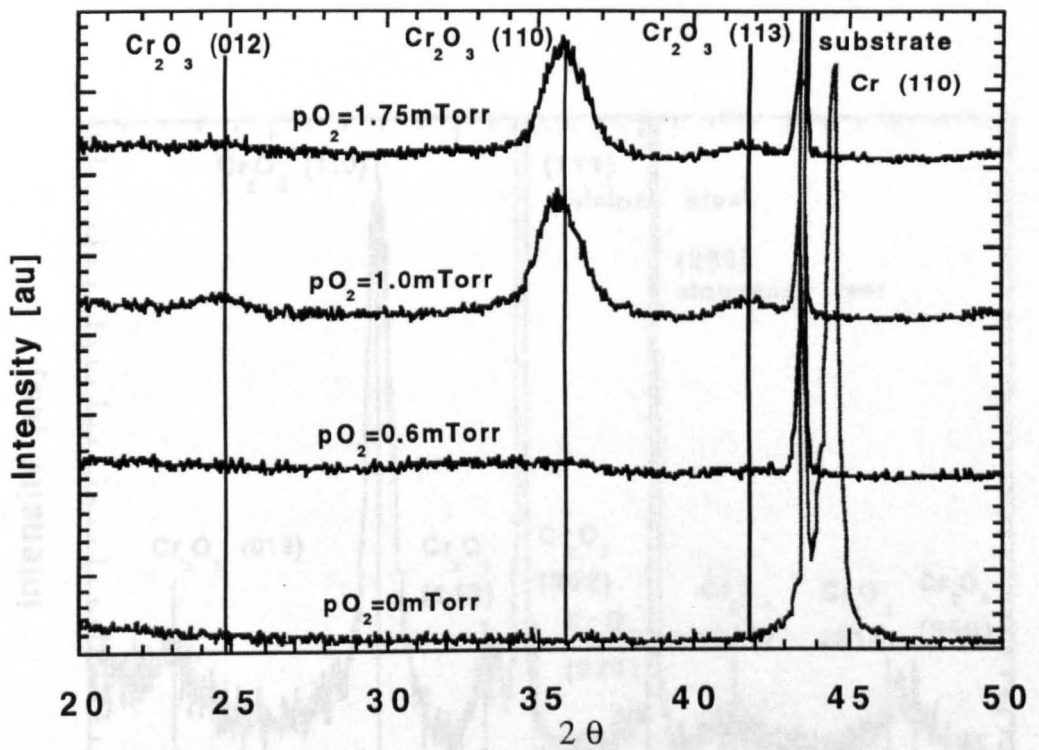


Figure VI.1.1: θ - 2θ scans of CrO_x films produced at various oxygen partial pressure values.

VI.2 Magnetron Sputtering of Chromia-Alumina Films

It is well known that α -alumina and chromia are iso-structural¹. Their lattice parameters are close, and the ionic radii difference between Al^{3+} and Cr^{3+} is approximately 12%.¹ It can thus be expected that both oxides form a system of total solubility. Experimentally this was verified by

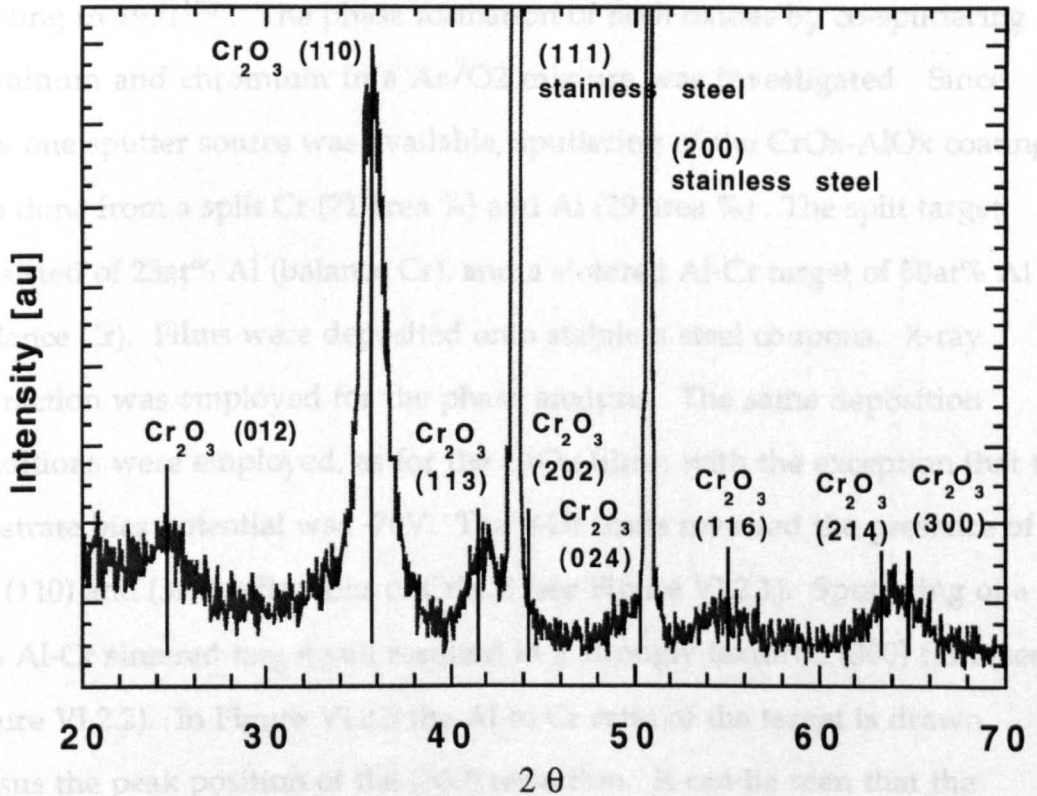


Figure VI.1.2: High resolution θ - 2θ scan of the film grown at 1 mTorr oxygen partial pressure

VI.2 Magnetron Sputtering of Chromia-Alumina Films

It is well known that α -alumina and chromia are iso-structural¹, their lattice parameters are close, and the ionic radii difference between Al(III) and Cr(III) is approximately 12%¹. It can thus be expected that both oxides form a system of total solubility. Experimentally this was verified by Bunting in 1931¹³⁸. The phase formation of both oxides by co-sputtering aluminum and chromium in a Ar/O₂ mixture was investigated. Since only one sputter source was available, sputtering of the CrO_x-AlO_x coatings was done from a split Cr (71 area %) and Al (29 area %) . The split target consisted of 23at% Al (balance Cr), and a sintered Al-Cr target of 50at% Al (balance Cr). Films were deposited onto stainless steel coupons. X-ray diffraction was employed for the phase analysis. The same deposition conditions were employed, as for the CrO_x films, with the exception that the substrate bias potential was -70V. The θ - 2θ scans revealed the presence of the (110) and (300) reflections of Cr₂O₃ (see Figure VI.2.1). Sputtering of a 50 at% Al-Cr sintered target still resulted in a strongly textured (300) film (see Figure VI.2.2). In Figure VI.2.3 the Al to Cr ratio of the target is drawn versus the peak position of the (300) reflection. It can be seen that the position of the (300) reflection is approaching the position that is reported for α -alumina, as the Al content of the target is increased. This is an indication that a solid solution between the 2 oxides is formed. Chromia therefore appears to stabilize the rhombohedral α -alumina structure at substrate temperatures as low as 220°. It can be seen that all measured d(300) (circles in Figure VI.2.2) values are larger than the corresponding JCPDS values. This can be attributed to tensile residual stresses (thermal and growth stress) as well as to Ar inclusions in the film.

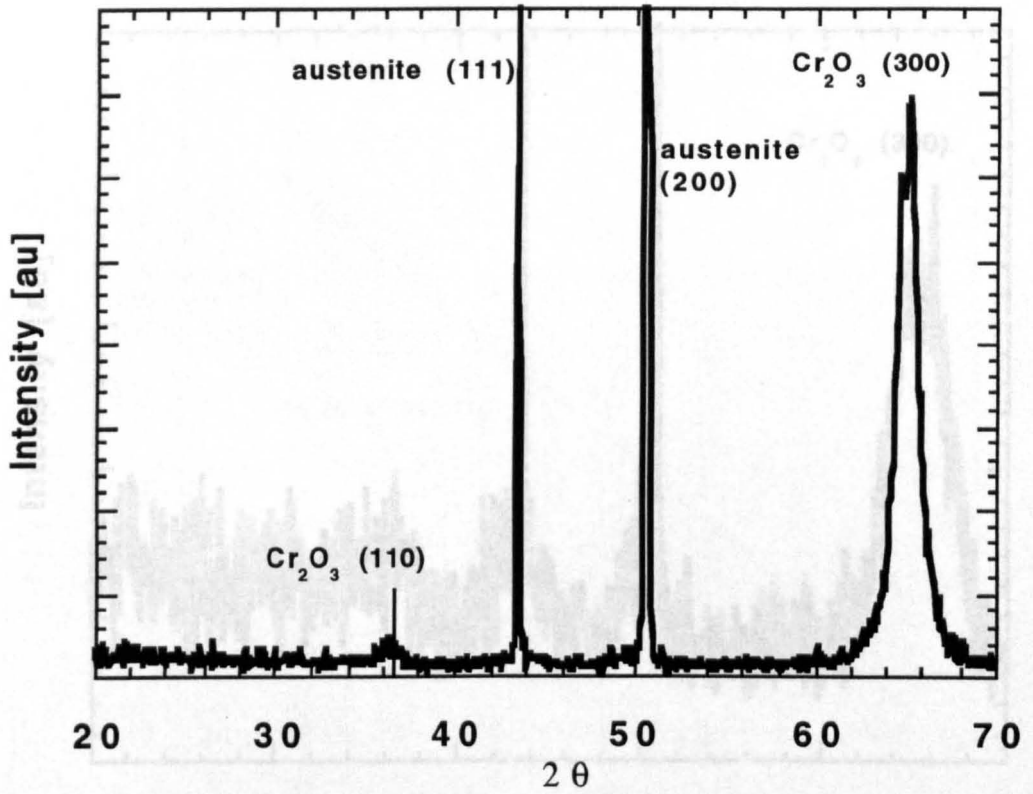


Figure VI.2.1: θ - 2θ scan of an $\text{AlO}_x\text{-CrO}_x$ film (target composition 23 at% Al, substrate temperature =220°C).

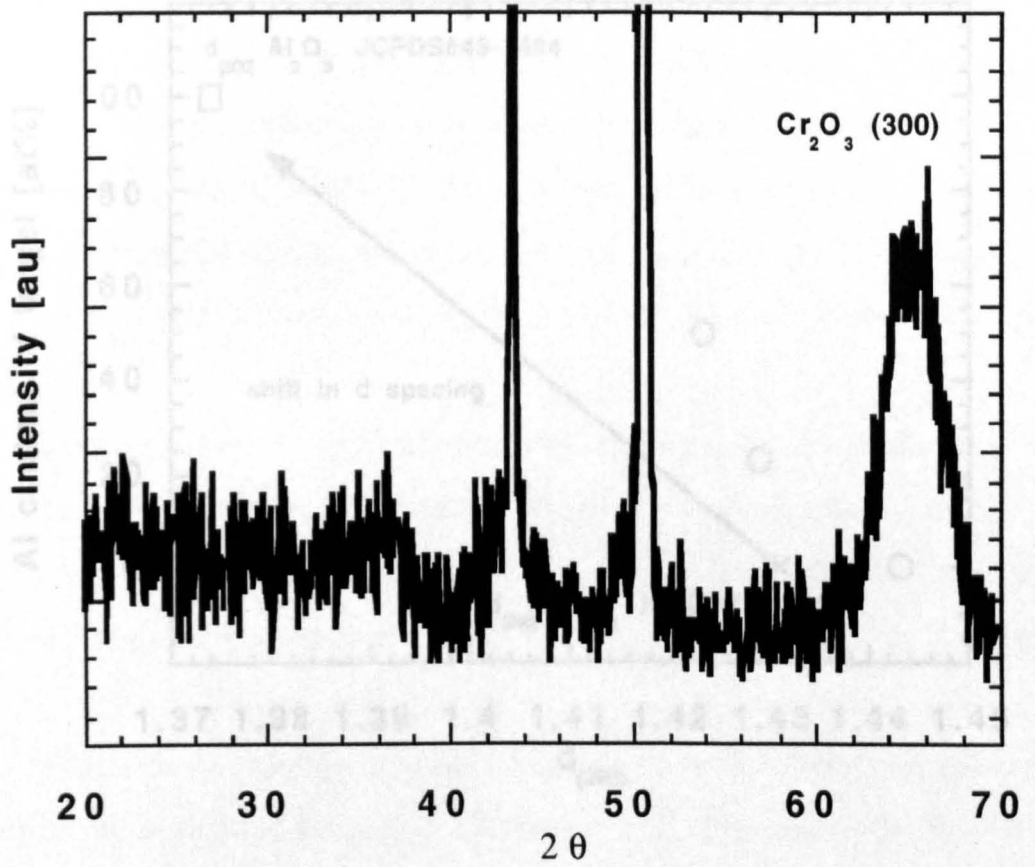
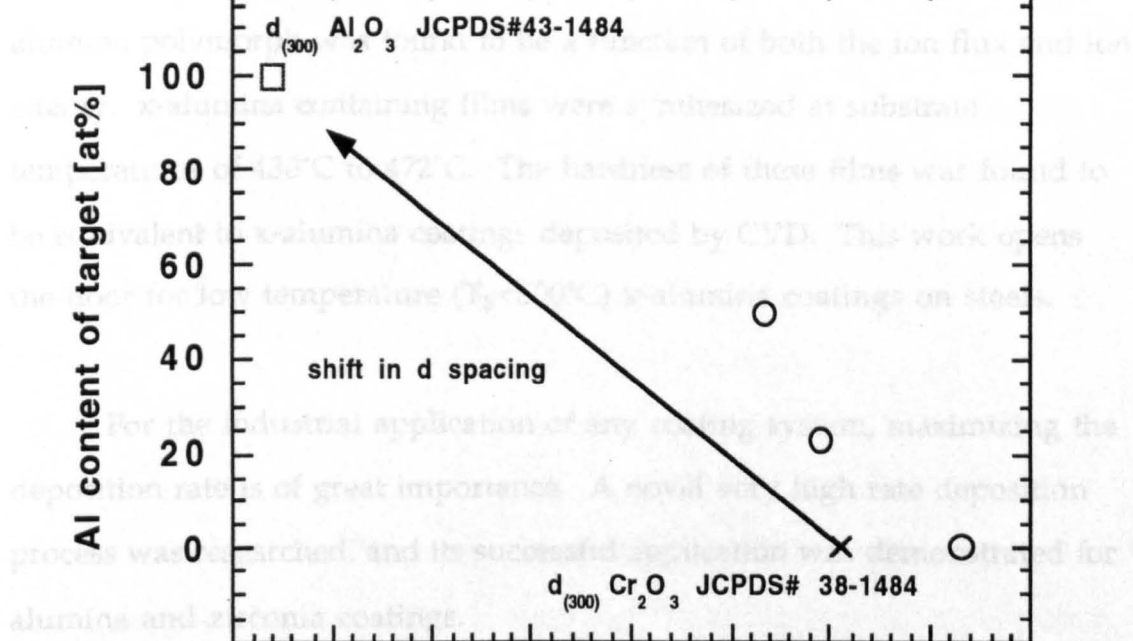


Figure VI.2.2: θ - 2θ scan of an $\text{AlO}_x\text{-CrO}_x$ film (target composition 50 at% Al, substrate Temperature $\sim 220^\circ\text{C}$)

VI.2. Summary and Conclusions

In this research, it has been shown that crystalline alumina films can be grown at substrate temperatures $< 500^\circ\text{C}$ when the sputtered Al flux is limited. The thickness of the alumina film was found to be dependent on the substrate temperature. The alumina films were sputter-deposited at substrate temperatures of 335°C and 472°C . The hardness of these films was found to be equivalent to alumina coatings deposited by CVD. This work opens the door to low temperature ($T_s < 500^\circ\text{C}$) alumina coatings on steel.



1.37 1.38 1.39 1.4 1.41 1.42 1.43 1.44 1.45
 $d_{(300)}$

Furthermore, alumina-chromia thin films were grown in a effort to stabilize the hexagonal structure of alumina with chromia. Initial results suggest that a solid solution between the two oxides exists and alumina is formed.

Figure VI.2.3: (300) interplanar spacing of the produced coatings versus the Al to Cr ratio of the target

VI. Conclusions and Future Directions

VI.1 Summary and Conclusions

In this research, it has been shown that crystalline alumina films can be grown at substrate temperatures $< 500^{\circ}\text{C}$ when the sputtered Al flux is ionized. The temperature required for the phase formation of a crystalline alumina polymorph was found to be a function of both the ion flux and ion energy. κ -alumina containing films were synthesized at substrate temperatures of 430°C to 472°C . The hardness of these films was found to be equivalent to κ -alumina coatings deposited by CVD. This work opens the door for low temperature ($T_s < 500^{\circ}\text{C}$) κ -alumina coatings on steels.

For the industrial application of any coating system, maximizing the deposition rate is of great importance. A novel very high rate deposition process was researched, and its successful application was demonstrated for alumina and zirconia coatings.

Furthermore, alumina-chromia alloy films were grown in an effort to stabilize the hexagonal structure of alumina with chromia. Initial results suggest that a solid solution between the isostructural chromia and alumina is formed.

VI.1.1 High Rate Deposition of Alumina

From the research presented in Chapter 3 of this thesis, the following conclusions can be drawn: Partial pressure control and pulsed D.C. power are the enabling technological tools for the very high rate reactive deposition of alumina in this case at 76% of the metal deposition rate. This high rate can only be achieved if the O₂ partial pressure is controlled precisely. It is shown that variations of the partial pressure of several percent can increase or decrease the deposition rate significantly. The optical properties of the films are very sensitive to the incorporation of free metal in the film, and hence to the O₂ partial pressure. The high rate coatings are fully dense and X-ray amorphous.

The elastic moduli are typically 140 GPa, which is ~ 40% higher than usually reported for amorphous alumina. The maximum hardness value measured is ~11 GPa, which is consistent with the higher values previously reported. The coatings produced at 76% and 38% of the metal deposition rate had a refractive index of 1.65. A comparison to the state of the art in high rate deposition of alumina coatings by PVD is given in Figure VII.1. The relative deposition rates for R.F. and D.C. sputtering with baffles are taken from Jones et al⁵³, the pulsed D.C. data from Schiller et al¹¹⁶. Optimum high rate results can be achieved by utilizing both pulsed dc power and partial pressure control of the reactive gas. The relative deposition rate could be increased by 27% compared to the values published by Schiller et al¹¹⁶, for a straight dc process.

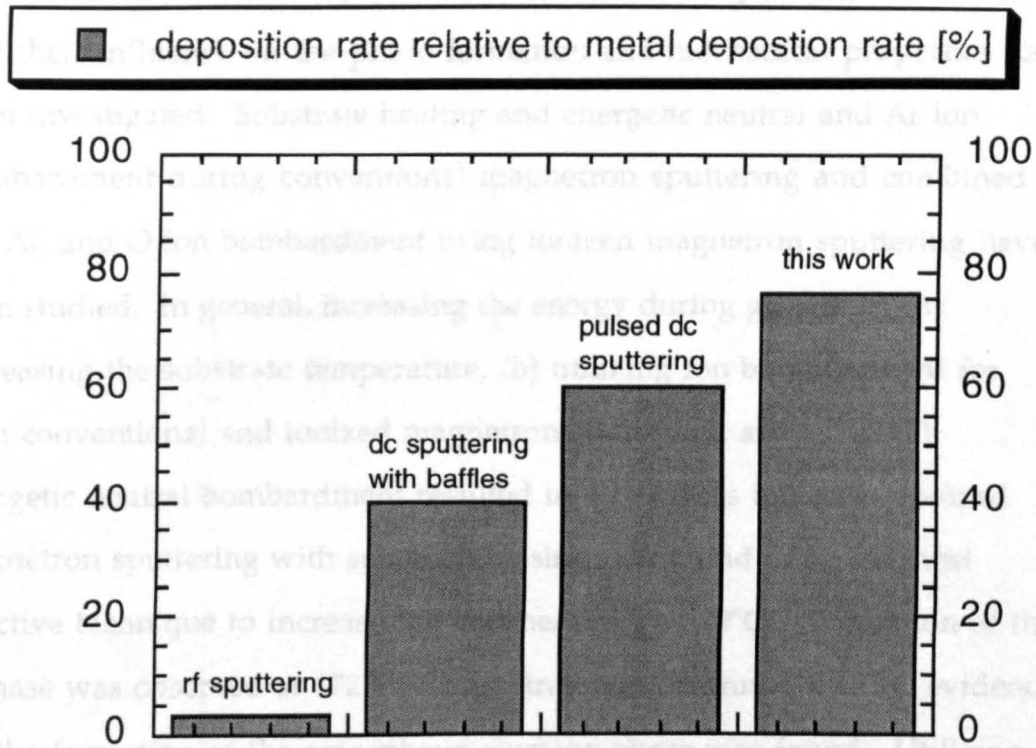


Figure VII.1: State of the art in high rate deposition of alumina coatings

VI.1.2 Phase Formation Studies - Ionized Magnetron Sputtering

Different ways of increasing the energy at the surface during growth of alumina films have been studied for substrate temperature $T_s < 500^\circ\text{C}$, and their influence on the phase formation and mechanical properties have been investigated. Substrate heating and energetic neutral and Ar ion bombardment during conventional magnetron sputtering and combined Ar, Al, and O ion bombardment using ionized magnetron sputtering have been studied. In general, increasing the energy during growth by (a) increasing the substrate temperature, (b) utilizing ion bombardment for both conventional and ionized magnetron sputtering, as well as (c) energetic neutral bombardment resulted in a hardness increase. Ionized magnetron sputtering with substrate biasing was found to be the most effective technique to increase the hardness at $T_s < 500^\circ\text{C}$. Formation of the κ -phase was observed at 472°C . At substrate temperatures $< 472^\circ\text{C}$ evidence for the formation of the amorphous alumina phase was found. Utilizing higher ion fluxes, the formation of κ and θ -phases occurred at 370°C to 430°C . The phases, as identified by XRD are mapped as a function of the substrate temperature and substrate ion current density in Figure VII.2.

It can be concluded from this work that higher ion currents lead to the presence of crystalline phases at lower substrate temperatures. However, high ion fluxes were found to increase the brittleness of the films significantly. Microindentation measurements of films produced at ion current densities $> 7 \text{ mA cm}^{-2}$ were not possible due to cracking of the films while indenting.

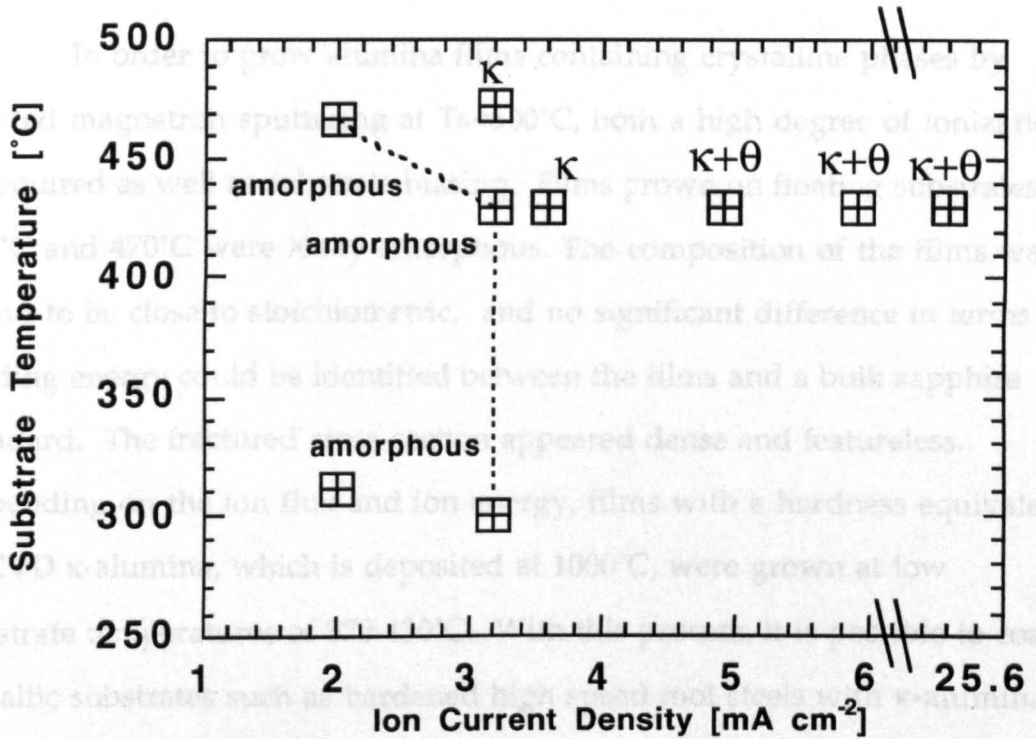


Figure VII.2: Phases identified by XRD as a function of substrate temperature and ion current density

It can be concluded from this work that higher ion currents lead to formation of crystalline phases at lower substrate temperatures. However, high ion fluxes were found to increase the brittleness of the films considerably. Nanoindentation measurements of films produced at ion current densities $> 7 \text{ mAcm}^{-2}$ were not possible due to cracking of the films while indenting.

In order to grow alumina films containing crystalline phases by ionized magnetron sputtering at $T_s < 500^\circ\text{C}$, both a high degree of ionization is required as well as substrate biasing. Films grown on floating substrates at 400°C and 470°C were X-ray amorphous. The composition of the films was found to be close to stoichiometric, and no significant difference in terms of binding energy could be identified between the films and a bulk sapphire standard. The fractured cross-section appeared dense and featureless. Depending on the ion flux and ion energy, films with a hardness equivalent to CVD κ -alumina, which is deposited at 1000°C , were grown at low substrate temperatures of $370\text{--}430^\circ\text{C}$. With this process, it is possible to coat metallic substrates such as hardened high speed tool steels with κ -alumina containing coatings without compromising the metallurgical and mechanical properties of the tool steel.

VI.3 Future Directions - Ways to Crystalline Low Temperature Alumina

Three different ways to encourage the growth of crystalline alumina at low substrate temperatures are suggested:

- 1) Ionized Aluminum Route
- 2) Alloying, or Multilayer Route
- 3) High Energetic Neutral Route

The first 2 ways are a direct result of my research over the last 2 years, the 3rd way was postulated by Zywitzki et al from the Fraunhofer Society in Dresden.

VI.3.1 Ionized Aluminum Route

It has been shown that low formation temperatures of crystalline alumina can be achieved by ionizing the sputtered aluminum flux in an effective manner, combined with utilizing a pulsed DC substrate bias potential. For a more basic understanding of the nucleation and growth phenomena, an experiment utilizing a mono-energetic aluminum ion beam is suggested: Ideally, flux and energy should be controlled separately. Possible techniques which are available are Al arc sources, Al microwave discharges, or a aluminum ion sources.

The oxygen is easiest supplied by a ion-gas source, for example a End Hall ion source, or a R.F. excited ion source. The energy range to be studied should extend to several hundreds of eV.

VI.3.2 Alloying, or Multilayer Route

The initial results gained by co-sputtering of chromium and aluminum in an argon/oxygen ambient, suggest the formation of a solid solution between the isostructural chromia and alumina (in the hexagonal α -alumina structure). The films were grown at substrate temperatures as low as 250°C.

It appears that chromia stabilizes the hexagonal structure of α -alumina. Experiments using hexagonal chromia layers as a template, for alumina in a multilayer or superlattice type of arrangement are promising.

VI.3.3 High Energetic Neutral Route

Over the last 3 years, no significant progress was made in lowering the formation temperature of α -alumina. The results published so far suggest a strong correlation between the target potential and the formation temperature of α -alumina. The larger the target potential, and hence the energetic oxygen neutral flux, the lower the formation temperature of α -alumina. The power used for the lowest formation temperature (760°C) was 17 kW. Increasing the target power might lead to α -alumina formation at lower substrate temperatures. Nucleation and growth of the high energetic neutral route would be best understood by utilizing molecular beam epitaxy (MBE), or pulsed laser deposition. The latter technique has the advantage that neutral energies on the order of 100's of eV are readily available.

References:

- ¹ E. Ryshkewitch and D. W. Richerson, *Oxide Ceramics* (General Ceramics, INC., Published by Arrangement with Academic Press, INC., Orlando, Florida, Haskell, New Jersey, 1985).
- ² M. V. Swain, *Structure and Properties of Ceramics*, Materials Science and Technology (VCH Publishers INC., Weinheim, Germany, 1994), vol. 11.
- ³ B. Bhushan and B. K. Gupta, *Handbook of Tribology* (McGraw-Hill, Inc., New-York, 1991).
- ⁴ H. G. Prengel, W. Heinrich, G. Roder, and K. H. Wendt, *Surface and Coatings Technology* 68/69, 217 (1994).
- ⁵ P. Liu and J. Skogsmo, *Acta Cryst.* B47, 425 (1991).
- ⁶ J. A. Thornton and J. Chin, *Ceramic Bulletin* 56, 5, 504 (1977).
- ⁷ M. Kamoshida, I. V. Mitchell, and J. W. Mayer, *Appl.Phys.Lett.* 18, 7, 292 (1971).
- ⁸ K. Iida and T. Tsujide, *Jpn.J.Appl.Phys.* 11, 6, 840 (1972).
- ⁹ S. Vurionen and L. Karlsson, *Surface Modifiacion Technologies IV*, Edited by T.S. Sudrashan, D.G. Bhat, M. Jeandin, *The Minerals, Metals & Materials Society*, (1991).

- ¹⁰ B. C. Lippens and J. J. Steggerda, in B. G. Linsen Eds., *Physical and Chemical Aspects on Absorbents and Catalysis*, vol. chap.4 (Academic Press, London, UK, 1970). and K. Wefers and Chanakya Misra, Alcoa Technical Paper No.19, revised, Alcoa Laboratories, 1987
- ¹¹ J. Lindstroem, B. Jonsson, and F. Ohlsson, US Patent 3,837,896, (1974).
- ¹² B. Lux, R. Funk, H. Schachner, and C. Triquet, (1974).
- ¹³ C. Chatfield, J. L. Lindstroem, and M. E. Sjostrand, *J.Phys.Colloq.* C5, 50, 377 (1989).
- ¹⁴ S. Vurionen and J. Skogsmo, *Thin Solid Films* 193/194, 536 (1990).
- ¹⁵ M. Halvarsson and S. Vurionen, *Surface and Coatings Technology* 76-77, 287 (1995).
- ¹⁶ M. Halvarson, H. Norden, and S. Vurionen, *Surface and Coatings Technology* 68/69, 266 (1994).
- ¹⁷ E. Frederiksson and J.-O. Carlsson, *J.Phys.Colloq.* C5, 391 (1989).
- ¹⁸ J. L. Vossen and W. Kern, *Thin Film Processes II* (Academic Press, New York, 1991).
- ¹⁹ S. M. Rosnagel, J. J. Cuomo, and W. D. Westwood, *Handbook of Plasma Processing Technology* (Noyes Publications, New Jersey, 1990).

- ²⁰ D. S. Rickerby and A. Matthews, *Advanced Surface Coatings - A Handbook of Surface Engineering* (Blackie & Sons Ltd, London, 1991).
- ²¹ J. J. Cuomo and S. M. Rossnagel, *Handbook of Ion Beam Processing Technology* (Noyes Publications, New York, 1989).
- ²² J. A. Thornton, *Journal of Vacuum Science and Technology* **11**, 666 (1974).
- ²³ R. Messier, A. P. Giri, and R. A. Roy, *Journal of Vacuum Science and Technology A* **2**, 2, 500 (1984).
- ²⁴ B. A. Movchan and A.V.Demchishin, *Fiz. Metal. Metalloved.* **28**, 4, 653 (1969).
- ²⁵ K.-H. Mueller, *Phys.Rev.B* **35**, 7906 (1987).
- ²⁶ F. L. Williams, R. D. Jacobson, J. R. McNeil, G. J. Exarhos, and J. J. McNally, *Journal of Vacuum Science and Technology* **6**, 3, 2020 (1988).
- ²⁷ J. C. Maxwell-Garnett, *Phil. Trans. R. Soc. London* **203**, 385 (1904).
- ²⁸ W. D. Westwood, *Journal of Vacuum Science and Technology* **15**, 1 (1978).
- ²⁹ K. H. Shih and D. B. Dove, *Journal of Vacuum Science and Technology A* **12**, 2, 321 (1993).
- ³⁰ F. M. Penning, *Physica (Utrecht)* **3**, 873 (1939).

- ³¹ F. M. Penning, . US Patent No: 2,146,025, USA, 1939),
- ³² R. F. Buhshah, *Deposition Technologies for Films and Coatings* (Noyes Publications, Park Ridge, NJ, 1982).
- ³³ B. Window and N. Savvides, *Journal of Vacuum Science and Technology* A 4, 2, 196 (1986).
- ³⁴ B. Window and N. Savvides, *Journal of Vacuum Science and Technology* A 4, 2, 453 (1986).
- ³⁵ S. Kadlec, J. Musil, and W. D. Muenz, *Journal of Vacuum Science and Technology* 8, 3, 1318 (1990).
- ³⁶ S. Kadlec, J. Musil, V. Valvoda, W. D. Muenz, H. Petersein, and J. Schroeder, *Vacuum* 42, 7-9, 2233 (1990).
- ³⁷ J. Musil, S. Kadlec, and W. D. Muenz, *Journal of Vacuum Science and Technology* 4, 3, 1171 (1991).
- ³⁸ W. D. Sproul, P. J. Rudnik, M. E. Graham, and S. L. Rohde, *Surface and Coatings Technology* 43/44, 270-278 (1990).
- ³⁹ S. L. Rohde, I. Petrov, W. D. Spoul, S. A. Barnett, P. J. Rudnik, and M. E. Graham, *Thin Solid Films* 193-194, 117 (1990).

- ⁴⁰ L. I. Maissel, in L. I. Maissel and R. Glang Eds., *Handbook of Thin Film Technology* (McGraw-Hill, New York, 1970).
- ⁴¹ J. L. Vossen and J. J. Cuomo, in J. L. Vossen and W. Kern Eds., *Thin Films Processes* (Academic Press, New York, 1978).
- ⁴² J. A. Thornton and A. S. Penfold, in J. L. Vossen and W. Kern Eds., *Thin Film Processes* (Academic Press, New York, 1978).
- ⁴³ J. A. Thornton, in R. F. B. e. al Eds., *Deposition Technologies for Films and Coatings; Development and Applications* (Noyes Publications, New Jersey, 1982).
- ⁴⁴ W. D. Sproul, *Journal of Vacuum Science and Technology* **4**, (6), 2874 (1986).
- ⁴⁵ N. Schwarz, *Trans. 10th Natl. Symp. vac. Technol. Pergamon, New York*, (1963).
- ⁴⁶ A. J. Stirling and W. D. Westwood, *Journal of Applied Physics* **41**, 742 (1970).
- ⁴⁷ J. Heller, *Thin Solid Films* **17**, 163 (1973).
- ⁴⁸ B. Gornachev, V. Orlinov, and V. Popova, *Thin Solid Films* **33**, 173 (1976).
- ⁴⁹ B. Gornachev, V. Orlinov, V. Tsaneva, and I. Petrov, *Thin Solid Films* **52**, 365 (1978).

⁵⁰ S. Schiller, U. Heisig, K. Goedicke, K. Schade, G. Teschner, and J. Henneberger, *Thin Solid Films* **64**, 455 (1979).

⁵¹ W. D. Sproul, *Thin Solid Films* **107**, 141 (1983).

⁵² W. D. Sproul and J. A. Thomashek, . US Patent No: 4,428,411, January 31, USA, 1984),

⁵³ F. Jones and J. Logan, *Journal of Vacuum Science and Technology A* **7**, 3, 1240 (1989).

⁵⁴ e. a. Corima, . US Patent No: U.S. Patent No. 4,046,659 , September 6. 1977, USA, 1977),

⁵⁵ V. Kirchhoff, . DD-Patent No: 252205 A1, September, 1, 1986, GDR, 1986),

⁵⁶ W. D. Muenz, H. Peterson, and M. Scherer, . DE-Patent No: 38 02 852 C2, Februar, 1, 1988, FRG, 1988),

⁵⁷ G. Este and W. D. Westwood, *Journal of Vacuum Science and Technology A* **6**, 3, 1845 (1988).

⁵⁸ M. Scherer, J. Schmitt, R. Latz, and M. Schanz, *Journal of Vacuum Science and Technology A* **10**, (4), 1772 (1991).

⁵⁹ M. I. Ridge and R. P. Howson, *Thin Solid Films* **96**, 121 (1982).

- ⁶⁰ W. D. Sproul, P. J. Rudnik, and M. E. Graham, *Surface and Coatings Technology* **39/40**, 355 (1989).
- ⁶¹ R. M. Valetta, J. A. Perri, and J. Risman, *Electrochem. Technol.* **4**, 402 (1966).
- ⁶² E. Hollands and D. S. Campbell, *J. Mat. Sci.* **3**, 544 (1968).
- ⁶³ A. J. Stirling and W. D. Westwood, *Thin Solid Films* **7**, 1 (1971).
- ⁶⁴ J. A. Thornton, US Dept. of Energy Report DSE-4042-T-19 , (1979).
- ⁶⁵ J. Chapin and C. R. Condon, . US Patent No: 4,116,784,1-10, USA, 1979),
- ⁶⁶ S. Schiller, G. Beister, E. Buedke, H.-J. Becker, and H. Schicht, *Thin Solid Films* **96**, 113 (1982).
- ⁶⁷ K. Enjouji, K. Murata, and S. Nishikawa, *Thin Solid Films* **108**, 1 (1983).
- ⁶⁸ A. S. Penfold, *Proceedings of the American Society of Vacuum Coaters Annual Technical Conference, New Orleans* , 381 (1986).
- ⁶⁹ S. Kadlec, J. Musil, and J. Vyskocil, *Vacuum* **37**, 18, 729 (1987).
- ⁷⁰ S. Schiller, U. Heisig, K. Steinfelder, and J. Struempfel, *Proceedings of the International Conference on Ion Plating and Allied Techniques, London, (CEP Consultants, Edinburgh, 1979)* , (1979).

- ⁷¹ S. Maniv, C. Miner, and W. D. Westwood, *Journal of Vacuum Science and Technology* 18, (2), 195 (1981).
- ⁷² G. Este and W. D. Westwood, *Journal of Vacuum Science and Technology* 2, (3), 1238 (1984).
- ⁷³ M. Scherer and P. Wirtz, *Thin Solid Films* 119, 203 (1984).
- ⁷⁴ T. M. Pang, M. Scherer, B. Heinz, C. Williams, and G. N. Chaput, *Journal of Vacuum Science and Technology A* 7, 3, 1254 (1989).
- ⁷⁵ A. J. Aronson, D. Chen, and W. H. Class, *Thin Solid Films* 72, 535 (1980).
- ⁷⁶ W. D. Sproul, . US Patent No: 4,428,812, USA, 1984),
- ⁷⁷ A. Billard and C. Frantz, presented at ICMCTF, San Diego, USA, 1996 , (1996).
- ⁷⁸ S. Schiller, U. Heisig, K. Steinfelder, J. Strumpfel, A. Friedrich, and R. Fricke, *Proceedings: Conference of Ion Plating and Allied Techniques (CEP Consultants Edinburgh, 1987), , (1987).*
- ⁷⁹ R. P. Howson, A. G. Spencer, K. Oka, and R. W. Lewin, *Journal of Vacuum Science and Technology A* 7, (3), 1230 (1989).
- ⁸⁰ J. Affinito and R. R. Parson, *Journal of Vacuum Science and Technology A* 2, (3), 1275 (1983).

- ⁸¹ W. D. Sproul, *Surface and Coatings Technology* **33**, 73 (1987).
- ⁸² W. D. Sproul, P. J. Rudnik, and C. A. Gogel, *Thin Solid Films* **171**, 171 (1989).
- ⁸³ P. Beucherie, M. Block, and J. G. Wurm, *Journal of the Electrochemical Society* **116**, 1, 159 (1969).
- ⁸⁴ Y. Murayama, *Jap. J. Appl. Phys. Suppl. 2, Pt.1* , 459 (1974).
- ⁸⁵ Y. Murayama, *Journal of Vacuum Science and technology* **12**, 4, 813 (1975).
- ⁸⁶ S. M. Rossnagel and J. Hopwood, *Appl. Phys. Lett.* **63**, 3285 (1993).
- ⁸⁷ S. M. Rossnagel and J. Hopwood, *Journal of Vacuum Science and Technology B* **12**, 449. (1994).
- ⁸⁸ A. A. Voevodin, C. Rebholz, J. M. Schneider, and A. Matthews, *Surface and Coatings Technology* **73**, 185 (1995).
- ⁸⁹ J. Musil and M. Misina, 4 th Internat. Symp. on trends and new applications in this films March 7-14, Dresden (1994).
- ⁹⁰ W. M. Holber, J. S. Logan, H. J. Grabarz, J. T. C. Yeh, J. B. O. Caughman, A. Sugerman, and F. E. Turene, *Journal of Vacuum Science and Technology A* **11**, 6, 2903 (1993).

- ⁹¹ C. A. Nichols, S. M. Rossnagel, and S. Hamaguchi, *Journal of Vacuum Science and Technology B* **14**, 5, 3270 (1996).
- ⁹² R. G. Frieser, *J. Electrochem. Soc.* **113**, 4, 357 (1966).
- ⁹³ C. A. T. Salama, *J. Electrochem. Soc.* **117**, 7, 913 (1970).
- ⁹⁴ I. H. Pratt, *Solid State Technol.* **12**, 12, 49 (1969).
- ⁹⁵ A. L. Dragoo and J. J. Diamond, *J. Am. Ceram. Soc.* **50**, 11, 568 (1967).
- ⁹⁶ K. M. Eisele, *J. Electrochem. Soc.* **122**, 1, 148 (1975).
- ⁹⁷ R. F. Bunshah and R. J. Schramm, *Thin Solid Films* **40**, 211 (1977).
- ⁹⁸ O. Zywitzki and G. Hoetsch, *Surface and Coatings Technology* **76/77**, 754 (1995).
- ⁹⁹ O. Zywitzki, G. Hoetsch, F. Fietzke, and K. Goedicke, *Surface and Coatings Technology* **82**, 169 (1996).
- ¹⁰⁰ U. Helmersson, I. Ivanov, and K. Macak, presented at the Fifth International Conference on Plasma Surface Engineering, Garmisch-Partenkirchen September 9-13 , (1996).
- ¹⁰¹ A. Jaemting, M. Ring, S. Ruppi, and M. V. Swain, *Journal of Hard Materials* **6**, 67 (1995).

- ¹⁰² R. Cueff, B. Baud, J. P. Besse, and M. Jaquette, *Thin Solid Films* **266**, 198 (1995).
- ¹⁰³ R. Cueff, G. Baud, M. Benmalek, J. P. Besse, J. R. Butruille, and M. Jacquet, *Surface and Coatings Technology* **80**, 96 (1996).
- ¹⁰⁴ J. M. Schneider, W. D. Sproul, R. W. Chia, M.-S. Wong, and A. Matthews, accepted for publication in *Surface and Coatings Technology* , (1996).
- ¹⁰⁵ B. M. Kramer and P. K. Judd, *Journal of Vacuum Science and Technology A* **3**, 6, 2439 (1985).
- ¹⁰⁶ J. T. DeMasi-Marcin and D.K.Gupta, *Surface and Coatings Technology* **68/69**, 1 (1994).
- ¹⁰⁷ J. M. Schneider, W. D. Sproul, A. R. T. Lefkow, A. Matthews, M. E. Graham, and J. Rechner, *39th Annual Technical Conference Proceedings*, May 5-10, Philadelphia, USA , 168 (1996).
- ¹⁰⁸ X. Chu, M. S. Wong, W. D. Sproul, S. L. Rohde, and S. A. Barnett, *Journal of Vacuum Science and Technology A* **10**, 4, 1604 (1992).
- ¹⁰⁹ D. Li, Y.W.Chung, S.Lopez, M.S.Wong, and W.D.Sproul, *Journal of Vacuum Science and Technology A* **13**, 3, 1063 (1994).
- ¹¹⁰ J. Sellers, *Asymetric Bipolar Pulsed DC*, ENI Tech Note , (1996).

- 111 UMIS 200 Operating Manual, CSIRO , (1992).
- 112 W. C. Oliver and G. M. Pharr, *Journal of Materials Research* **7**, 6, 1564 (1992).
- 113 M. F. Doerner and W. D. Nix, *Journal of materials research* **1**, 4, 601 (1986).
- 114 G. Electric, *Fused Quartz Product Handbook* 1985).
- 115 G. Simmons and H. Wang, *Single Crystal Elastic Constants and Calculated Aggregate Properties: A Handbook* (MIT Press, Cambridge MA, 1971).
- 116 S. Schiller, K. Goedicke, J. Reschke, V. Kirchhoff, S. Schneider, and F. Milde, *Surface and Coatings Technology* **61**, 331 (1993).
- 117 P. J. Clarke, *Journal of Vacuum Science and Technology A* **12**, 594 (1994).
- 118 O. Knotek, F. Loeffler, and W. Beele, *Surface and Coatings Technology* **61**, 6 (1993).
- 119 S. Zhu, F. Wang, H. Lou, and W. Wu, *Surface and Coatings Technology* **71**, 9 (1995).
- 120 S. K. Rutledge, B. A. Banks, and J. Hunt, *NASA Technical Memorandum* 106966 , (1995).

- ¹²¹ O. S. Heavens, *Optical Properties of Thin Solid Films* (Dover Publications Inc., New York, 1965).
- ¹²² G. K. Wehner and G. S. Anderson, in L. I. Maisel and R. Glang Eds., *Handbook of Thin Film Technology* (Mc Graw-Hill Book Company, New York, 1970).
- ¹²³ K. Tominaga, N. Ueshiba, Y. Shintani, and O. Tada, *Japanese Journal of Applied Physics* **20**, 3, 510 (1981).
- ¹²⁴ K. Tominaga, S. Iwamura, Y. Shintani, and O. Tada, *Japanese Journal of Applied Physics* **21**, 5, 688 (1982).
- ¹²⁵ H. Kuchling, *Taschenbuch der Physik* (Verlag Harri Deutsch, Frankfurt, 1988).
- ¹²⁶ R. S. Robinson, *Journal of Vacuum Science and Technology* **16**, 2, 185 (1979).
- ¹²⁷ A. M. Myers, J. R. Doyle, and J. R. Abelson, *Journal of Vacuum Science and Technology* **9**, 3, 614 (1991).
- ¹²⁸ F. W. Dynys and J. W. Halloran, *Ultrastructure Processing of Ceramic, Glasses and Composites*, Edited by L.L. Hench and D.R. Ulrich (John Wiley & Sons Inc., NY, 1984).
- ¹²⁹ O. Zywitzki and G. Hoetsch, *Surface and Coatings Technology* **86-87**, 640 (1997).

- ¹³⁰ A. Handbook, Vol.1, Properties and Selection: Iron, Steels, and High Performance Alloys, , 134 (1990).
- ¹³¹ A. A. Voevodin, M. A. Campano, A. J. Safriet, M. S. Donley, and J. S. Zabinski, Appl. Phys. Lett. **69**, 2, 188 (1996).
- ¹³² A. Y. Liu and M. L. Cohen, Physical Review B **41**, 15, 10727 (1990).
- ¹³³ J. E. Greene, CRC critical review of solid state and material science **11**, 47 (1984).
- ¹³⁴ L. Hultman, U. Helmerson, S. A. Barnett, J.-E. Sundgren, and J. E. Greene, Journal of Applied Physics **61**, 2, (1987).
- ¹³⁵ I. Petrov, A. Myers, J. E. Greene, and J. R. Abelson, Journal of Vacuum Science and Technology A **12**, 5, 2846 (1994).
- ¹³⁶ JCPDS, International center for powder diffraction data, Swarthmore, PA, USA, Card 23-1009 , (1994).
- ¹³⁷ S. M. Rossnagel, presented at ICMCTF 1996, San Diego, USA , (1996).
- ¹³⁸ E. W. Bunting, Journal Research Natl. Bur. Standards (U.S.) **6**, 947 (1931).

APPENDIX: NANOINDENTATION

M := READPRN(qwer)

y := 0.. 2

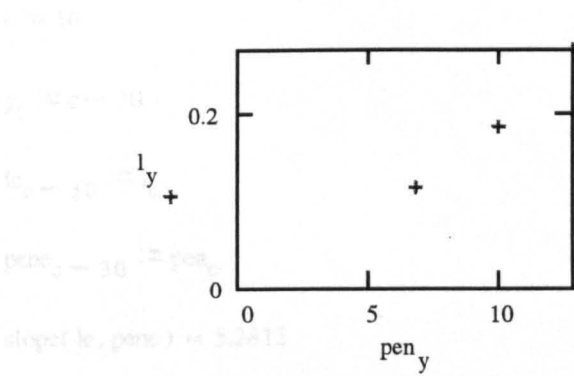
pen_y := M_{y, 0}

l_y := M_{y, 1}

Ediamond := 1141

vdiamond := 0.07

vsample := 0.234



ip := intercept(l, pen)

ip = 2.5539

M := READPRN(qwer)

x := 0.. 59

pen_x := M_{x, 0}

l_x := M_{x, 1}

138.7014
135.6714
132.5614
129.4914

c := 30..33

pen₃₀ = 138.7014

load := l₃₀

load = 10.0155



t := 10

y_t := c - 30

le_{c-30} := l_c

pene_{c-30} := pen_c

slope(le, pene) = 5.2812

slope(pene, le) = 0.1893

corr(le, pene) = 0.9999

int := intercept(le, pene)

l _c
10.0155
9.4244
8.8513
8.2964

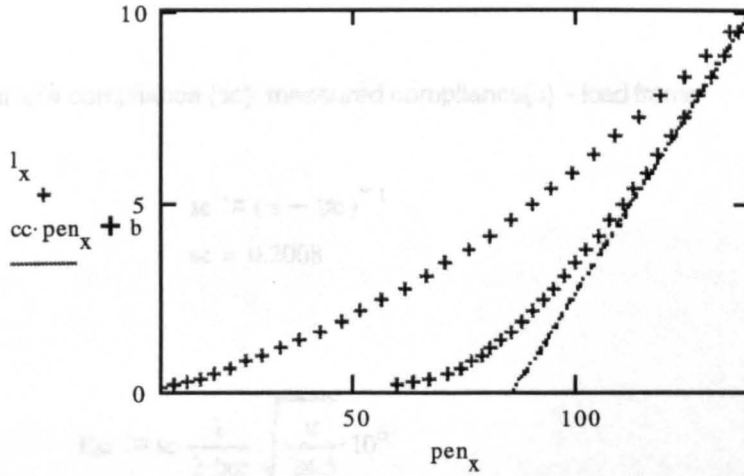
pen _c
138.7014
135.6704
132.5618
129.6492

int = 85.8392

b := intercept(pene, le)

s := slope(le, pene)

cc := slope(pene, le)



load = 10.0155

ip = 2.5539

hc = 104.1067

hc := (int - ip) · 1.25

subtract initial penetration

hcc := 1.9057 · hc^{0.91564}

tip correction

hcc = 134.0722

E1 = 330.7504 GPa

H = 22.742 GPa

hcc = 134.0722

hc = 104.1067

load = 10.0155

$$\frac{\text{load}}{24.5 \cdot \text{hcc}^2} \cdot 10^6 = 22.742 \quad \text{GPa}$$

plug in the machine compliance and recalculation of the hardness:

$$\text{load frame compliance} \quad \text{lfc} := .3$$

calculation of the sample compliance {sc}: measured compliance{c} - load frame compliance {lfc}

$$\text{sc} := (\text{c} - \text{lfc})^{-1}$$

$$\text{sc} = 0.2008$$

$$\text{Esr} := \text{sc} \cdot \frac{1}{2 \cdot \text{hcc}} \cdot \sqrt{\frac{\pi}{24.5}} \cdot 10^6$$

$$\text{Esr} = 268.096 \quad \text{GPa}$$

$$\text{Es} := \left(\frac{1}{\text{Esr}} - \frac{1 - \text{vdiamond}^2}{\text{Ediamond}} \right)^{-1} \cdot (1 - \text{vsample}^2)$$

$$\text{Es} = 330.7504 \quad \text{GPa}$$

$$\text{h} = 22.742 \quad \text{GPa}$$

$$\text{pen}_{30} = 138.7014$$

$$\text{hcc} = 134.0722$$

$$\text{hc} = 104.1067$$

$$\text{load} = 10.0155$$

VITA

Birthdate: September 25, 1969
Birthplace: St.Georgen, Germany

Education:

Fachhochschule Furtwangen, Germany, June 1992
Dipl.Ing. (FH) degree in Materials and Surface Engineering

University of Hull, January 1995
M.Sc. degree in Engineering, Design and Manufacturing

University of Hull, expected September 1997
Ph.D. degree in Engineering, Design and Manufacturing

Publications:

- ¹ J. M. Schneider, W. D. Sproul, A. A. Voevodin, and A. Matthews, "Crystalline alumina deposited at low temperature by reactive ionized magnetron sputtering", *Journal of Vacuum Science and Technology A*, **15**, 1084 (1997).
- ² J. M. Schneider, W. D. Sproul, and A. Matthews, "Phase formation and mechanical properties of alumina coatings prepared at substrate temperatures <math>< 500^{\circ}\text{C}</math> by ionized and conventional magnetron sputtering", accepted for publication in *Surface and Coatings Technology*, (1997).
- ³ J. M. Schneider, W. D. Sproul, and A. Matthews, "Reactive ionized magnetron sputtering of alumina hard coatings", *Surface and Coatings Technology*, **92**, (1996).
- ⁴ J. M. Schneider, W. D. Sproul, R. W. Chia, M.-S. Wong, and A. Matthews, "Very high rate reactive sputtering of alumina hard coatings", accepted for publication in *Surface and Coatings Technology*, (1997).
- ⁵ J. M. Schneider, W. D. Sproul, and J. Sellers, "Alumina-chromia coatings deposited by reactive magnetron sputtering", *Society of Vacuum Coaters, 40th Annual Technical Conference Proceedings*, New Orleans, USA (1997)
- ⁶ J. M. Schneider, W. D. Sproul, A. R. T. Lefkow, A. Matthews, M. E. Graham, and J. Rechner, "Scalable processes for pulsed dc magnetron sputtering of non-conducting oxides", *Society of Vacuum Coaters, 39th Annual Technical Conference Proceedings*, May 5-10, Philadelphia, USA (1996)

- ⁷ J. M. Schneider, C. Rebholz, A. A. Voevodin, A. Leyland, and A. Matthews, "Deposition and characterization of stainless steel coatings prepared by magnetron sputtering", *Vacuum*, **47**, 1077 (1996).
- ⁸ J. M. Schneider, A. A. Voevodin, C. Rebholz, A. Matthews, J. H. C. Hogg, D. B. Lewis, and M. Ives, "X-ray diffraction investigations of magnetron sputtered TiCN coatings", *Surface and Coatings Technology*, **74/75**, 312 (1995).
- ⁹ J. M. Schneider, A. A. Voevodin, C. Rebholz, and A. Matthews, "Micro structural effects and morphological effects on the tribological properties of electron enhanced magnetron sputtered hard coatings", *Journal of Vacuum Science and Technology A*, **13**, 2189 (1995).
- ¹⁰ A. A. Voevodin, J. M. Schneider, C. Rebholz, and A. Matthews, "Multilayer composite ceramic-metal-DLC coatings for sliding wear applications", *Tribology International*, **29**, 559 (1996).
- ¹¹ A. A. Voevodin, J. M. Schneider, C. Caperaa, P. Stevenson, and A. Matthews, "Characterization of a saddle field source for deposition of diamond-like carbon films", *Ceramics International*, **22**, 1 (1996).
- ¹² M. S. Wong, W. J. Chia, P. Yashar, J. M. Schneider, W. D. Sproul, and S. A. Barnett, "High-rate reactive d.c. magnetron sputtering of ZrOx coatings", *Surface and Coatings Technology*, **86-87**, 381 (1996).
- ¹³ A. Matthews, A. Leyland, B. Dorn, P. R. Stevenson, M. Bin-Sudin, C. Rebholz, A. A. Voevodin, and J. M. Schneider, "Plasma based surface engineering processes for wear and corrosion protection", *Journal of Vacuum Science and Technology A*, **13**, (1995).
- ¹⁴ A. A. Voevodin, P. Stevenson, C. Rebholz, J. M. Schneider, and A. Matthews, "Active process control of reactive sputter deposition", *Vacuum*, **46**, 723 (1995).
- ¹⁵ A. A. Voevodin, C. Rebholz, J. M. Schneider, and A. Matthews, "Wear Resistant Composite Coatings Deposited by Electron Enhanced Closed Field Unbalanced Magnetron Sputtering", *Surface and Coatings Technology*, **73**, 185 (1995).
- ¹⁶ A. A. Voevodin, J. M. Schneider, C. Caperaa, P. Stevenson, and A. Matthews, "Studies of atom beams produced by a saddle field source used for depositing diamond like carbon films on glass", *Vacuum*, **46**, 299 (1995).